

Universidade de São Paulo  
Instituto de Física

Estrutura eletrônica do candidato a semimetal  
topológico  $\text{ZrTe}_2$

Pedro Henrique Arantes Moya

Orientador: Prof. Dr. Fernando Assis Garcia

Co-orientador: Prof. Dr. Wendell Simões e Silva

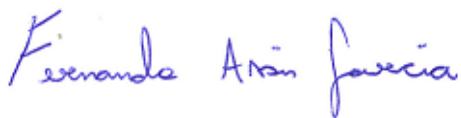
Dissertação submetida ao Instituto de Física da Universidade de São Paulo, como requisito parcial para a obtenção do título de Mestre em Ciências.

Banca Examinadora:

Prof. Dr. Fernando Assis Garcia (IFUSP)

Prof. Dr. Abner de Siervo (Unicamp)

Prof. Dr. Helena de Souza Bragança Rocha (UnB)



Sao Paulo  
2023

**FICHA CATALOGRÁFICA**  
**Preparada pelo Serviço de Biblioteca e Informação**  
**do Instituto de Física da Universidade de São Paulo**

Moya, Pedro Henrique Arantes

Bandas dobradas e elétrons de Dirac em um candidato a semimetal topológico/ Folded bands and Dirac electrons in a topological semimetal candidate. São Paulo, 2023.

Dissertação (Mestrado) - Universidade de São Paulo. Instituto de Física. Depto. Física Aplicada.

Orientador: Prof. Dr. Fernando Assis Garcia.

Área de Concentração: Física da Matéria Condensada.

Unitermos: 1. Estrutura eletrônica; 2. Espectroscopia de raio-X; 3. Metais de transição dicalcogenados; 4. Densidade de onda de carga.

USP/IF/SBI-095/2023

University of São Paulo  
Physics Institute

# Electronic structure of the topological semimetal candidate $\text{ZrTe}_2$

Pedro Henrique Arantes Moya

Supervisor: Prof. Dr. Fernando Assis Garcia

Co-supervisor: Prof. Dr. Wendell Simões e Silva

Dissertation submitted to the Physics Institute of the University of São Paulo in partial fulfillment of the requirements for the degree of Master of Science.

Examining Committee:

Prof. Dr. Fernando Assis Garcia (IFUSP)

Prof. Dr. Abner de Siervo (Unicamp)

Prof. Dr. Helena de Souza Bragança Rocha (UnB)

Sao Paulo  
2023

# Abstract

Transition Metal Dichalcogenides (TMDs) have garnered substantial attention over recent decades due to their remarkable properties. These layered materials offer unparalleled versatility in tailoring their electrical and optical characteristics through various techniques, making them a prime platform for exploring novel physical phenomena. Chemical doping, a well-established method, manipulates electron counts through the introduction of impurities, potentially leading to the emergence of distinct ground states, such as superconductivity or density wave phases.

In this study, we employed Angle Resolved Photoemission Spectroscopy (ARPES) to investigate the impact of transition metals Ni and Dy intercalation on the electronic structure of the  $1T$ -ZrTe<sub>2</sub> system. Our findings reveal that Ni doping induces the formation of a flat band arising from Ni-d states within the electronic structure at  $E_B \approx -1.2$  eV and potentially at  $E_B \approx -0.7$  eV. This new electronic configuration offers insights into the appearance of both the superconducting state at  $T = 4$  K and the suggested charge density wave state at  $T = 287$  K. In the case of Dy-doping, we observe a non-monotonic variation in the sizes of hole and electron pockets: 1% doping results in reduced pocket areas, while 5% doping reverts to the parent compound case. This behavior is reminiscent of the superconducting dome in the phase diagram, with 1% representing near-optimal doping and 5% residing beyond the superconducting region. Furthermore, we identify linear Dirac states near the Fermi level at the  $\Gamma(A)$ -point for all systems studied.

This work underscores the versatility of TMDs and the profound influence of chemical doping on their electronic properties, offering valuable insights into emergent physical phenomena and potential applications.

**Keywords:** ARPES; Transition Metal Dichalcogenides; Charge Density Wave; Flat Bands



## Resumo

Os Metais de Transição Dicalcogenados (TMDs) têm atraído considerável atenção nas últimas décadas devido às suas propriedades notáveis. Esses materiais em camadas oferecem uma versatilidade sem paralelos na adaptação de suas características elétricas e ópticas por meio de várias técnicas, tornando-os uma plataforma de destaque para explorar fenômenos físicos inovadores. A dopagem química, um método bem estabelecido, manipula a contagem de elétrons por meio da introdução de impurezas, potencialmente levando ao surgimento de estados fundamentais distintos, como a supercondutividade ou fases de ondas de densidade.

Neste estudo, empregamos a Espectroscopia de Fotoemissão Resolvida em Ângulo (ARPES) para investigar o impacto da intercalação de metais de transição Ni e Dy na estrutura eletrônica do sistema  $1T\text{-ZrTe}_2$ . Nossas descobertas revelam que a dopagem de Ni induz a formação de uma banda plana originada dos estados  $d$  do Ni dentro da estrutura eletrônica em  $E_B \approx -1,2$  eV e potencialmente em  $E_B \approx -0,7$  eV. Essa nova configuração eletrônica lança luz sobre o surgimento tanto do estado supercondutor a  $T = 4$  K quanto do sugerido estado de onda de densidade de carga a  $T = 287$  K. No caso da dopagem de Dy, observamos uma variação não monotônica nos tamanhos dos bolsos de buracos e elétrons: a dopagem de 1% resulta em áreas de bolsos reduzidas, enquanto a dopagem de 5% volta ao caso do composto original. Esse comportamento é remanescente do domo supercondutor no diagrama de fases do material, em que 1% representa a dopagem quase-ótima e 5% está além da região supercondutora. Além disso, identificamos estados lineares de Dirac próximos ao nível de Fermi no ponto  $\Gamma(A)$  para todos os sistemas estudados.

Este trabalho destaca a versatilidade dos TMDs e a influência profunda da dopagem química em suas propriedades eletrônicas, oferecendo resultados valiosos sobre fenômenos físicos emergentes e possíveis aplicações.

**Palavras-Chave:** ARPES; Metais de Transição Dicalcogenados; Onda de Densidade de Carga; Bandas Planas



# Agradecimentos

Gostaria de expressar o meu agradecimento a todos, pessoas e instituições, que foram importantes para o desenvolvimento deste projeto e que me ajudaram a atingir este objetivo. Pelo apoio financeiro ao meu mestrado, agradeço à agência financiadora Coordenação de Aperfeiçoamento de Pessoal de Nível Superior - Brasil (CAPES) - Código de Financiamento 88887.639735/2021-00 e 88887.816479/2022-00 - e ao Swedish Council of Higher Education, pelo financiamento do meu intercâmbio pelo programa *Linnaeus-Palme*. Sou muito grato ao meu orientador, professor Fernando Assis Garcia, por toda a disponibilidade, discussões, aconselhamento e paciência durante todo o período do mestrado e nos anos anteriores. Gostaria de agradecer também ao meu coorientador, Wendell Simões e Silva, pelo apoio nos experimentos e instrumentação.

Quero agradecer também aos meus colegas do grupo de pesquisa: Juliana, Wagner, Hanna, Álvaro, Lauro, Valkíria, Rodrigo e Marli. Eles proporcionaram ótimas discussões, colaborações, apoio e momentos de descontração nesse período. Em especial, à Marli, que me ajudou bastante durante todo o mestrado com o processamento de dados e entendimento dos experimentos e teoria, sendo na prática também uma co-orientadora para mim, deixo aqui meu muitíssimo obrigado. Aos professores e funcionários do IFUSP que me auxiliaram direta ou indiretamente, em particular ao técnico do laboratório de cristalografia Tarsis Germano, que me ajudou bastante ao longo dos anos em que estive lá, também deixo aqui expresso meus agradecimentos.

Gostaria de agradecer ao professor Claude Monney pela disponibilidade para realizarmos os experimentos preliminares do projeto em seu laboratório na Universidade de Fribourg e também ao laboratório MAX IV pelo tempo de linha na estação experimental Bloch, bem como o suporte e apoio do Jacek Osiecki e Craig Polley durante o experimento. Não posso deixar de agradecer também ao professor Antonio Jefferson e Lucas E. Correa pela colaboração e pelas amostras usadas nesse trabalho e também agradecer ao professor Abner pela oportunidade de treinar e aprender tecnologia de vácuo em seu laboratório e ao Alisson por me acompanhar e instruir. Também agradeço ao professor Venkata K. Mutta, quem me deu a oportunidade de trabalhar em seu grupo de pesquisa durante meu período de intercâmbio em que estive na Universidade de Uppsala. Aos estudantes Henry Nameirakpam e David Muradas pelo treinamento, ajuda e companhia durante as etapas do projeto que lá desenvolvi.

Por fim, mas igualmente importante, agradeço à minha família, especialmente meu pai Mauro e minha mãe Rosane, pelo apoio e compreensão durante essa etapa. Também agradeço muito aos meus amigos - Hen-



rique, Matheus, Gabriel, Gustavo, Otávio, Leonardo, Renato, Nicholas, Letícia, Daniel, Isabela, Marcelo, Vitor, Jonas, ZL, Tayna, João e Jonatas pelos tão necessários momentos de descontração, conversas construtivas, motivação e apoio, tornando os momentos difíceis menos ruins e os bons momentos melhores ainda.

# Contents

<b>1</b>	<b>Introduction</b>	<b>1</b>
1.1	Transition Metal Dichalcogenides (TMDs)	1
1.1.1	Electronic Structure	2
1.1.2	Crystal Structure, Brillouin Zone and Band Structure of $\text{ZrTe}_2$	4
1.2	The Charge Density Wave Phenomenon	10
1.2.1	Peierl's Picture	10
1.2.2	Fermi Surface Nesting	12
1.2.3	Excitonic Insulator	13
1.2.4	Experimental Signatures of the CDW phase in 1T-TaS <sub>2</sub> , 2H-TaSe <sub>2</sub> and 1T-TiSe <sub>2</sub> : an ARPES overview	15
1.2.5	The case of the monolayer 1T-ZrTe <sub>2</sub>	18
1.3	Flat Bands	19
<b>2</b>	<b>Instrumentation and Methodology</b>	<b>23</b>
2.1	Photoelectron Spectroscopy	23
2.2	Interacting Picture - The one-particle spectral function and self energy	26
2.3	ARPES - General Description	27
2.4	Light Polarization Effects	31
<b>3</b>	<b>ARPES Data and Analysis</b>	<b>33</b>
3.1	Experimental Data Processing	33
3.2	Preliminary Measurements - He-discharge lamp	34
3.3	Synchrotron Light Measurements	37
3.3.1	The Parent Compound	37
3.3.2	The Ni-doped Sample	42
3.3.3	The Dy-doped Sample	51
3.4	Fermi Surface Nesting Analysis	56
<b>4</b>	<b>Conclusion</b>	<b>63</b>

---

<b>Bibliography</b>	<b>65</b>
<b>A Complementary Figures</b>	<b>73</b>
<b>B Strain Device Project</b>	<b>79</b>
<b>C Investigation of van Hove Singularities in BLG by STM and STS Techniques</b>	<b>83</b>
C.1 Scanning Tunneling Microscopy (STM)	83
C.2 Scanning Tunneling Spectroscopy (STS)	84
C.3 van Hove singularities (vHs)	85
C.3.1 vHs on Twisted Bilayer Graphene (TBG) and the Moiré effect	86
C.4 STM/STS Experimental Setup and Measurements	87
C.4.1 Measurements Quality Factors and Preparation	89
C.4.2 The Substrate Effect - Graphene on SiO <sub>2</sub>	90
C.5 Results	92
C.5.1 Graphene Monolayer STM Data	92
C.5.2 Graphene Monolayer STS Data	93
C.5.3 Graphene Bilayer STM Data	94
C.5.4 Graphene Bilayer STS Data	94
C.6 Discussion	98
C.6.1 Scanning Tunneling Microscopy Data	98
C.6.2 Scanning Tunneling Spectroscopy Data	98

# List of Figures

1.1	Schematic view of the different phases of TMDs . . . . .	2
1.2	Schematic view of band structures . . . . .	3
1.3	(a): Crystal structure of 1T-ZrTe <sub>2</sub> . (b): 3D Brillouin Zone of the system. The high symmetry points are labelled. . . . .	5
1.4	Superconducting Phase Diagram of Dy-doping ZrTe <sub>2</sub> . . . . .	8
1.5	<i>ab-initio</i> calculation of the electronic structure of ZrTe <sub>2</sub> and DOS of different Ni-doped ZrTe <sub>2</sub> compounds . . . . .	9
1.6	The CDW phenomenon in 1D (The Peierls Transition), the electronic susceptibility for different dimensionalities and the phonon softening in 1D. . . . .	11
1.7	The Fermi Surface Nesting Phenomenon in different FS topologies . . . . .	13
1.8	Excitonic Insulator Transition in a semimetal . . . . .	14
1.9	Atomic displacements in the commensurate CDW/PDL phase of illustrative TMD materials .	16
1.10	ARPES measurements for illustrative TMD materials . . . . .	17
1.11	ARPES measurements and Schematic of the band structure for the Monolayer 1T-ZrTe <sub>2</sub> . . .	19
1.12	One dimensional diamond chain electronic structure calculated by the Tight Binding Model .	21
2.1	Energetics of the photoemission process along with the schematics of the ARPES geometry .	29
2.2	Schematic of the rotational degrees of freedom for an ARPES experiment . . . . .	30
2.3	Schematic of the linear light polarization in ARPES and the <i>p</i> orbitals representations . . . .	32
3.1	Preliminary ARPES measurements of ZrTe <sub>2</sub> for $\Gamma$ M high symmetry direction . . . . .	35
3.2	Preliminary ARPES measurements of Ni <sub>x</sub> ZrTe <sub>2</sub> ( <i>x</i> =0, 0.05) for $\Gamma$ M high symmetry direction	36
3.3	ARPES measurements of ZrTe <sub>2</sub> for $\Gamma$ K high symmetry direction . . . . .	38
3.4	MDC evaluation of the ZrTe <sub>2</sub> bands near $E_F$ . . . . .	39
3.5	ARPES measurements of ZrTe <sub>2</sub> Fermi Maps . . . . .	41
3.6	$k_z$ dispersion of ZrTe <sub>2</sub> for both polarization . . . . .	42
3.7	Comparison of the ARPES spectra between the parent and the Ni-doped compound . . . . .	43
3.8	Energy Distribution Curves as function of temperature for the Ni-doped compound at $\Gamma$ in both BZ planes. . . . .	44

3.9	ARPES measurements of $\text{Ni}_{0.05}\text{ZrTe}_2$ for $\Gamma\text{M}$ high symmetry direction for different photon energy . . . . .	46
3.10	ARPES measurements of $\text{Ni}_{0.05}\text{ZrTe}_2$ for $\Gamma\text{M}$ high symmetry direction for different photon energy . . . . .	47
3.11	MDC evaluation of the $\text{Ni}_{0.05}\text{ZrTe}_2$ bands near $E_F$ . . . . .	48
3.12	Schematic of the area calculation procedure . . . . .	49
3.13	Ni-doping dependence of the pocket's areas. . . . .	50
3.14	MDC evaluation of the Dy- doped $\text{ZrTe}_2$ bands near $E_F$ . . . . .	52
3.15	ARPES measurements of $\text{Dy}_{0.01}\text{ZrTe}_2$ for both high symmetry direction and polarization . . . . .	53
3.16	ARPES measurements of $\text{Dy}_{0.05}\text{ZrTe}_2$ for both high symmetry direction and polarization . . . . .	54
3.17	Dy-doping dependence of the pocket's areas. . . . .	55
3.18	Schematic of the Nesting Vector calculation . . . . .	56
3.19	Electron-Hole Nesting Vectors for the $\text{ZrTe}_2$ compound . . . . .	57
3.20	Electron-Hole Nesting Vectors for the Ni-doped compound . . . . .	59
3.21	Electron-Hole Nesting Vectors for the Ni-doped compound . . . . .	60
3.22	Electron-Hole Nesting Vectors for the Ni-doped compound . . . . .	61
A.1	ARPES measurements of $\text{Ni}_{0.05}\text{ZrTe}_2$ flat band states for the $\Gamma\text{K}$ direction . . . . .	74
A.2	ARPES measurements of $\text{Ni}_{0.05}\text{ZrTe}_2$ flat band states for the $\Gamma\text{M}$ direction . . . . .	75
A.3	ARPES measurements of $\text{Ni}_{0.05}\text{ZrTe}_2$ Fermi Maps . . . . .	76
A.4	ARPES measurements of $\text{Dy}_{0.01}\text{ZrTe}_2$ Fermi Maps . . . . .	77
A.5	ARPES measurements of $\text{Dy}_{0.05}\text{ZrTe}_2$ Fermi Maps . . . . .	78
B.1	Strain Device and Wheatstone Bridge . . . . .	80
C.1	Schematic of the Tunneling Process and STM . . . . .	84
C.2	Example of a van Hove singularity . . . . .	86
C.3	Schematic of the graphene structure . . . . .	87
C.4	Schematic of the twisted bilayer graphene . . . . .	88
C.5	STM setup and metallic cover . . . . .	89
C.6	STM setup and metallic cover . . . . .	90
C.7	Schematic of the random potential. Large scale view of the graphene surface. . . . .	91
C.8	Example of a wrinkle and triangular lattice formation . . . . .	91
C.9	Examples of monolayer graphene STM imaging . . . . .	92
C.10	STS measurements of the monolayer sample - complete set . . . . .	93
C.11	Examples of bilayer graphene STM imaging . . . . .	95
C.12	STS measurements of the bilayer sample. 2 V rage scale. . . . .	96
C.13	STS measurements of the bilayer sample. 1 V scale range . . . . .	96

---

C.14 STS measurements of the bilayer sample. 0.6 V scale range . . . . .	97
C.15 Example of a polycrystalline graphene surface . . . . .	99
C.16 Average of the STS measurements. 2 V range scale. . . . .	100
C.17 Average of the STS measurements. 1 V range scale. . . . .	100
C.18 Average of the STS measurements. 0.6 V range scale . . . . .	101

# Chapter 1

## Introduction

This chapter serves as a comprehensive introduction to the category of materials known as Transition Metal Dichalcogenides (TMDs). It offers a concise historical context, delves into their structural composition, and introduces key aspects related to their electronic properties and observed emergent phenomena. Special attention is given to the charge density wave order and its interconnected electronic structure, as these constitute the primary focal points of investigation within the study developed in this work.

### 1.1 Transition Metal Dichalcogenides (TMDs)

Transition Metal Dichalcogenides (TMDs) represent a distinct category of two-dimensional (2D) materials characterized by a general chemical formula  $\text{MX}_2$ , where M denotes a transition metal, and X signifies a chalcogen atom (S, Se, or Te). Their structural arrangement consists of layers featuring a typical X-M-X stacking pattern, characterized by strong covalent bonding within each layer and relatively weaker van der Waals interactions between adjacent layers. This unique structural configuration imparts these materials with intriguing physical and chemical properties, rendering them highly appealing for a wide range of applications, including spintronics, optoelectronics, and flexible electronics [1]. Additionally, TMDs serve as a conducive platform for investigating novel and fundamental physical phenomena. This encompasses the exploration of lattice commensurability effects in Periodic Lattice Distortion/Charge Density Wave (PLD/CDW) transitions, the interplay between ordered phases and topological orders.

The origins of these materials trace back to the early 20th century when Linus Pauling made their initial discovery in 1923. By the late 1960s, numerous distinct Transition Metal Dichalcogenides (TMDs) had been identified. Notably, it was during this period that the first ultrathin layers of  $\text{MoS}_2$  were successfully isolated using adhesive tapes. The milestone of achieving monolayer thickness, also in  $\text{MoS}_2$ , was realized in 1986. However, it wasn't until the emergence of graphene in 2004 that a substantial surge in the development and enhancement of techniques for the investigation and manipulation of layered materials occurred. This catalyzed a resurgence of interest in TMDs, driven by innovative and improved approaches to their study and

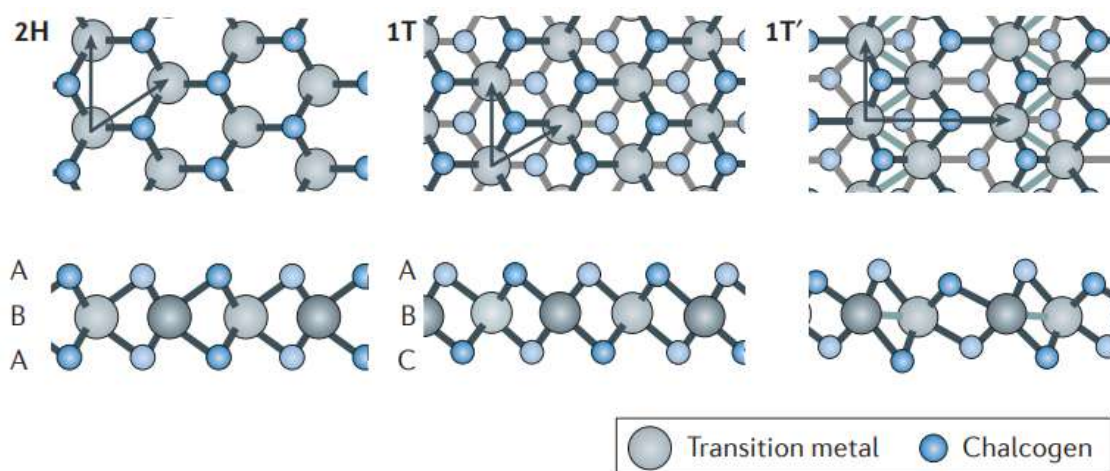


Figure 1.1: Top and side view of the different atomic structure of a single layer of Transition Metal Dichalcogenides (TMDs) in their trigonal prismatic (2H), octahedral (1T) and dimerized (1T') structural phases. The in-plane lattice vectors are indicated in the top view. Image from [1].

exploration.

TMDs predominantly exhibit two structural phases denoted as H (trigonal prismatic) and T (octahedral), classifying the compounds based on the coordination of transition metals, as depicted in Figure 1.1. Typically, a numerical value precedes the phase nomenclature, signifying the stacking sequence of layers within the unit cell, i.e., how many layers are contained within each unit. The 2H phases are characterized by an ABA stacking pattern within the layers, where chalcogen atoms in different planes align directly on top of each other. In contrast, the 1T phases feature an ABC stacking, indicating that chalcogen atoms in different planes are slightly displaced from one another. This stacking distinction is illustrated at the bottom of Figure 1.1.

A crucial aspect of their structural configuration lies in the alteration of periodicity caused by potential distortions. Various types of phase transitions, such as those leading to charge density wave (CDW) ordering, can induce subtle lattice distortions. In certain cases, these distortions may even lead to changes in the chemical bonding within the system, resulting in phenomena like the formation of metal-to-metal bonds. One prevalent example of distorted structure in TMDs is the 1T' phase, where atoms rearrange themselves to create dimers of transition metal atoms. As elaborated upon in Section 1.2.1, this dimerization process can create a complex and intriguing physical scenario.

### 1.1.1 Electronic Structure

It is well known from condensed matter theory [2, 3] that electrons in solids assume discrete energy levels with exceedingly small energy and momentum intervals. When a solid adopts a crystalline structure, the periodic potential generated by its nuclei causes these energy levels to be organized into what we refer to



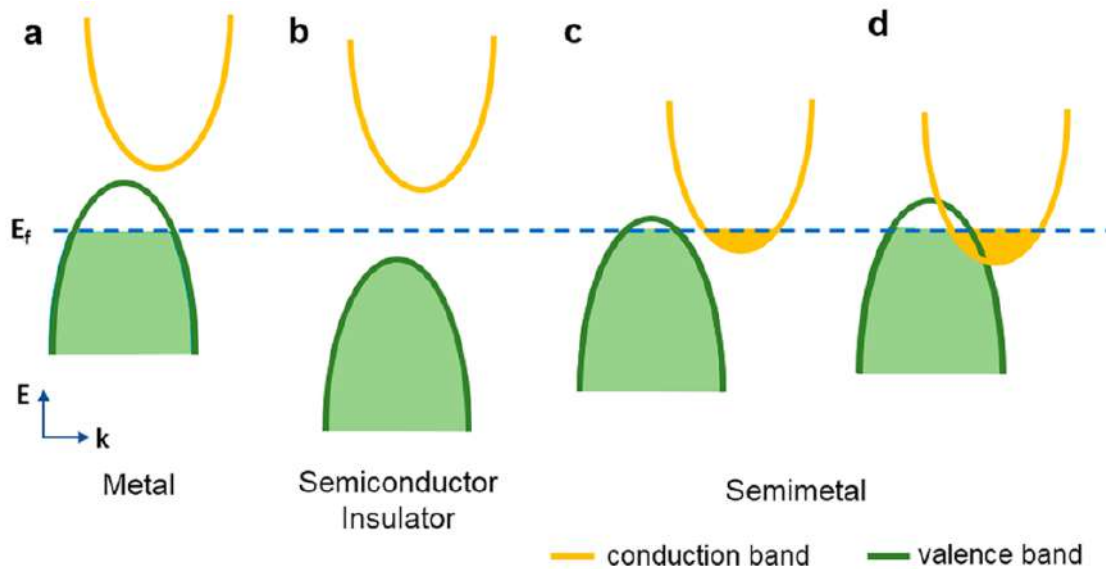


Figure 1.2: Illustrative representation of band structures of a (a) metal, (b) semiconductor/insulator and (c) semimetal in the reciprocal space. Image from [4].

as an electronic band structure, typically delineated in the reciprocal (momentum) space.

This band structure is conventionally divided into conduction and valence bands, similar in concept to unoccupied and occupied energy levels within molecular electronic systems. Various scenarios emerge in the organization of the electronic band structure. In a simplified view, an even number of electrons per unit cell fully occupy a band, whereas an odd number of electrons only partially occupy it. When the valence and conduction bands remain separated by a gap, a material with an even number of electrons behaves as an insulator or semiconductor, depending on the gap size (Figure 1.2b). In such cases, the valence band attains full occupancy. On the other hand, when a system harbors an odd number of electrons within the unit cell, the valence band states remain partially occupied, resulting in a metallic behavior (Figure 1.2a).

In more intricate scenarios, the conduction and valence bands may exhibit a modest overlap, as exemplified in Figure 1.2c and 1.2d. In such instances, the degree of band filling no longer dictates the material's electronic behavior, which generally assumes a metallic nature. These materials often exhibit a low carrier density, which can be either electrons or holes, at the Fermi Surface, categorizing them as semimetals.

While TMDs are commonly categorized as 2D materials, it is important to recognize the significance of weak van der Waals interactions between their layers in comprehending their electronic properties. The number of layers in TMDs often strongly influences their band structure, conferring bulk and monolayer counterparts with distinct properties. The underlying concept is that, even though weak, a relevant interlayer interaction induce steeper band dispersion, potentially leading to the overlap of the conduction and valence bands' extremities. This transformation can shift a semiconducting monolayer's behavior towards metallic attributes when it comes to the bulk material with the same composition. Hence, it is imperative to emphasize

that the out-of-plane band dispersion in TMDs is not merely a negligible factor but a significant determinant of their electronic band structure.

Another interesting facet of TMDs is the emergence of spin splitting within electronic bands, driven by spin-orbit coupling (SOC). This effect arises as the spin degeneracy of valence and/or conduction bands is lifted due to the absence of inversion symmetry, achieved through mechanisms like the Dresselhaus [5] or Rashba [6] effects. Such spin splitting is observable across various TMDs, especially in 2H-compounds, where it manifests at the nonequivalent K and K' points in reciprocal space [1].

### 1.1.2 Crystal Structure, Brillouin Zone and Band Structure of ZrTe<sub>2</sub>

The crystal structure of the Transition Metal Dichalcogenide (TMD) 1T-ZrTe<sub>2</sub>, which is the primary subject of investigation in this study, consists of stacked layers arranged in hexagonal lattices, forming a trigonal structure (Space Group P3m1, number 164), as illustrated in Figure 1.3a. In this structure, Zr atoms have octahedral coordination with the strongly bonded Te layers. Specifically, the chalcogen atoms in the top layer are positioned between the chalcogen atoms in the bottom layer. The unit vectors characterizing this structure can be expressed as follows:

$$\vec{a}_1 = a\hat{x}; \quad \vec{a}_2 = \frac{a}{2}\hat{x} + \frac{\sqrt{3}a}{2}\hat{y}; \quad \vec{a}_3 = c\hat{z} \quad (1.1)$$

where  $a = 3.945 \text{ \AA}$  and  $c = 6.610 \text{ \AA}$ [7]. Thus, we can construct the vectors  $\vec{b}_j$  of the reciprocal space by using the relations:

$$\vec{b}_1 = \frac{2\pi\vec{a}_2 \times \vec{a}_3}{\vec{a}_1 \cdot (\vec{a}_2 \times \vec{a}_3)}; \quad \vec{b}_2 = \frac{2\pi\vec{a}_3 \times \vec{a}_1}{\vec{a}_1 \cdot (\vec{a}_2 \times \vec{a}_3)}; \quad \vec{b}_3 = \frac{2\pi\vec{a}_1 \times \vec{a}_2}{\vec{a}_1 \cdot (\vec{a}_2 \times \vec{a}_3)} \quad (1.2)$$

This yields the reciprocal lattice vectors:

$$\vec{b}_1 = \frac{2\pi}{a}\hat{x} - \frac{2\pi\sqrt{3}}{3a}\hat{y}; \quad \vec{b}_2 = \frac{4\pi\sqrt{3}}{3a}\hat{y}; \quad \vec{b}_3 = \frac{2\pi}{c}\hat{z} \quad (1.3)$$

With these vectors in hand, we can construct the hexagonal Brillouin Zone of the system, which is presented in Figure 1.3b along with the high symmetry points. We now are able to also calculate the high symmetry distances directly. The  $\Gamma\text{M}$  segment is given by  $\frac{|\vec{b}_{1,2}|}{2} = 0.916 \text{ \AA}^{-1}$  or  $1.15 \frac{\pi}{a}$ . Both  $\Gamma\text{K}$  and  $\text{MK}$  segments can be determined by the simple trigonometry relations  $\cos 30^\circ = \frac{\Gamma\text{M}}{\Gamma\text{K}}$  and  $\tan 30^\circ = \frac{\text{MK}}{\Gamma\text{M}}$ . Then, we have  $\Gamma\text{K} = 1.060 \text{ \AA}^{-1}$  or  $1.33 \frac{\pi}{a}$  and  $\text{MK} = 0.529 \text{ \AA}^{-1}$ . These values were used as reference for the data processing discussed in section 3.

Before continuing, it is worth making a short digression in order to discuss some important features which may arise from a hexagonal lattice. We will use the tight binding model from the honeycomb lattice, a simple 2D system that represents the graphene, and see how such geometry brings about an interesting electronic configuration. We start our calculation by considering a Hamiltonian for a system with 1 atom per lattice point [8]:

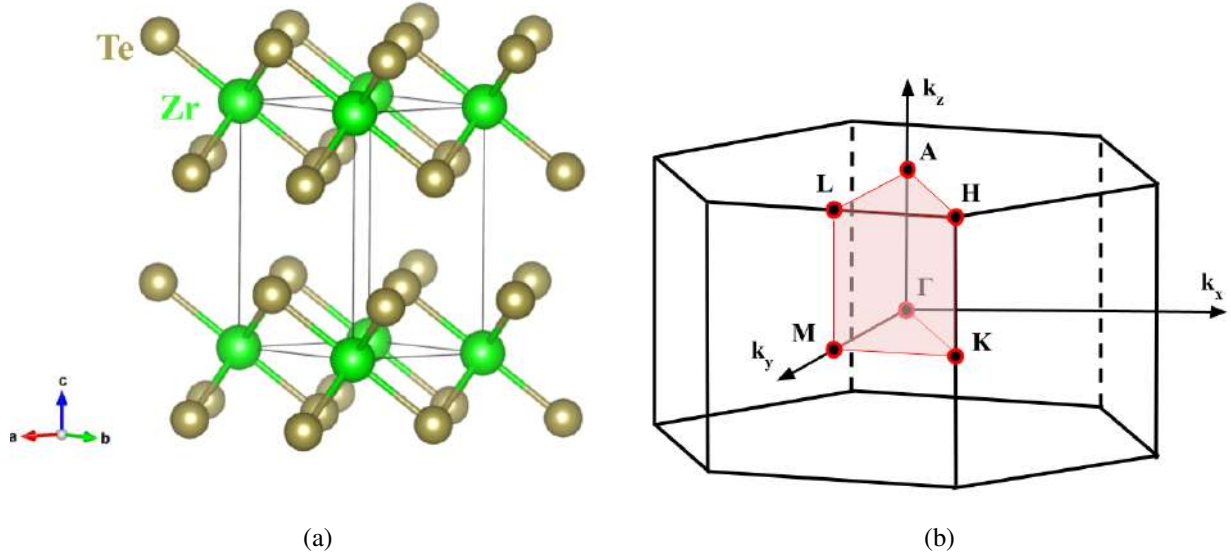


Figure 1.3: (a): Crystal structure of 1T-ZrTe<sub>2</sub>. (b): 3D Brillouin Zone of the system. The high symmetry points are labelled.

$$H = \sum_i E_i |r_i\rangle \langle r_i| - \sum_{ij} |r_i\rangle t_{ij} \langle r_j| \quad (1.4)$$

We can simplify this expression by considering only first neighbors hopping, such that  $t_{ij} = t$ , and that the on site energies are all equal,  $E_i = E_0$ . We have, then,

$$H = E_0 \sum_i |r_i\rangle \langle r_i| - t \sum_{ij} |r_i\rangle \langle r_j| \quad (1.5)$$

For the case of graphene, we have a triangular lattice with a basis of two atoms, which forms the well-known honeycomb structure. If we consider the entire system as being two intertwined triangular lattices, the Hamiltonian writes as,

$$H = E_A \sum_i |r_i, A\rangle \langle r_i, A| + E_B \sum_i |r_i, B\rangle \langle r_i, B| - t \sum_{ij} (|r_i, A\rangle \langle r_j, B| + |r_j, B\rangle \langle r_i, A|) \quad (1.6)$$

where A and B labels the carbon atoms from the different sublattices. Since all atoms in the sublattices are carbon atoms,  $E_A = E_B = E_0$  and we set it to 0 for the moment. Taking the term  $|r_j, B\rangle \langle r_i, A|$  as the hermitian conjugate of  $|r_i, A\rangle \langle r_j, B|$ , we are left with:

$$H = -t \sum_{ij} |r_i, A\rangle \langle r_i + \delta_j, B| + h.c \quad (1.7)$$

where  $\delta_j$  is the vector that connects one atom from the sublattice A to the sublattice B. In order to diagonalize the Hamiltonian, we propose the Ansatz which is the Fourier Transform of the states of each sublattice separately:

$$|r_i, A\rangle = \frac{1}{\sqrt{N}} \sum_{k \in 1^{st} BZ} e^{-ik \cdot r_i} |k, A\rangle \quad \text{and} \quad |r_i + \delta_j, B\rangle = \frac{1}{\sqrt{N}} \sum_{k \in 1^{st} BZ} e^{-ik \cdot (r_i + \delta_j)} |k, B\rangle$$

Substituting these Ansatz back in equation 1.7 we get,

$$H = \sum_k \gamma(k) [|k, A\rangle \langle k, B|] + h.c \quad (1.8)$$

Here, we introduced the quantity,

$$\begin{aligned} \gamma(k) &= -t \sum_j e^{ik \cdot \delta_j} = -t(e^{ik_x a} + e^{ia(k_x + \sqrt{3}k_y)/2} + e^{ia(k_x - \sqrt{3}k_y)/2}) \\ &= -te^{ik_x a} (1 + 2e^{3ik_x a/2} \cos \sqrt{3}k_y a/2) \end{aligned}$$

We have, then, the Hamiltonian matrix:

$$H_{2 \times 2} = \begin{pmatrix} 0 & \gamma(k) \\ \gamma^*(k) & 0 \end{pmatrix} \quad (1.9)$$

which leaves with the eigenenergies:

$$E_{\pm}(k) = \pm |\gamma(k)| \quad (1.10)$$

Let's see now what happens to the band dispersion around the K and K' points of the Brillouin Zone. These points are located at:

$$K = \frac{1}{3}(2b_1 + b_2) = \frac{2\pi}{3a}(\hat{x} + \frac{1}{\sqrt{3}}\hat{y}) \quad K' = \frac{1}{3}(b_1 + 2b_2) = \frac{2\pi}{3a}(\hat{x} - \frac{1}{\sqrt{3}}\hat{y})$$

We expand  $\gamma(k)$  around K +  $\vec{q}$  (and K' +  $\vec{q}$ ):

$$H_{2 \times 2} = \begin{pmatrix} 0 & \gamma(K + \vec{q}) \\ \gamma^*(K' + \vec{q}) & 0 \end{pmatrix} \approx \frac{3}{2}at \begin{pmatrix} 0 & q_x - iq_y \\ q_x + iq_y & 0 \end{pmatrix} = \hbar v_F [\tau^x q_x + \tau^y q_y] = \hbar v_F \vec{\tau} \cdot \vec{q}$$

Here,  $\tau^x$ ,  $\tau^y$  and  $\tau^z$  represent the Pauli matrices. From this development of low energy theory, we find that,

$$E_{\pm}(q) \approx \hbar v_F |q| \quad (1.11)$$

This result is very interesting because this is the energy spectrum of Dirac particles [9, 10, 11]. What is meant is that these equations are analogues of relativistic massless particles from Dirac equations. Therefore, the electronic excitations of graphene in this region reproduce the behavior of Dirac quasi particles. We finish this digression now and go back to discussing the electronic properties of 1T-ZrTe<sub>2</sub>.

The electronic behavior of this material aligns with the characteristics expected for a semimetal. The Fermi surface manifests as a result of bands with Zr-4d and Te-5p orbital character, giving rise to one electron pocket located at the M(L) point and two hole pockets situated at the  $\Gamma$ (A) point [7]. These features are illustrated in the first-principle calculations presented in Figure 1.5a.

Recent studies have demonstrated that zirconium telluride materials also exhibit band splitting associated with SOC [12]. It is suggested that SOC induces an inversion between the Te-p and Zr-d band characters in the proximity of the  $\Gamma$  point [13, 14]. This symmetry-breaking mechanism may give rise to non-trivial band topologies, including 3D/2D Dirac and Weyl semimetals, as well as topological insulators [15, 16]. Moreover, it has been experimentally demonstrated that thin films of 1T-ZrTe<sub>2</sub> exhibit gap opening at the  $\Gamma$  point due to SOC effects. This results in the formation of a linear dispersion band, indicating the presence of massless Dirac Fermions [17, 12].

Due to these distinctive attributes, there has been a growing interest in exploring the physical properties of this material as a versatile platform for novel and intriguing physical phenomena. Recent investigations have unveiled the remarkable effects of intercalation within the van der Waals gap [18, 7], as well as hole doping [19], which have led to the emergence of unconventional superconductivity. Additionally, a noteworthy study has revealed that ZrTe<sub>2</sub> monolayers undergo a low-temperature ( $T_c = 130 \pm 20$ ) Charge Density Wave (CDW) phase transition [20], driven by excitonic condensation rather than the conventional electron-phonon coupling mechanism. This finding positions it as a promising Excitonic Insulator candidate material, a topic to be discussed with more detail in Section 1.2.5.

Inspired by the intriguing findings reported in Ref. [7], this project was conceived with the primary objective of conducting an exploration into the electronic structure of ZrTe<sub>2</sub> intercalated with both Ni and Dy using Angle-Resolved Photoemission Spectroscopy (ARPES). Figure 1.5b showcases the calculated Density of States (DOS) for varying levels of Ni intercalation. The emergence of a narrow peak in the density of states indicates the formation of localized, nearly flat bands situated in proximity to a binding energy of  $-1.0$  eV.

Furthermore, Ref. [7] presented resistivity and specific heat measurements, consistent with a phase transition occurring at approximately  $T = 285$  K, suggested as a Charge Density Wave (CDW) transition. In addition, at about  $T = 4$  K, there is a zero-resistance transition accompanied by diamagnetic transition at the same temperature, suggesting the onset of a superconducting ground state. Remarkably, heat capacity

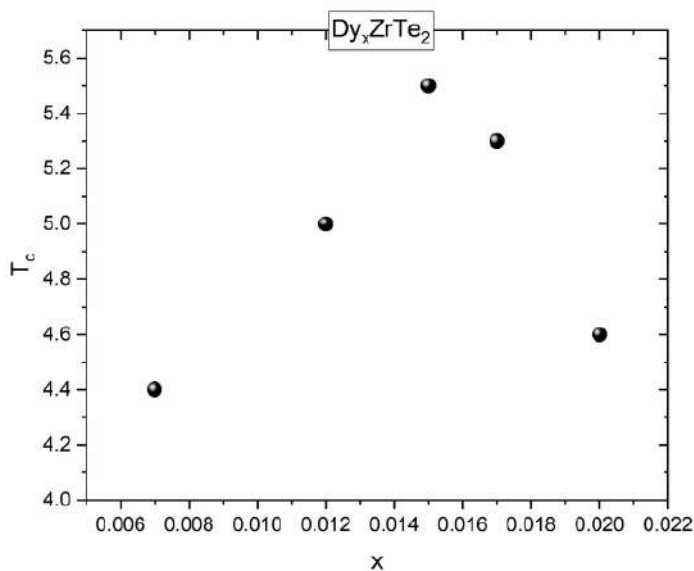
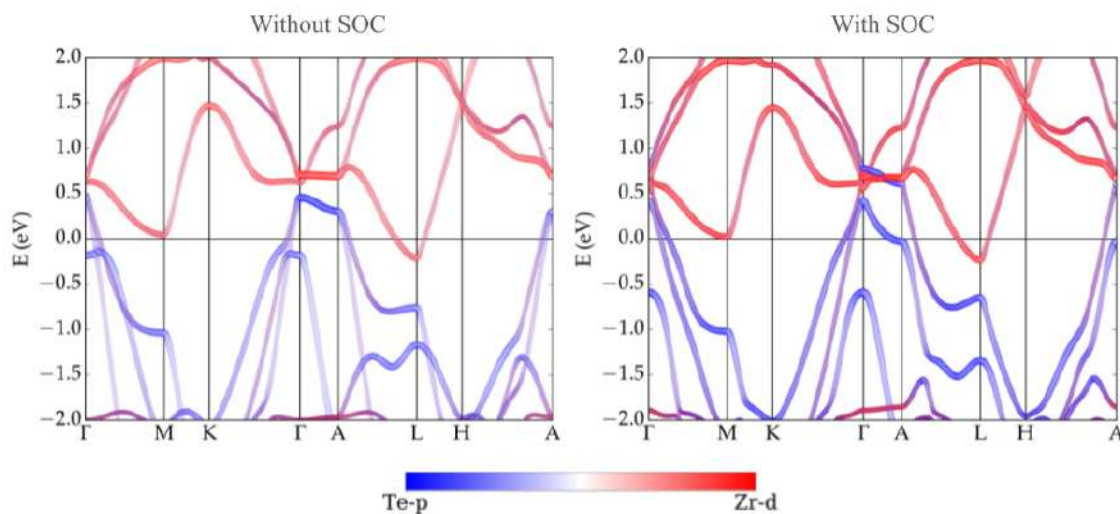


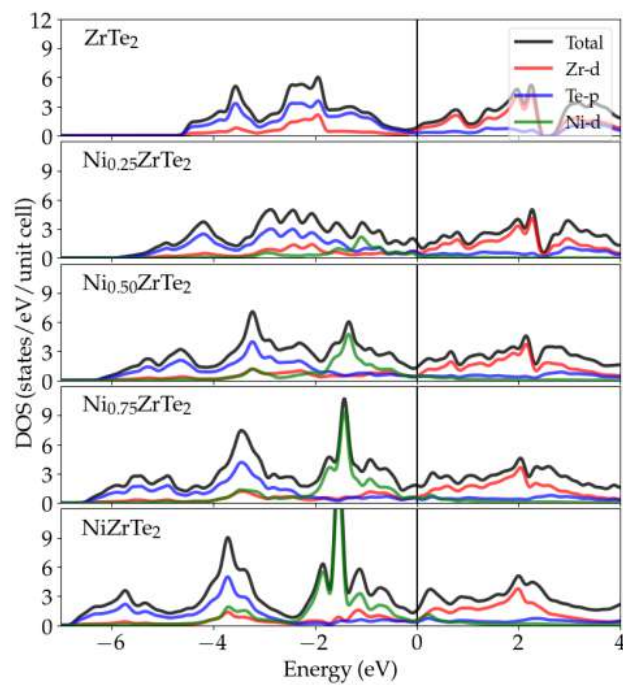
Figure 1.4: Superconducting Phase Diagram of Dy-doping  $\text{ZrTe}_2$ . From Ref [21]

measurements at this temperature do not exhibit a corresponding phase transition. This leads to the intriguing hypothesis that superconductivity may be confined to the material's surface or that it may manifest as a gapless superconducting state. We thus decided to carry out an investigation of the electronic structure of Ni-intercalated  $\text{ZrTe}_2$  by ARPES.

As for the Dy-intercalation, Figure 1.4 offers a comprehensive composition ( $x$ ) versus temperature ( $T$ ) phase diagram derived from resistivity and susceptibility measurements of the samples. Notably, this phase diagram exhibits a distinct superconducting dome. Within this context, we investigated the electronic structure of distinct compositions of Dy-intercalated samples.



(a)



(b)

Figure 1.5: (a): *ab-initio* calculation of the electronic structure without (left) and with (right) spin-orbit coupling of the  $\text{ZrTe}_2$ , with the orbital composition. (b): Density of States calculation for different Ni-doped  $\text{ZrTe}_2$  compounds. Both figures from Ref [7].

## 1.2 The Charge Density Wave Phenomenon

Electrons in most metals are typically treated as free particles. In a simplified model, they experience mutual repulsion due to their negative charge while being simultaneously attracted to the positively charged ions constituting the material. These opposing forces tend to reduce electronic interactions. In such scenarios, the resulting charge density can be considered nearly homogeneous throughout the system in real space.

Now, let's explore a scenario where the arrangement of positive ions undergoes some sort of distortion, subsequently affecting the positions of electrons. This change in the system's configuration gives rise to an effective interaction between electrons. Frequently, these interactions lead to the pairing of electrons, resulting in the formation of an ordered structure characterized by a novel spatial charge distribution formed by these electron pairs, which mutually repel each other. This makes the charge density to increase at the pairs locations and decrease elsewhere. This phenomenon is commonly referred to as a Charge-Density Wave (CDW) [22].

### 1.2.1 Peierl's Picture

This ordered phase was initially postulated by the physicist Rudolph E. Peierls in the early 1930s [23]. He noted a fundamental instability in one-dimensional metals. To elucidate this instability, let's contemplate a one-dimensional atomic chain model consisting of atoms equally spaced apart by a lattice constant  $a$ , as depicted on the left side of Figure 1.6a. In this model, each atomic site hosts a single electron, and we adopt a free electron picture, leading to a quadratic band structure. Consequently, the band filling extends up to the Fermi points situated at  $k_F = \pm\pi/2a$ , connected by the vector  $q = 2k_F$ .

Through Second Order Perturbation Theory [24], it is possible to demonstrate that introducing a disturbance to the system results in the electrons occupying states with lower total energy. This phenomenon leads to the opening of a band gap in the system's structure. Alternatively, employing the Tight Binding Model provides an intuitive understanding: a lattice distortion that doubles the periodicity leads to a lower total energy state compared to an undistorted scenario. This occurs because the distortion changes the atomic periodicity of the chain to  $2a$ , creating a new unit cell with two atoms and opening a gap at the Brillouin Zone boundaries ( $k = \pm\pi/2a$ ), shifting it to  $k_F$ . The energy required for the distortion is compensated by the gain in electronic energy, establishing this configuration as the new ground state of the system. The right side of Figure 1.6a illustrates the modified atomic chain and the new electronic band structure after the transition.

It is important to emphasize that the increase in electronic energy must outweigh the cost of restructuring the atomic lattice for the transition to occur, meaning that  $\delta E_{band} + \delta E_{lattice} < 0$  for a given phonon mode. In the simplified framework of independent electrons, harmonic and adiabatic approximations, the mean-field theory of a 1D electron-lattice system in the weak-coupling limit yields an instability condition [27] derived from microscopic parameters:



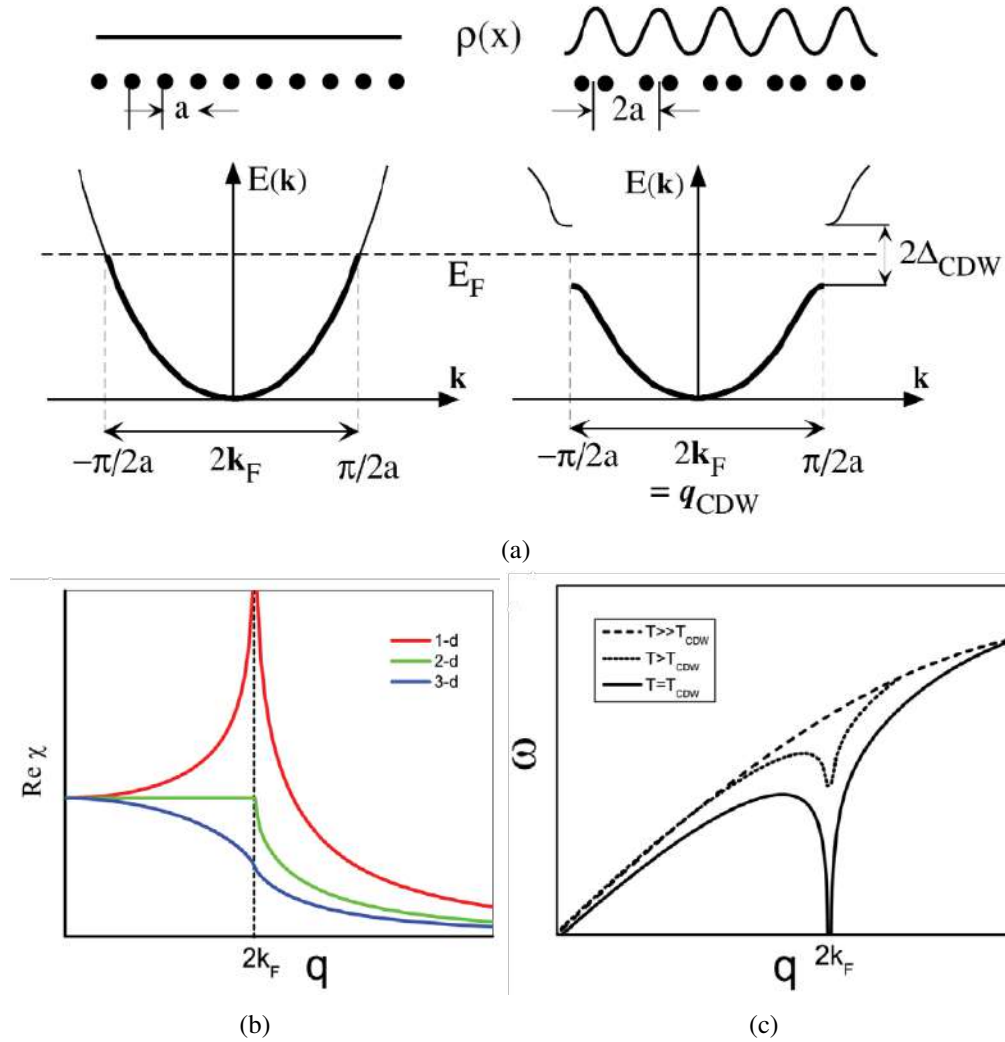


Figure 1.6: (a): Peierls Distortion in 1D. The initial system is a linear chain of monovalent atoms with periodicity  $a$ , forming a metal (left side). Then, the system is distorted in such a way that the new periodicity is doubled, opening a gap in the electronic states which compensate for the increase in the elastic energy of the deformation (right side). Image from Ref [25]. (b): Graphs depicting the real component of the Lindhard function across 1D, 2D, and 3D models of free electron gases. (c): Variation in phonon energy within a 1D atomic chain at different temperatures. Both (b) and (c) images from Ref [26].

$$\frac{4g_k^2}{\hbar\omega_k} - 2U_k + V_k > \frac{1}{\chi_0(k)} \quad (1.12)$$

where  $g_k$  is the electron-phonon coupling constant,  $\omega_k$  is the frequency of the phonon normal mode,  $\chi_0(k)$  is the non-interacting electronic susceptibility,  $U_k$  is the Coulomb interaction and  $V_q$  is the screened exchange interaction.

While the condition presented in Equation 1.12 employs some strong simplifications, it encapsulates key

insights into the formation of CDWs. First, it underscores the significance of robust interactions between electrons and phonons ( $g_k$ ) as well as electron-electron exchange interactions ( $V_k$ ). Secondly, it emphasizes the necessity of weak Coulomb interactions ( $U_k$ ) and phonon mode softening (small  $\omega_k$ ). Additionally, it highlights the importance of an augmented non-interacting susceptibility (large  $\chi_0(k)$ ). Notably, the divergence of  $\chi_0(q = 2k_f)$  is what causes the phonon mode with a wave number around  $2k_F$  to undergo a renormalization to a lower energy state, which means that the phonon softening is a consequence of the electronic instability. Figure 1.6b and 1.6c illustrates both the electronic susceptibility's divergence and phonon softening, respectively.

Within this framework, it becomes possible to establish a connection between the zero-temperature energy gap, assuming a tight-binding band, and the transition temperature (mean-field) [27] with the relation  $2\Delta(0) = 3.52k_B T_c$ . This equation implies that thermal excitation of electrons remains insufficient to raise the total energy beyond a certain threshold. As the system transforms from a metal to an insulator due to the emergence of a gap at the Fermi Level at  $T_c$ , there is a metal-to-insulator transition, commonly referred to as Peierls's Transition.

### 1.2.2 Fermi Surface Nesting

Although the preceding depiction captures several crucial aspects of Charge Density Waves, it's important to acknowledge its inherent limitations stemming from various approximations. An intriguing facet closely tied to TMDs warrants further examination - the dimensionality of the system. To elucidate the emergence of CDWs in systems with higher dimensions, we can extend Peierl's model to incorporate the concept of Fermi Surface Nesting (FSN). When the topology of the Fermi Surface is structured in such a way that it allows different segments of the Fermi Surface to align through translation by a fixed vector  $\mathbf{q}_{CDW}$ , a CDW state can manifest with a spatial periodicity of  $2\pi/|\mathbf{q}_{CDW}|$ .

In the 1D scenario, the Fermi Surface comprises only two points, ensuring that a vector  $\mathbf{q}_{CDW} = 2k_F$  always connects the entire Fermi Surface, resulting in complete nesting. In 2D systems, the Fermi Surface resides within a 2D plane in k-space. For free electrons, the Fermi Surface adopts a circular shape, and only an infinitesimal portion (two points) can be nested for a given vector. Ideally, the Fermi Surface should exhibit parallel segments to facilitate nesting, but this condition is rarely met in real systems. A more realistic scenario, particularly for 2D TMDs, is when the Fermi Surface assumes an elliptical shape. In such cases, quasi-parallel segments may exist, inducing the system into a distorted phase along the nesting direction. Figure 1.7 provides an illustration of the nesting phenomenon for these three examples.

We can observe that the scenario of Fermi Surface (FS) nesting is highly dependent upon the specific shape of the Fermi Surface itself. Furthermore, it's worth commenting on the limitations inherent in this picture. For instance, we must acknowledge that the significance of the Fermi Surface becomes less pronounced when we deviate from the weak-coupling regime (Electron-Phonon Coupling or EPC). As the coupling strength increases, so does the energy gap ( $\Delta/E_F \lesssim 1$ ), resulting in the characteristic energy gain,  $\delta E_{band}$ , becoming proportional to  $\Delta$  and spreading throughout the entire Brillouin Zone (BZ). In this sce-

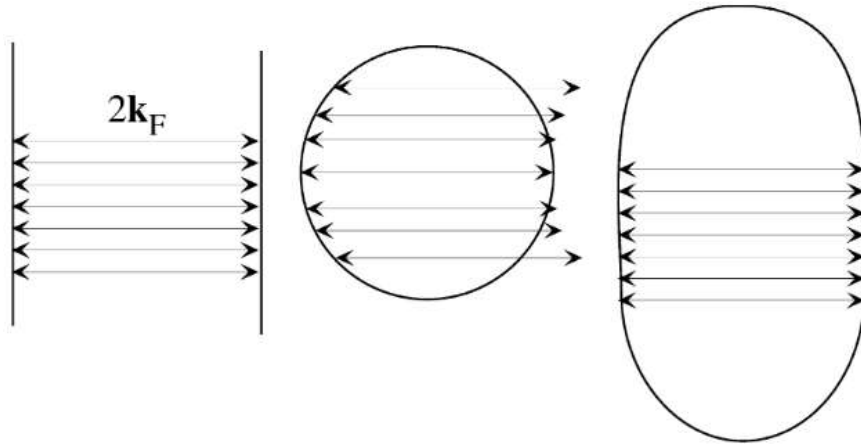


Figure 1.7: From left to right, we have 2D FS with completely parallel segments; the free-electron case, which is a circle; and an ellipse, that can feature quasi-parallel portions. Image from Ref [25].

nario, the energy gain is no longer localized in  $k$ -space, effectively diminishing the relevance of the Fermi Surface.

Another important limitation to consider is the impact of dimensionality on the non-interacting electronic susceptibility ( $\chi_0(k)$ ). In higher dimensions ( $D > 1$ ), the characteristic logarithmic divergence of  $\chi_0(k)$  transforms into a smooth peak, the features of which, such as its height and position, heavily rely on the configuration of nested portions of the Fermi Surface.

### 1.2.3 Excitonic Insulator

Beyond the scenario discussed in the previous section, another phenomenon of great importance in the realm of Charge Density Waves (CDWs) is the emergence of quasiparticles known as excitons. They represent a bound state formed between an electron and a hole, which is formed when an electron is excited from the valence band to a state within the conduction band, as shown in Figure 1.8b. The electron carries a negative charge, while the hole, essentially the vacancy left behind by the electron, bears a positive charge. Thus, an attractive Coulomb interaction arise between them, resulting in the formation of an electron-hole pair referred to as an "exciton".

The groundwork for this scenario was initially laid by Yakov Frenkel in 1931, during his investigation of the light absorption process in crystals [28]. Subsequently, Gregory H. Wannier (1937) [29] and Nevill Mott (1961) [30] expanded upon this concept while exploring the tuning of excitation levels in insulators and semiconductors. The former, known as Frenkel excitons, are characterized by strong binding, which stands in contrast to the latter, known as Wannier-Mott excitons, in which the coupling is weaker [31].

It turns out that, below a critical temperature, the systems total energy will be lowered by the formation of excitons, which start to form spontaneously. This phenomenon is particularly favored in semimetals, where

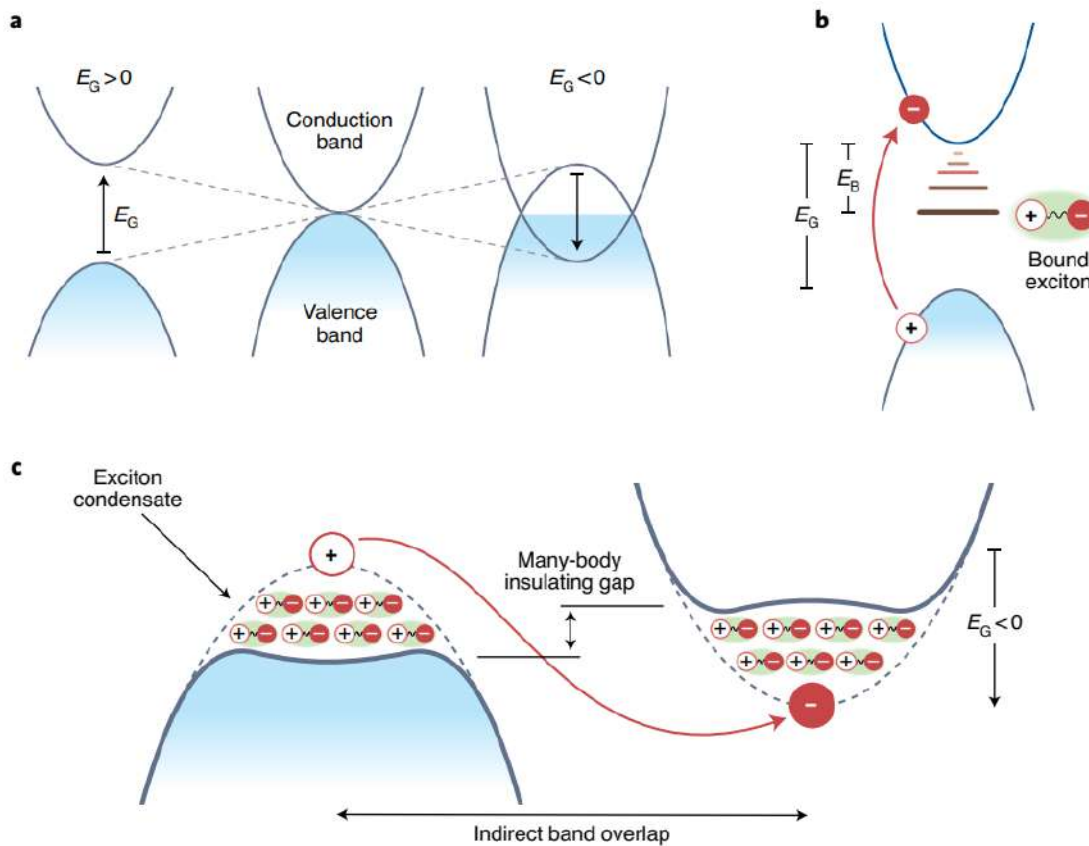


Figure 1.8: (a): Schematic view of an semiconductor with positive gap ( $E_G > 0$ ), no gap ( $E_G = 0$ ) and negative gap ( $E_G < 0$ ), from the left to the right, respectively. (b): For the case of a semiconductor, the particle-hole are a composite system bind together by the Coulomb interactions. This is an exciton, a boson, with binding energy  $E_B$ . (c): Below a certain critical temperature, the formation of excitons can occur spontaneously if the bands overlap (non-interacting bands are the dashed parabolas). This such scenario leads to an excitonic insulator. Image from Ref [32].

the bandgap is negative. By reducing the number of charge carriers to a sufficiently low level, electronic screening diminishes, allowing the Coulomb attraction between the electron and the hole to become strong enough to stabilize bound states. As excitons consist of two fermions - a conduction electron and a valence hole - they collectively behave as bosons, which means they can form a Bose-Einstein condensate. Therefore, the system's new ground state transitions into an insulating many-body exciton condensate. Figure 1.8c illustrates the scenario of excitonic insulator reconstruction in a semimetal.

The excitonic insulator phase exhibits several distinctive characteristics. It induces the formation of either a Charge Density Wave (CDW) or a Spin Density Wave (SDW), depending on the total spin ( $S$ ) of the soft mode -  $S = 1$  leads to an antiferromagnetic SDW, while  $S = 0$  results in a CDW. These alterations in the band structure are coupled with the potential for lattice distortion, depending on the nature of the electronic density wave. In the case of a CDW, the electron-phonon coupling is strong, causing a Periodic

Lattice Distortion (PLD). Importantly, this CDW and its associated PLD are by-products of the electronic instability induced by electron-electron interactions, particularly the formation of electron-hole bound states. This is different from the Peierl's instability-induced CDW/PLD, which arises from electronic instabilities described by a non-interacting susceptibility which, in turn, also causes a softening of the phonon modes and associated PLD.

In recent years, extensive research has demonstrated that Transition Metal Dichalcogenides (TMDs) serve as a promising platform for investigating excitonic effects [33, 34, 35]. Their two-dimensional character and weak dielectric screening give rise to enhanced Coulomb interactions, creating a favorable environment for the formation of strongly bound electron-hole pairs (excitons) upon optical excitation with binding energies in the range of few hundred meV. Remarkably, these excitonic properties persist even at room temperature in some instances. This unique characteristic has intensified interest in TMDs for potential applications in optics and optoelectronics [36].

#### 1.2.4 Experimental Signatures of the CDW phase in 1T-TaS<sub>2</sub>, 2H-TaSe<sub>2</sub> and 1T-TiSe<sub>2</sub>: an ARPES overview

In this section, we delve into the experimental features related to the Charge Density Wave (CDW) phase within the family of layered transition-metal dichalcogenides (TMDs). Specifically, we'll focus on the characterization of 1T-TaS<sub>2</sub>, 2H-TaSe<sub>2</sub>, and 1T-TiSe<sub>2</sub> using Angle-Resolved Photoemission Spectroscopy (ARPES). These materials have been extensively studied since the 1970s [37], employing various experimental techniques like specific heat and transport measurements to characterize the phase transition, as well as X-ray, scanning tunneling microscopy, electron and neutron diffraction to examine structural changes. Additionally, optical and scanning tunneling spectroscopies, along with angle-resolved photoemission spectroscopy, provide insights into their electronic properties and spectra.

In Figure 1.9 we can see the atomic displacements associated to the commensurate CDW/PDL phase in these compounds. In the case of 1T-TaS<sub>2</sub>, a cluster of 13 Ta atoms forms a "Star of David" arrangement below the transition temperature ( $T_c = 183$  K), resulting in a  $\sqrt{13} \times \sqrt{13}$  reconstruction. These displacements are around 0.2 Å, primarily confined to the plane, while S atoms exhibit smaller displacements, approximately 0.1 Å, mostly perpendicular to the atomic sheet [38]. For 2H-TaSe<sub>2</sub>, a commensurate transition occurs at 90 K, leading to a  $3 \times 3$  reconstruction. Ta atoms are rearranged into a 7-atom cluster resembling the "Star of David" configuration of 1T-TaS<sub>2</sub> [38], as shown in the middle of Figure 1.9. In-plane atomic displacements are notably smaller, even at temperatures as low as 5 K, at approximately 0.05 Å and 0.01 Å for Ta and Se atoms, respectively. Se atoms exhibit an out-of-plane distortion of about 0.02 Å. Lastly, the 1T-TiSe<sub>2</sub> compound undergoes a commensurate superlattice formation at around 202 K, resulting in a  $2 \times 2 \times 2$  reconstruction. The in-plane displacements of Ti and Se are approximately 0.09 Å and 0.03 Å, respectively [39].

Having provided a brief overview of the periodic lattice distortion in these materials, we can now explore the changes in ARPES spectra induced by the CDW/PDL phases. We start with the 1T-TaS<sub>2</sub> compound. In

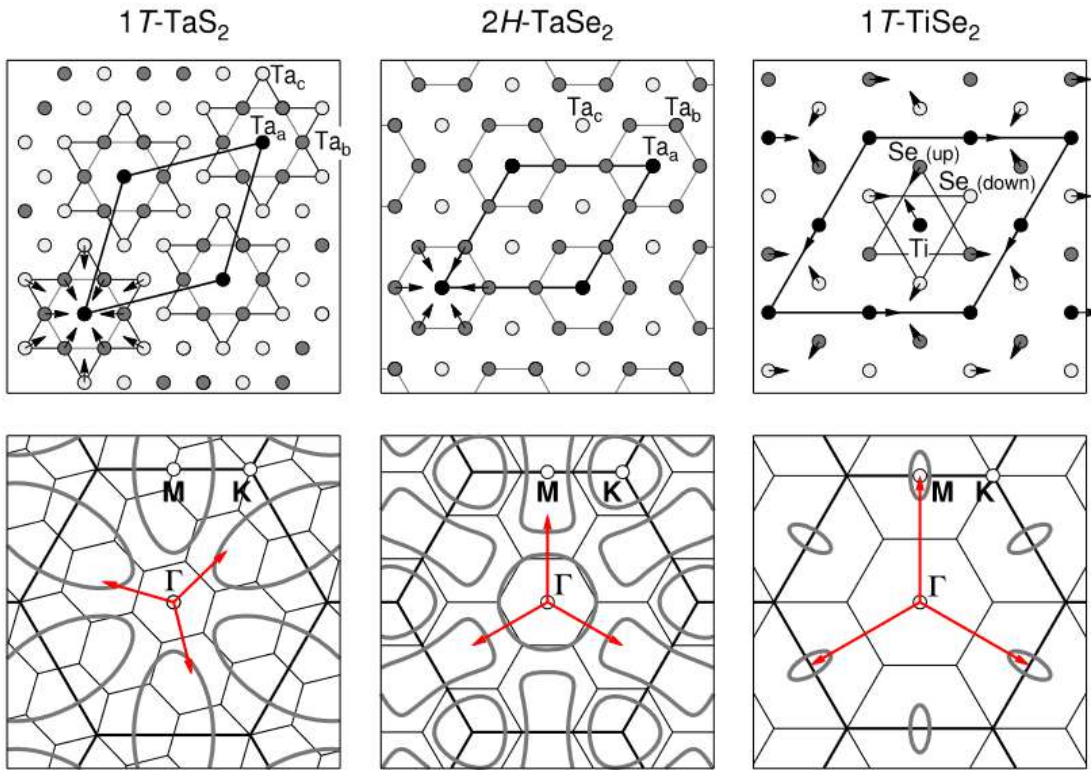


Figure 1.9: Real-space unit cells and their respective BZ for the commensurate  $\sqrt{13} \times \sqrt{13}$  (left),  $3 \times 3$  (middle) and  $2 \times 2$  (right) superlattices. Black arrows indicate the in-plane displacements of atoms. Red arrows indicate the in-plane CDW wavevectors and the gray contours illustrate the topology Fermi Surface in the normal phase. Image from Ref [27].

Figure 1.10-left, we observe a single band dispersion of Ta 5d-states crossing the Fermi Level at the  $\Gamma$  point (Brillouin Zone center), descending to a higher binding energy at the M point (Brillouin Zone boundary), and then crossing the Fermi Level again along the M-K direction. This creates an elliptical pocket at the Fermi Surface around M, as depicted in Figure 1.9. Below the transition temperature, this band divides into numerous gapped submanifolds, transforming the Fermi Surface into a complex structure with multiple small pockets, resulting from a set of undulating bands. This scenario is illustrated in Figure 1.10-right through a tight-binding model calculation [27]. It's worth noting that ARPES measurements may not resolve the fine band structure expected from the theoretical calculation, as evident in Figure 1.10, making the correct assignment of spectral weight distribution challenging.

In the case of 2H-TaSe<sub>2</sub>, the CDW/PDL phase transition reveals clearer features. A comparison of Fermi Surfaces in the normal and CDW phases showcases distinct topologies. Above the transition temperature, the Fermi Surface comprises two hole-like pockets around the  $\Gamma$  and K points and one electron-like pocket around M. As the system transitions into the commensurate CDW phase, the K and M pockets are partially

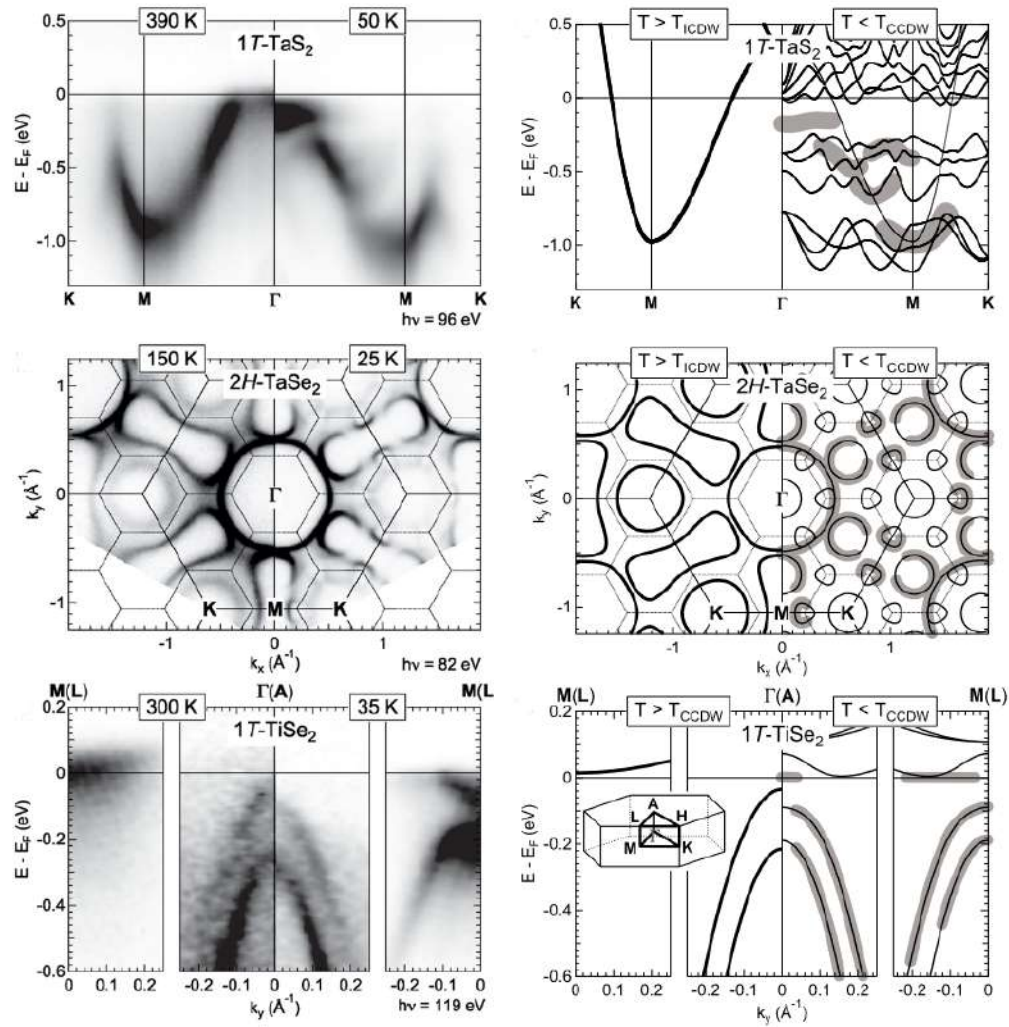


Figure 1.10: Left Side: Experimental ARPES measurements of the electronic structures of 1T-TaS<sub>2</sub>, 2H-TaSe<sub>2</sub> and 1T-TiSe<sub>2</sub>, in the normal phases (left) and in the commensurate CDW phases (right). The corresponding temperature and photon energies are indicated. For the 2H-TaSe<sub>2</sub> case, the Brillouin Zones for the 1 × 1 (solid lines) and 3 × 3 (dotted lines) superlattices are indicated. Right Side: Schematic electronic structures of 1T-TaS<sub>2</sub>, 2H-TaSe<sub>2</sub> and 1T-TiSe<sub>2</sub> in the normal and CDW phases (respectively, left and right sides). The thick gray lines highlight the band structure features that carry significant spectral weight in the CDW phases. The inset shows the 3D Brillouin Zone. Image from Ref [27].

broken, as small bandgaps appear, while the  $\Gamma$  pocket is preserved. This results in a reconstructed Fermi Surface consisting of circular pockets around the  $\Gamma$  points of the new Brillouin Zone and smooth triangular pockets around the new K points, as observed in Figure 1.10. Furthermore, the spectral weight is notably higher around the normal state  $\Gamma$  pocket than regions contributing to the reconstructed Fermi surface pockets.

The final example is the 1T-TiSe<sub>2</sub> system. In the normal state, the band structure comprises a hole-like valence band formed by Se 4p-states, peaking around the  $\Gamma$  point, and an electron-like conduction band of

Ti 3d-states, with a minimum around the L point. Below the transition temperature, a reconstruction of the electronic states occurs, such that the  $\Gamma$  and L points of the normal state Brillouin Zone become equivalent  $\Gamma$  points in the new Brillouin Zone. This leads to interactions between Se 4p and Ti 3d bands, resulting in a gap opening at that region. Moreover, the Se 4p valence band flattens at the top, and folded valence bands emerge at the L point, features that characterize the CDW/PLD transition in this compound.

The preceding discussion on these compounds serves to highlight ARPES signatures expected during a CDW/PDL phase transition. We have seen that the characteristic bandgap in the electronic spectrum is not necessarily located at the Fermi Level. It may happen at  $E_F$ , as is the case of 2H-TaSe<sub>2</sub>, but even then it is not uniform and is very likely to present a dependency on the momentum. Frequently, the CDW gap is situated between new states emerging with the transition, typically at higher binding energies, as exemplified by 1T-TaS<sub>2</sub> and 1T-TiSe<sub>2</sub>. Another significant feature is related to the spectral weight of the new band dispersion. It is expected that the reconstructed electronic structure predominantly exhibits spectral weight around the original bands from the normal phase, while the complete band folding is usually only partially detected as faint shadows in remote regions relative to the original electronic states.

### 1.2.5 The case of the monolayer 1T-ZrTe<sub>2</sub>

A very important system for this work, which also requires a separated discussion is the monolayer (ML) variant of 1T-ZrTe<sub>2</sub>, a potential excitonic insulator candidate. This compound serves as the two-dimensional counterpart to our primary material of interest, the bulk 1T-ZrTe<sub>2</sub>, which description and characteristics are presented in Chapter 3. Notably, 1T-ZrTe<sub>2</sub> bears striking similarities to 1T-TiSe<sub>2</sub>, one of the previously discussed compounds. However, intriguingly, the bulk material lacks any Charge Density Wave (CDW) behavior, whereas the reduction to few layers brings about the emergence of a CDW. The underlying premise is that reducing dimensionality enhances exciton formation by mitigating the influence of electronic screening within the system.

ARPES and STM measurements have unequivocally demonstrated that this system exhibits a 2x2 CDW ground state, accompanied by pronounced spectral weight redistribution and band folding [40, 20]. Figure 1.11a showcases energy maps that chart the evolution of band folding with temperature. Interestingly, the authors from Ref [20] argue that the CDW phase in this material undergoes a two-step process. Initially, an exciton gas forms well above the transition temperature,  $T_c = 130 \pm 20$  K, and then, an exciton condensate is formed, leading to the CDW transition. This phenomenon is discerned in their study through the pronounced spectral weight transfer in the first valence band at the  $\Gamma$  point, a feature persisting even at temperatures significantly above  $T_c$ . This distinctive characteristic stands in contrast to other CDW indicators, including the bandgap size, the intensity of the folded second valence band, and the prominence of the 2x2 superlattice peaks, all of which vanish shortly above  $T_c$ .

As discussed by the authors, this intermediate state can be attributed to the fact that excitonic interaction is more energetically favored due to the exciton forming between the conduction and valence bands near the Fermi level ( $E_F$ ). This favorable energy dynamics result in the binding energy overlapping with the



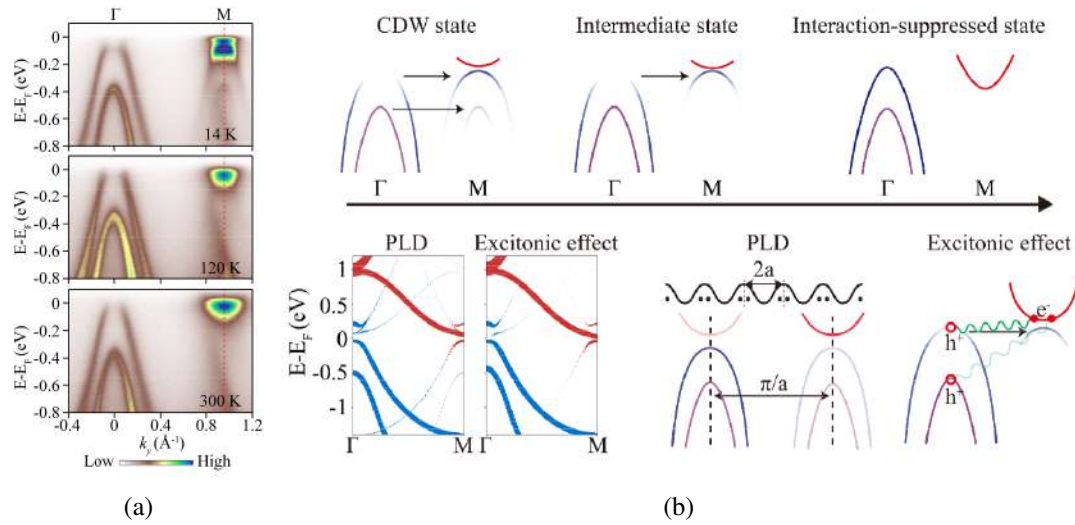


Figure 1.11: (a): ARPES energy maps measured for the  $\Gamma$ M direction at 14 K, 120 K and 300 K. (b): Upper panel: Schematic representation of the band structure from the normal to the CDW state. Lower panel: Schematic diagram of the effects of both PLD and exciton formation in the electronic structure. Each one leads to a different SW redistribution. Images from Ref [20].

bandgap, a process that predominantly concentrates the electronic structure hybridization on the top of the valence band and the bottom of the conduction band. Consequently, an intermediate state materializes, lying between the normal and CDW phases. Figure 1.11b provides a schematic representation of the transition from the normal to CDW phase, passing through the intermediate state, while also delineating the expected spectral weight associated with each phase.

Further temperature reduction culminates in the excitonic condensation of the pre-existing exciton gas, instigating the establishment of a long-range CDW order, which incidentally triggers periodic lattice distortions. The hallmark characteristic defining CDW formation is the folding of the second valence band, a phenomenon solely observable below  $T_c$ . Consequently, the monolayer 1T-ZrTe<sub>2</sub> emerges as an exceptionally promising candidate material for the Excitonic Insulator, showcasing intricate phase transitions and distinct spectral features.

### 1.3 Flat Bands

As discussed in section 1.1.1, electrons in materials form energy bands, which have many different forms of dispersion in the  $k$ -space. When this dispersion features regions where the energy levels are all - or almost all - the same, we call this portion a "flat band". This type of narrow energy dispersion, when located at the vicinity of the Fermi Level, are of very much interest since they may allow electrons to manifest many different physical phenomena, leading the system into a strong correlated state.

In order to have a better idea about this kind of physics we can use a simple model of a quasi-one-

dimensional diamond chain, as illustrated in Figure 1.12a. The unit cell contains three atoms, two of them on the edges ( $m=1,3$ ) and one of them in between those ( $m=2$ ). In terms of a tight binding picture, we consider a hopping  $t$  between the central and border sites of diamonds and one other hopping  $t'$  between the border atoms [41]. The nearest-neighbor hopping term  $t$  is set to be the unit of energy, i.e,  $t = 1$ . In this model, we are not considering the on-site repulsive interaction. The Hamiltonian of such system give us the eigenvalues  $\epsilon_{1,2} = \pm(4(1 + \cos(k)) + t'^2 \cos(k))^{1/2} + t' \cos(k)$  and  $\epsilon_3 = 2t' \cos(k)$ . This way, we can compare how the change in the interapex hopping term  $t'$  affects the band structure of the system, as shown in Figure 1.12b.

Within this picture, we can understand the emergence of a flat band as the interplay between the hopping integrals. For isolated atoms, the energy levels are discrete, as we bring the atoms close together, forming the linear chain, there is an overlap of the atomic orbitals in different atoms, which allows for the "hopping" of electrons between them. First, by setting  $t' = 0$ , we turn off this overlap between the border atoms and the flat band is formed from  $\epsilon_3$ , which have a very high localization because of the lack of orbital overlap. On the other hand, as  $t' \rightarrow 1$ , the overlap of these states becomes stronger, allowing for an intense hopping. However, the states formed by  $\epsilon_2$  now start to get more and more narrow, as if there was a destructive interference of the overlap, blocking one channel of electrons from hopping.

In terms of the new physics that such localization may bring into the system, the core idea is that since  $\frac{\partial E(k)}{\partial k} \propto v_g(k)$ , the charge carrier's group velocity at flat bands is very slow. Thus, the kinetic energy associated to this electronic state,  $E_{kin}$ , is decreased to a point where it is surpassed by the Coulomb repulsion,  $U$ , between electrons in the system. In this sense, the system is now a correlated electron system. Indeed, one should always have in mind that a system with "weak correlations" is a system for which  $E_{kin}$  dominates over  $U$ . For electronic states in a flat band, this is certainly reversed and the electron-electron interactions now dominates the Physics. It can given rise to strong correlated phases of matter, such as Mott insulators or charge and spin density waves.

In order to further illustrate how these quantities may induce the emergence of correlated states, lets take as an example the simple picture of two interacting electrons [42]. If we consider such an interaction to be positive, as it is in the case of Cooper pairs from the BCS theory, the energy associated to the bound state of such electron pair is given by  $E_b = 2E_k - E$ , where  $E_b$  is the bound energy,  $E_k$  is the free electron energy and  $E$  is the total energy. The bound state between the electrons requires that  $E < 2E_k$ . Since the free electron energy is purely kinetic, this give us an intuition on how these quantities play out in order to induce the emergence of such a phase.

Another important aspect of the flat bands is related to the density of states (DOS) of the system. The increase of the DOS around the Fermi Level, which is intimately related to the electronic band dispersion, can enhance electronic correlations, as it amplifies the effects of interactions. In order to understand how the DOS may be affected by the band structure, we can write down the expression for the density of states as

$$D(E) = \frac{2}{(2\pi)^d} \int_{S(E)} \frac{dS}{|\nabla_{\mathbf{k}} E(\mathbf{k})|}. \quad (1.13)$$

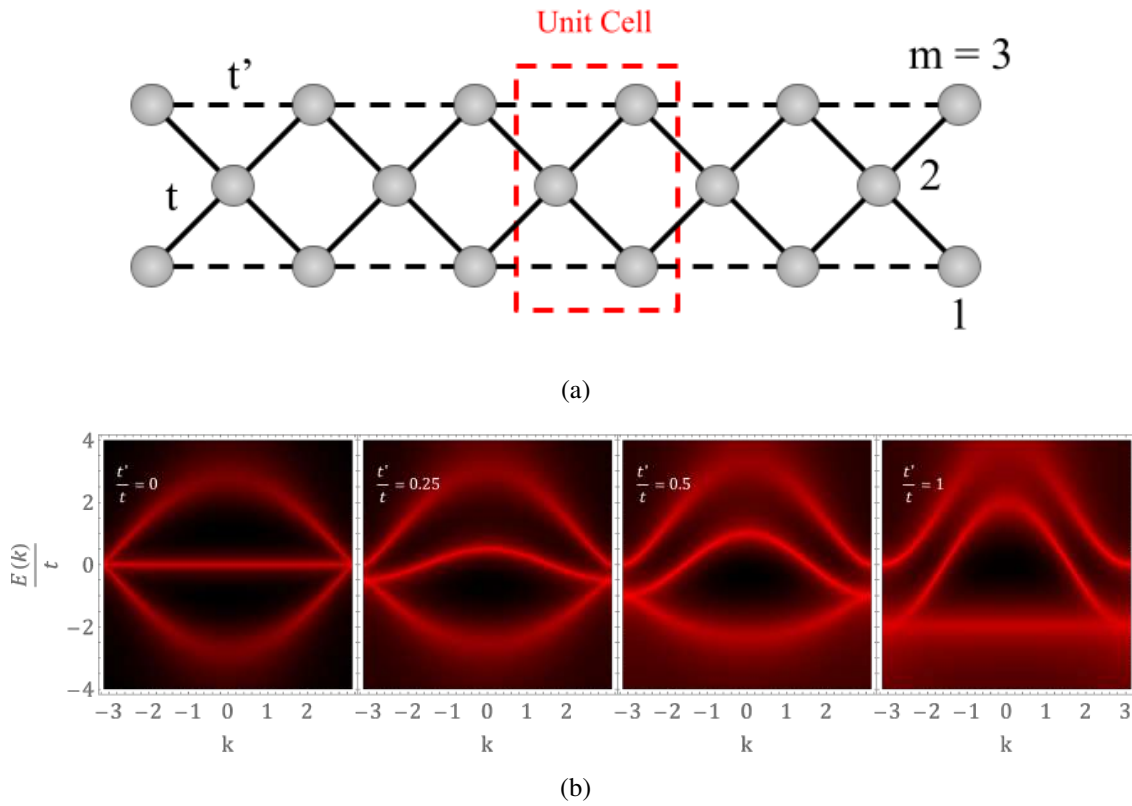


Figure 1.12: (a): Illustration of the 1D diamond chain. The two hopping parameters considered are  $t$ , between the central atom and the others, and  $t'$ , between the external atoms. (b) One dimensional diamond chain electronic structure calculated by the Tight Binding Model.

The integral in equation 1.13 is carried over of the surface of constant energy  $S(E)$ , where  $E(\mathbf{k})$  is the energy dispersion relation and  $d$  is the dimensionality of the system [43, 42]. Note, then, that the DOS will present a drastic increase when the electron velocity,  $\mathbf{v}_{\mathbf{k}}$ , becomes or gets close to zero, since the density of states is inversely proportional to the energy gradient, as long as the integral doesn't goes to zero faster than the inverse gradient diverges. That means, thus, that the regions where the band structure has a local maximum, a local minimum or a saddle point, also know as van Hove singularities, or simply has flat or quasi-flat dispersion are strong candidates for displaying high DOS.

It is important to note that such orders of correlated states emerge only at a critical temperature, when the thermal excitation introducing disorder are overcome by the interactions favoring ordering. As one may realize, the density of states, therefore, also plays an important role at defining such a critical temperature, as, for example, determined by the BCS Theory [42],  $T_c = \frac{2e\gamma_E}{\pi} \frac{\hbar\omega_D}{k_B} e^{-\frac{1}{V_0\rho_F}}$ , where  $\gamma_E \approx 0.577$  is the Euler constant,  $\omega_D$  is the Debye frequency,  $k_B$  is the Boltzmann constant,  $\hbar$  is the Planck constant,  $V_0$  is the attractive interaction term and  $\rho_F$  is the density of states at the Fermi Level.

Over the recent years, many different groups of researches have studied ways to induce flat bands and/or

---

tune them to the Fermi Level in many different systems, such as cuprates [44, 45] with their paradigmatic high temperature superconductivity, van der Waals heterostructures, mainly on thin-films and twisted layers [46, 47, 48, 49], kagomes materials [50] and many others [51].

## Chapter 2

# Instrumentation and Methodology

This chapter is dedicated to introducing the fundamental principles associated with theory and instrumentation of the Angle Resolved Photoemission Spectroscopy (ARPES) technique. Furthermore, it provides a description of the experimental setups utilized in the context of this study.

### 2.1 Photoelectron Spectroscopy

The process of photoelectron emission found its first comprehensive explanation in Einstein's work in 1905. He identified the quantum nature of light as the underlying cause of this phenomenon, which we now refer to as the photoelectric effect. In this phenomenon, when light, or more generally, radiation, impinges upon a material, a photon can be absorbed by an electron, resulting in the emission of that electron from the material. The maximum kinetic energy of the emitted photoelectron is determined by the expression  $h\nu - \phi$ , where  $\nu$  represents the photon frequency, and  $\phi$  represents the material's work function. This work function acts as a potential barrier at the material's surface, preventing the excited electrons from escaping.

In order to gain a deeper understanding of the insights provided by Angle Resolved Photoemission Spectroscopy (ARPES) results, it's important to comprehend some fundamental aspects of the theoretical framework underlying photoemission. When considering that this process takes place within a many-body system (the sample), describing the excitation of electrons becomes an exceedingly complex task. However, an insightful simplification can be achieved by adopting the "single-particle picture", where the photoemission process is described by a single-particle removal function from the initial system. This approach uses first-order perturbation theory together with *Fermi's Golden Rule* to describe the transition process.

We start this approach by examining the Hamiltonian of an electron within a solid, which incorporates a small perturbation term resulting from its interaction with the electromagnetic field of a photon:

$$\begin{aligned}
H &= \frac{1}{2m_e} \left[ \mathbf{p} - \frac{e}{c} \mathbf{A} \right]^2 + U(\mathbf{r}) \\
&= \frac{1}{2m_e} p^2 + \frac{e}{2m_e c} (\mathbf{A} \cdot \mathbf{p} + \mathbf{p} \cdot \mathbf{A}) + \frac{e^2}{2m_e c^2} A^2 + U(\mathbf{r}) \\
&= \underbrace{\frac{p^2}{2m} + U(r)}_{H_0} + \underbrace{\frac{e}{2m_e c} (\mathbf{A} \cdot \mathbf{p} + \mathbf{p} \cdot \mathbf{A}) + \frac{e^2}{2m_e c^2} A^2}_{H_{int}} \tag{2.1}
\end{aligned}$$

where  $\mathbf{A}$  is the potential vector,  $\mathbf{p} = -i\hbar\vec{\nabla}$  is the electronic momentum operator,  $H_0$  is the Hamiltonian of an electron in a periodic field and  $H_{int}$  is the perturbation term caused by the interaction with the photon.

Unless for the case of very high energies, the two-photon process term proportional to  $A^2$  is not relevant, so it will be put aside. The perturbation term can be further simplified by taking the approximation that  $\mathbf{A}$  is constant over atomic distances and thus  $\nabla \cdot \mathbf{A} = 0$ . This way, it is written as:

$$H_{int} = \frac{e}{m_e c} \mathbf{A} \cdot \mathbf{p} \tag{2.2}$$

For the purpose of having the most general approach to the phenomenon, the electron excitation, emission and detection should be described as one coherent process, which means that many different states, such as the ones arising from bulk and surface properties, should be considered in the Hamiltonian. This way of approaching the problem is rather complex and is known as the *One-Step Model*. An alternative way to proceed, the *Three-Step Model* divides the photoemission process into three parts independent of each other: the absorption of a photon by a bulk electron, the path of the excited electron to the surface and the liberation of the electron to the vacuum [52, 53, 54]. Although this is a phenomenological description, it provides a fine understanding of the fundamental characteristics of the phenomenon and is largely used to unfold photoemission experimental data.

The photoemission intensity will be described, then, by these three elements. First, the probability of the transition, which contains all the information regarding the electronic structure of the system. Second, the scattering rate of electrons moving towards the surface, phenomenologically associated to their mean free paths. Third, the probability of the electron transmission through the surface, dependent on the material's surface energy barrier, called the inner potential  $V_0$ , and on the energy of the electron's excitation.

We start by discussing the transition probability between the initial ground state and the excited final state, both with  $N$  electrons. The *Fermi's Golden Rule* states that [55]:

$$w_{if} = \frac{2\pi}{\hbar} |\langle \psi_f^N | H_{int} | \psi_i^N \rangle|^2 \delta(E_f^N - E_i^N - h\nu) \tag{2.3}$$

The first term is the matrix element from the initial,  $\psi_i^N$ , to final,  $\psi_f^N$ , state. The last term imposes the energy conservation, where the final state energy  $E_f^N$  has to be the same of the initial state energy  $E_i^N$  plus

the energy increase of the absorbed photon.

At this point, it is relevant to note that as the electron leaves the material, the system also returns to the ground state, in the relaxation process. This interplay between the emitted electron and the rest of the remaining system increases substantially the complexity of the description. It is useful to simplify the problem by making use of the *sudden approximation*. Here, the photoelectron is transmitted through the surface instantaneously, which leaves no room for interactions to modify the electronic eigenstate. This way, the final state can be represented by [54]

$$|\psi_f^N\rangle = |\phi_f^{\mathbf{k}}\rangle |\psi_f^{N-1}\rangle \quad (2.4)$$

where  $|\phi_f^{\mathbf{k}}\rangle$  is the photoelectron's state with momentum  $\mathbf{k}$  and  $|\psi_f^{N-1}\rangle$  is the final state of the N-1 remaining electrons in the material, which can be in any of the possible excited states, given by the combination  $m$  of all quantum numbers that characterize such a state [52]. Note that this final state describes the system after the electron detachment but before the relaxation, so the total transition probability is given by the sum over all possible  $m$ , so we will write the final state as  $|\psi_m^{N-1}\rangle$ .

Similarly, the initial state can be decoupled from the rest of the system by considering a description of the many body problem given by Hartree-Fock formalism, where  $|\psi_i^N\rangle$  is approximated as a single Slater determinant. Thus, it is given as the direct product of the one-electron states, which allow us to write the initial state as

$$|\psi_i^N\rangle = |\phi_i^{\mathbf{k}}\rangle |\psi_i^{N-1}\rangle \quad (2.5)$$

We can write, then, the interaction matrix element as

$$\begin{aligned} \langle \psi_f^N | H_{int} | \psi_i^N \rangle &= \sum_m \underbrace{\langle \phi_f^{\mathbf{k}} | H_{int} | \phi_i^{\mathbf{k}} \rangle}_{M_{f,i}^{\mathbf{k}}} \underbrace{\langle \psi_m^{N-1} | \psi_i^{N-1} \rangle}_{P_{m,i}} \\ &= \sum_m M_{f,i}^{\mathbf{k}} P_{m,i} \end{aligned} \quad (2.6)$$

where  $M_{f,i}^{\mathbf{k}}$  is the one-electron dipole matrix element and  $P_{m,i}$  is the N-1 electron state overlap integral. Since the total photoemission intensity is proportional to the sum of all possible states for the transition rate, we have

$$\begin{aligned}
I(k, E_k) &\propto \sum_{i,f} \omega_{if} \\
&\propto \sum_{i,f} \left| M_{f,i}^k \right|^2 \sum_m |P_{m,i}|^2 \delta(E_{kin} + E_m^{N-1} - E_i^N - h\nu)
\end{aligned} \tag{2.7}$$

The total intensity is then measured as a function of the kinetic energy,  $E_{kin}$ , at a given momentum  $k$ . Note that if the electrons do not interact with each other, their initial state  $|\psi_i^{N-1}\rangle$  should be the same as the final state  $|\psi_m^{N-1}\rangle$ , that is,  $m = i$  for a particular state, then the only non-zero overlapping integral term is  $|P_{i,i}|^2 = 1$ . So, if the one-electron transition is allowed,  $M_{f,i}^k \neq 0$ , the intensity will be given by a sharp line, a delta function, at the specific momentum  $k$ . By allowing the electron interactions to happen, there will be a range of spectral weights,  $|P_{m,i}|^2$ , associated to overlapping of the initial state with the many excited states, effectively broadening the photoemission intensity.

## 2.2 Interacting Picture - The one-particle spectral function and self energy

The last term in equation 2.7 contains the information related to the electronic structure within the material resulting of the process of the electron excitation. We can define it, then, as a separated function called the *one-particle spectral function*,

$$A(k, E) = \sum_m |P_{m,i}|^2 \delta(E + E_m^{N-1} - E_i^N - h\nu) \tag{2.8}$$

In general, the coefficients  $P_{m,i}$  are different from zero as the electrons start to interact. The most common way to approach this correlated electron system is by using the Green's function Formalism [54]. In the physical context of many body systems, the one-electron Green's function,  $\mathcal{G}(t - t')$ , describes the propagation of an electron. One can express  $\mathcal{G}(t - t')$  in terms of energy and momentum by taking it's Fourier Transform, leaving us with  $\mathcal{G}(k, E) = G^+(k, E) + G^-(k, E)$ , which are defined in terms of a creation (annihilation) operator in the N-particle initial state. By following the appropriated steps [52], it is possible to relate one-particle spectral function to the single particle Green's function by writing:

$$A(k, E_k) = -\frac{1}{\pi} \text{Im}(G(k, E_k)) \tag{2.9}$$

Having established the one-particle spectral function as in equation 2.9, it is convenient to account the electron-electron correlation effects by expressing the Green's function in terms of the electron *self-energy*  $\Sigma(k, E) = \Sigma'(k, E) + i\Sigma''(k, E)$ . This gives us:

$$G(k, E) = \frac{1}{E - \epsilon_k - \Sigma(k, E)} \quad A(k, E) = -\frac{1}{\pi} \frac{\Sigma''}{(E - \epsilon_k - \Sigma')^2 - \Sigma''^2} \tag{2.10}$$



The self energy  $\Sigma(k, E)$  contains the information related to the energy renormalization, with its real part, and to the lifetime, with its imaginary part, of an interacting electron in a many body system, having a band energy  $\epsilon_k$  and momentum  $k$ .

This result show us that the measured photo-electron's energy corresponds to its band energy plus a renormalization factor of the self energy. For a Fermi liquid, when quasiparticles exist, the self-energy components are constant and the spectral function shown in equation 2.10 becomes a Lorentzian distribution.

There is one final important effect neglected so far in the discussion of the photoemission intensity, which is the temperature influence on the system. The ARPES photoemission will only detect occupied electronic states. This can be taken into account by introducing the Fermi-Dirac distribution function  $f(E, T) = (e^{\frac{E}{k_B T}} + 1)^{-1}$ , which results in the most common expression for the ARPES intensity signal [55]:

$$I(k, E) = I_0(k, \mathbf{A})A(k, E)f(E, T) \quad (2.11)$$

where  $I_0(k, \mathbf{A}) \propto \sum_{i,f} |M_{if}^k|^2$ , which depends on the electron momentum and energy and polarization of the incoming light,  $E$  is the electron energy with respect to the Fermi Level. Finally, it is worth mentioning that equation 2.11 does not take into consideration any kind of background or experimental effects such as finite energy and momentum resolution that can cause peak broadening. Although this is a simplified description of the photoemission process, limited by the several approximation made, it provides a very insightful understanding of the ARPES spectra.

## 2.3 ARPES - General Description

The main idea of the Angle-Resolved Photoemission Spectroscopy (ARPES) technique is to collect the photoemitted electrons with an electron analyzer, an instrument that accepts electrons within a fixed angle aperture and then detects them at different positions, measuring the electron kinetic energy according to the emission angle, creating a map of the intensity of the detected electron as function of both of these parameters, for a given sample orientation. The general geometry of an ARPES experimental is presented in Figure 2.1b.

Once the measurements are performed, it is necessary to convert the kinetic energy into the binding energy and the detected angles into momentum. Let's see how each of these quantities are related, starting with the energy. The binding energy is defined as the energy necessary for an electron to reach the Fermi Level  $E_F$ , meaning that it will be a shift in the probed kinetic energy so that  $E_F$  is set to a binding energy equal to zero. This way, we can write

$$E_{kin} = h\nu - \phi - |E_B| \quad (2.12)$$

For the momentum relation with the detected angle, we have to think in terms of the momentum conservation along the parallel and perpendicular directions. The momentum of the electron outside the sample,

after the excitation process, is given by a free electron dispersion:

$$E_{kin} = \frac{\hbar^2 k_{vac}^2}{2m_e} \quad (2.13)$$

where  $k_{vac}^2 = |\mathbf{k}_{vac}|^2$  is the electron momentum in the vacuum (after it escapes the sample). We can decompose the electron momentum inside the solid into components parallel,  $\mathbf{k}_{||} = \mathbf{k}_x + \mathbf{k}_y$ , and perpendicular,  $\mathbf{k}_{\perp} = \mathbf{k}_z$ , to the surface contributions. The in-plane components, which run parallel to the surface of the sample, remain conserved. However, the out-of-plane component, which is perpendicular to the surface, is not conserved due to the discontinuity in the medium in this direction. This discontinuity disrupts translational symmetry by introducing a sudden change in the potential along the  $z$ -axis.

As a result, when dividing the electron momentum in vacuum in the same manner, we can express the following equations in terms of the polar angle ( $\vartheta$ ) and azimuthal angle ( $\varphi$ ) emission angles defined by the experimental setup:

$$\begin{aligned} \mathbf{k}_{x,vac} &= \mathbf{k}_x = \sqrt{\frac{2m_e E_{kin}}{\hbar^2}} \sin \vartheta \cos \varphi \\ \mathbf{k}_{y,vac} &= \mathbf{k}_y = \sqrt{\frac{2m_e E_{kin}}{\hbar^2}} \sin \vartheta \sin \varphi \\ \mathbf{k}_{z,vac} &= \sqrt{\frac{2m_e E_{kin}}{\hbar^2}} \cos \vartheta \end{aligned} \quad (2.14)$$

In order to determine the perpendicular component  $\mathbf{k}_{\perp}$ , we make use of a different approach, in which the assumption that the final states of the electrons are given by a nearly free-electron dispersion. Also, because of the potential change at the surface, it is necessary to consider an additional term, the inner potential  $V_0$ . This quantity accounts for the loss of energy required for the electron to cross the surface barrier of the material. Considering a propagation of a free electron across a step potential,

$$V(\mathbf{r}) = \begin{cases} -V_0, & \text{if } r_{\perp} < 0 \\ 0, & \text{if } r_{\perp} > 0 \end{cases} \quad (2.15)$$

where  $V_0$  is the inner potential of the solid, which is roughly given by the sum of work function  $\phi$  and valence band-width  $E_0$ . During the emission process, energy has to be conserved, then, we can write

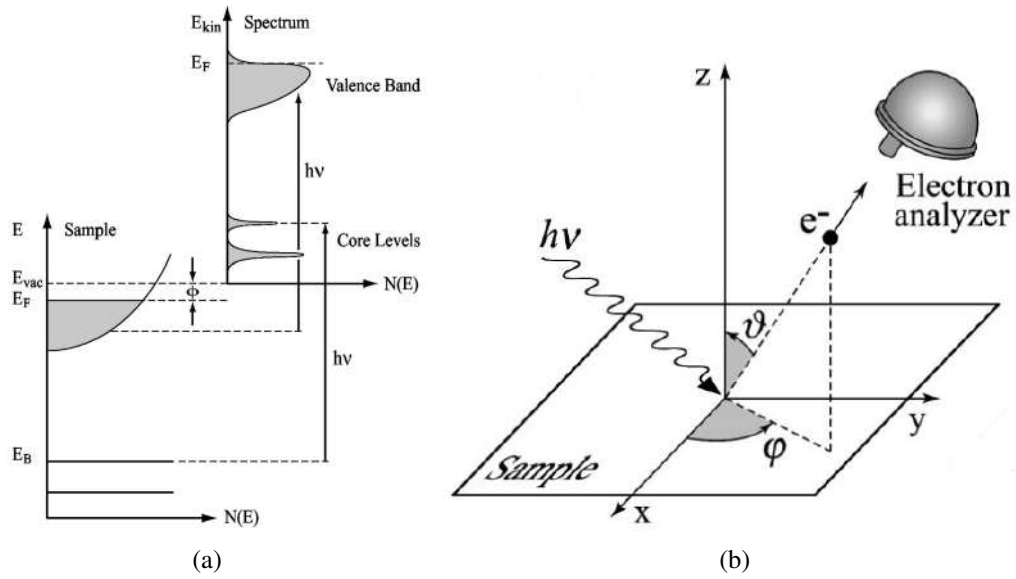


Figure 2.1: (a): An incident beam of photons causes the emission of an electron. The measurement is usually done as function of the kinetic energy  $E_{kin}$  of the photoelectron (right). It is common to relate it with the states inside the solid by expressing the energy distribution of this process in terms of the binding energy  $E_B$  (left). (b): Geometry of an ARPES experiment. The photoelectron's emission direction is described by the polar ( $\theta$ ) and azimuthal  $\varphi$  angles. Both images taken from reference [55].

$$\begin{aligned}
 \frac{\hbar^2}{2m}(\mathbf{k}_\perp^2 + \mathbf{k}_\parallel^2) &= E_{kin} + V_0 \\
 \mathbf{k}_\perp^2 &= \frac{2m_e}{\hbar^2}(E_{kin} + V_0) - \mathbf{k}_\parallel^2 \\
 \mathbf{k}_\perp^2 &= \frac{2m_e}{\hbar^2}(E_{kin} + V_0) - E_{kin} \sin^2 \vartheta \frac{2m_e}{\hbar^2} \\
 \mathbf{k}_\perp &= \sqrt{\frac{2m_e}{\hbar^2}(E_{kin} \cos^2 \vartheta + V_0)} \quad (2.16)
 \end{aligned}$$

This way, we see that, in order to characterize the complete 3D Brillouin Zone, it is necessary to explore two major experimental parameters. Probing different angles allow access to a range of values for  $k_x$  and  $k_y$ , as demonstrated in equation 2.14. Changing the incoming energy  $E_{kin}$  makes it possible to probe different  $k_\perp$ . Figure 2.2 illustrates how the rotational degrees of freedom influences on the momentum space visualization.

For the 1T-ZrTe<sub>2</sub> system, the perpendicular lattice vector is  $c = 6.6221 \text{ \AA}$ . This way we can compute the reciprocal lattice vector  $\vec{b}_3 = \frac{2\pi}{c}$  and use it to calculate the energy necessary to reach  $\Gamma$  or A points. If the ratio  $\frac{k_\perp}{b_3}$  is integer, we have an equivalent  $\Gamma$  point in the system. On the other hand, if the ratio is half integer, we have an equivalent A point. Using the known values of the physical constants, the inner potential and

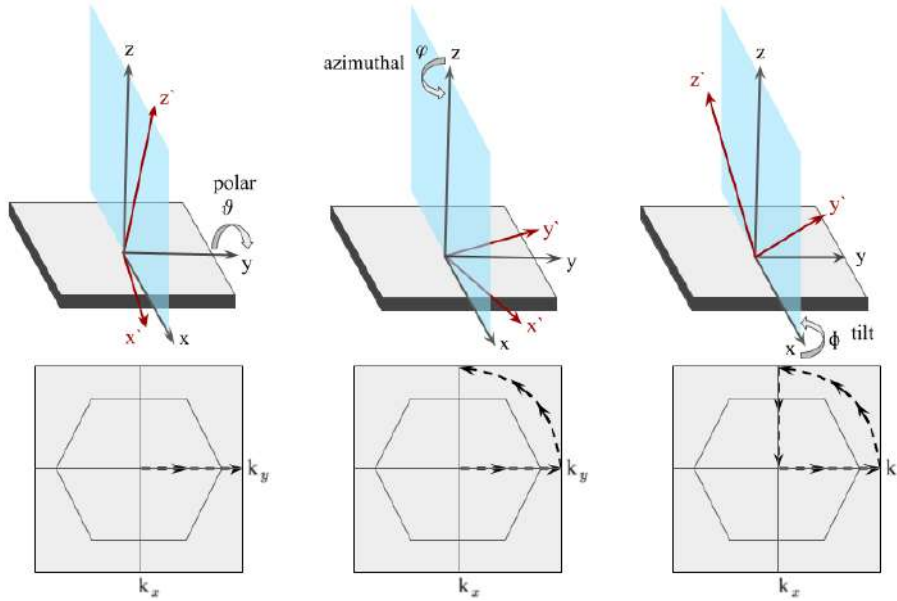


Figure 2.2: The hexagon represents the 6-fold Brillouin Zone. By rotating the polar angle  $\vartheta$  the momentum center is changed, without changing the high-symmetry direction (as indicated by the dashed arrow). Rotating the azimuthal angle  $\varphi$  changes the sample direction being probed along the slit, which changes the parallel momentum components. Rotating the tilt angle  $\Phi$  changes the  $k_y$  probed value. Adapted from [56].

work function, we find that  $E_{kin} = 88$  eV give us a ratio of approximately 5.5, while  $E_{kin} = 108$  eV, results in a ratio of 6. Those were the incident photon energies used for the majority of the measurements taken.

One more important aspect of an ARPES experiment, key to the analysis of many different phenomena, is the momentum resolution. From equation 2.14 we can see that the momentum resolution  $\Delta k_{||}$  is given by

$$\Delta k_{||} \approx \sqrt{\frac{2mE_{kin}}{\hbar^2}} \cos \vartheta \Delta \vartheta \quad (2.17)$$

where  $\Delta \vartheta$  is set by the electron analyzer's finite angle of acceptance. From this relation, we can deduce that a lower photon energy results in enhanced momentum resolution. This is the primary reason behind conducting most ARPES experiments in the ultraviolet (UV) range, where the kinetic energy,  $E_{kin}$ , is typically less than 120 eV. It's worth noting that the momentum resolution can also be improved by considering larger polar angles  $\vartheta$ . Experiments that explore regions on the edges or even beyond the boundaries of the first BZ can take advantage of this fact. Furthermore, it's important to recognize that, in the context of the TMD system under investigation in this work, the photon momentum only represents a fraction ranging from about 0.5% to 3% ( $0.01 - 0.05 \text{ \AA}^{-1}$ ) of the Brillouin size ( $2\pi/a$ , approximately  $1.593 \text{ \AA}^{-1}$ ), for photon energies between 20 and 100 eV. As such, the photon momentum can be safely disregarded when considering momentum conservation.

There is one last consideration to be made regarding the work function probed in an ARPES measurement. So far, we have been attained to the idea that  $\phi$  represents the work function of the sample, as in

equation 2.12. Even though this is true in the context of the development previously done, when performing the experiment, the Fermi energy  $E_F$  will not be given by the material's work function  $\phi$ , but rather by the work function  $\phi_A$  of the photoelectron analyzer that is connected to the sample. Because of that, for a fixed photon energy, the Fermi Level of different materials measured in the same experimental setup will be the same [57].

Transition Metal Dichalcogenides belong to a class of materials usually considered as two-dimensional. This characteristic implies that their electronic structure is typically anticipated to exhibit only small variations in response to changes in the  $k_z$ . As elaborated in section 3.3.1, for the case of  $ZrTe_2$ , the dispersion in  $k_z$  is reasonably relevant and, thus, necessary to be characterized.

## 2.4 Light Polarization Effects

The transition matrix element  $M_{f,i}^k = \langle \phi_f^k | H_{int} | \phi_i^k \rangle$ , as defined in equation 2.6, plays a crucial role in modulating the photoemission intensity. In order to understand how this term influences the final result, we have to consider the parities involved in the integral calculation, which will be zero if the final integrand is odd in respect to the mirror plane defined by the incoming light and sample normal direction. In this case, no ARPES signal would be detected. Then, if we want to extract information about the wave function of the initial state  $|\phi_i^k\rangle$ , an even function is required to probe the electronic band structure.

We start by assigning the parity of the perturbation term  $H_{int} = \frac{e}{m_e c} \mathbf{A} \cdot \mathbf{p}$ . The incident light can be polarized with many different ways, but let's suppose for the moment that the light is linearly polarized, such that the polarization vector  $\vec{\epsilon}$  can be written as

$$\vec{\epsilon} = \epsilon \begin{pmatrix} \cos \xi \\ \cos \alpha \sin \xi \\ \sin \alpha \sin \xi \end{pmatrix} \quad (2.18)$$

where  $\alpha$  is the angle in between incoming X-ray beam and electron analyzer,  $\xi$  is the orientation of the polarization vector with respect to the mirror plane. Then, for  $\xi = 0$  the polarization vector is perpendicular to the scattering plane, denominated as  $\sigma$ -polarized light, and it is odd with respect to the mirror plane. When  $\xi = \frac{\pi}{2}$  and the polarization vector is in the scattering plane, we call it  $\pi$ -polarized light, even with respect to the mirror plane. Here, we only take into consideration the parity with respect to the mirror plane because the momentum  $\mathbf{p}$  can be transformed into the position  $\mathbf{r}$  through  $[\hat{x}_i, \hat{p}_j] = i\hbar\delta_{ij}$ . Figure 2.3 illustrates the geometry of the light polarization elements.

Considering that the nearly free electron final  $|\phi_f^k\rangle$  state can be assumed as a plane wave, which is even, now the initial state parity will define the final photoemission intensity. In order to paint a simple picture, we can think the initial state as basically related to the orbital nature the electron occupies. Since for the system of  $ZrTe_2$  the  $p$  orbitals from the Te play a very important role in the composing of the electronic structure around the Fermi Level, let us use them as an example to illustrate this property. By positioning the sample

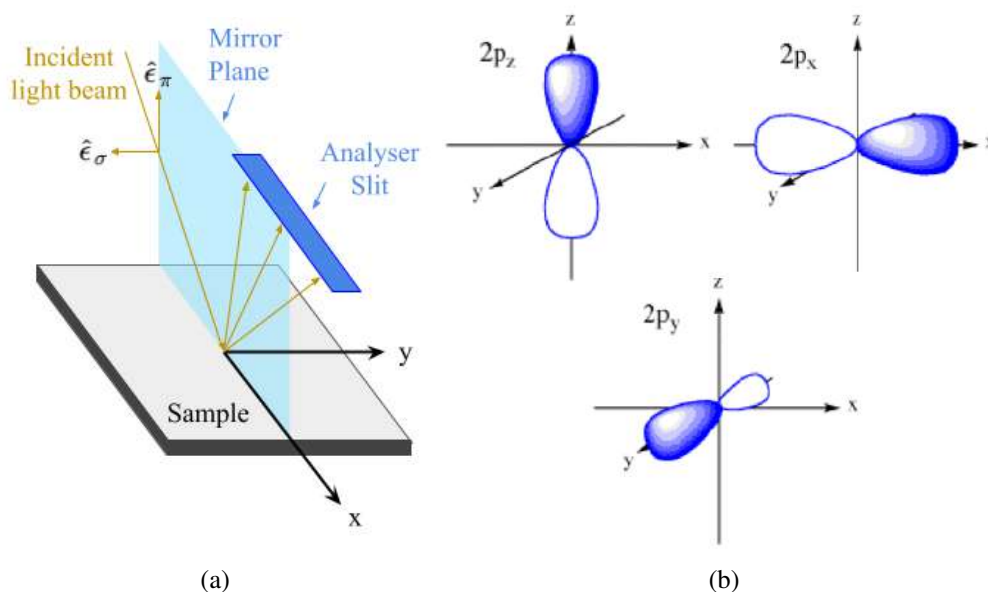


Figure 2.3: (a): The geometry of the mirror plane and both  $\sigma$  and  $\pi$  light polarization. (b): A representation of the p orbitals, which are relevant to the electronic structure of the TMD 1T-ZrTe<sub>2</sub>. The light and dark blue areas represent different phases for the orbital wave function. Image from [58].

with its  $x$  axis along the mirror plane, the  $p_y$  orbital will be odd with respect to the plane, while the  $p_x$  and  $p_z$  will be even. For simplicity, also consider that the orbitals are all aligned with the sample's orientation (which is not true in general). This way, we should expect that the  $p_x$  and  $p_z$  orbitals would only be detected with  $\pi$  light polarization and the  $p_y$  orbital, by the  $\sigma$  light polarization. Indeed, some bands do present a very strong light polarization dependence as it will be discussed in section 3.3.1.

## Chapter 3

# ARPES Data and Analysis

In the present chapter, we delve into the results obtained from our ARPES experiments conducted on several distinct systems: the parent compound  $\text{ZrTe}_2$ , as well as two doped variants, namely  $\text{Ni}_{0.05}\text{ZrTe}_2$  and  $\text{Dy}_x\text{ZrTe}_2$  (with  $x$  values of 0.01 and 0.05). Our discussion will encompass the electronic structure as measured for each of these systems, highlighting the distinctive features that characterize these compounds within the context of a CDW phase transition and the FS Nesting phenomenon.

### 3.1 Experimental Data Processing

Two series of ARPES experiments were conducted in the course of this study. Initially, a preliminary measurement was undertaken at the laboratory coordinated by Professor Dr. Claude Monney, situated at the University of Fribourg in Switzerland. This facility was equipped with a gas discharge He-lamp setup, deploying an incident photon energy of 21.2 eV, effectively targeting a region proximate to the  $\Gamma$  point of the system. Then, a second ARPES experiment was performed at the Bloch beamline in the MAX IV synchrotron facility at Lund, Sweden. For this case, a range of incident photon energies from 108 to 27 eV were used. The objective was to obtain a wider view of the electronic structure, taking advantage of the high photon flux to also probe the distinct feature observed at the previous preliminary experiment. Both the He-lamp and synchrotron ARPES were measured with the same type of electron analyzer, which was the DA30 manufactured by Scienta Omicron.

In both experiments, all aspects of data processing and treatment were done using the software IGOR Pro by Wavemetrics, Inc. USA. Within the program, ARPES data is handled as either a 3D or 2D wave. For energy mapping, the files can be thought as matrices, where one dimension encodes information regarding the tilt angle  $\phi$ , subsequently converted into  $k_x$  and  $k_y$  according to equation 2.14. The other dimension corresponds to the kinetic energy of the detected electrons. An intensity value is assigned to these two coordinates, generating the energy map. In the context of Fermi Surface measurement, the file assumes the form of a 3D "matrix" with the coordinates now associated with  $\vartheta$ ,  $\varphi$ , and kinetic energy. The program also

accommodates user coding using its own programming language, affording customizable data processing capabilities. All procedures employed in this study were developed and documented by Pakuszewski, K. R. [59], and Cantarino, M. R. [60].

In practice, it is often necessary to rectify angles by adjusting the axes of matrices, ensuring that  $k_x = 0$  and  $k_y = 0$  align with the center of the hole pockets at  $\Gamma/A$ . This adjustment compensates for potential misalignments associated with angle calibrations or translations applied to ensure that both  $\Gamma$  and  $M$  points are incorporated into the same map. Subsequently, the angles are converted into momentum units based on the relations defined in equation 2.14. This transformation yields a new axis represented in units of  $\text{\AA}^{-1}$ . Finally, the last step in data processing entails the determination and alignment of the Fermi Level for each map. This is accomplished by extracting an Energy Distribution Curve (EDC) at a specific  $k$ -point, preferably focusing on a band that intersects the Fermi Level, such as the electron pocket. Subsequently, a Fermi-Dirac distribution curve is fitted to this EDC. By identifying the energy corresponding to the Fermi Level, it becomes possible to adjust the kinetic energy, effectively establishing the binding energy for that particular map.

## 3.2 Preliminary Measurements - He-discharge lamp

Motivated by the specific heat and resistivity measurements performed by [7], which indicated a possible CDW phase transition at around  $T_c \approx 287K$  at the  $\text{Ni}_{0.05}\text{ZrTe}_2$  system, our group performed a preliminary ARPES investigation at the University of Fribourg, at the laboratory coordinated by Professor Dr. Claude Monney. This experiment was performed by Marli R. Cantarino, a former Ph.D student of our group and Christopher W. Nicholson, a former Post Doc Researcher of Monney's research group.

The experimental setup used was an He-discharge lamp, which provided 21.2 eV of incident photon energy, without any polarization. This corresponds to roughly the  $\Gamma$  point of the Brillouin Zone. A good momentum resolution of approximately  $0.01 \text{\AA}^{-1}$  and an energy resolution of 5 meV was achieved, while maintaining the pressure below  $6.3 \times 10^{-8}$  mbar. Data acquisition was performed across a temperature range spanning from 290 K down to 60 K, in order to probe the potential CDW phase transition, which had been observed around 287 K. All samples were cleaved *in situ* with scotch tape during this set of experiments, with a focus on probing the  $\Gamma$ -M high symmetry direction. This way, a comprehensive exploration of both parent and Ni-doped compound's electronic properties could be realized.

The resolved electronic structure of  $\text{ZrTe}_2$  is shown in the Energy Distribution Map (EDM) featured in Figure 3.1. We can see very distinctively two bands, denoted as  $\alpha_1$  and  $\alpha_2$ , crossing the Fermi Level in the vicinity of the  $\Gamma$  point. Additionally, there is a third hole-like band,  $\alpha_3$ , residing at a deeper binding energy. Around the  $M$  point, we discern the presence of a single electron-like dispersion,  $\beta$ , intersecting the Fermi Level. This characteristic band structure aligns very well with the attributes of a semimetal, as expected. Figure 3.1 shows these bands drawn over the EDM for a more clarifying view.

To discern any alterations in the electronic structure induced by a CDW order within the material, a



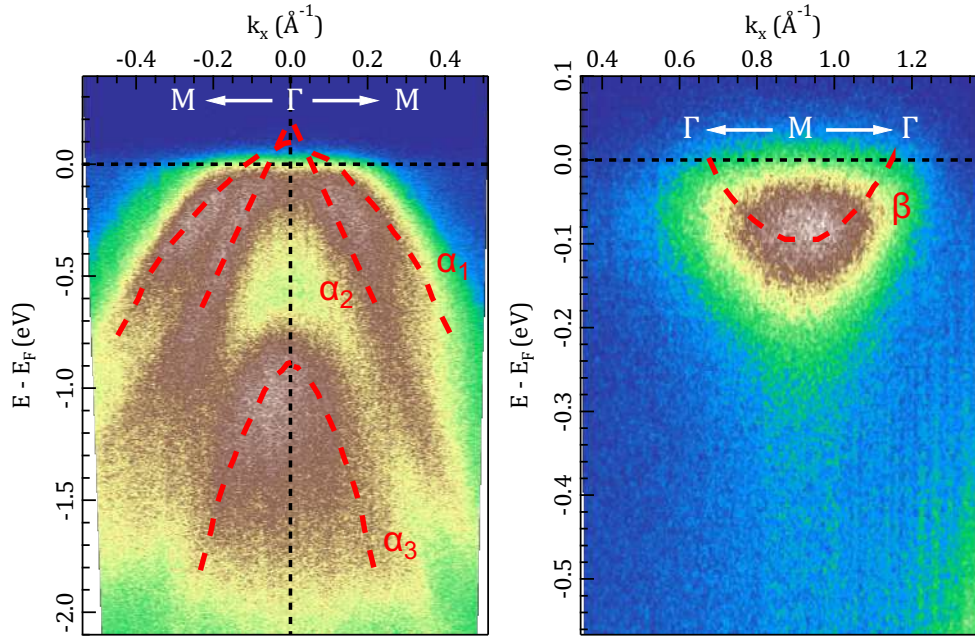


Figure 3.1: Left side: Energy Distribution Maps (EDMs) centered at the  $\Gamma$  point for the parent compound, at 21.2 eV photon energy. Right Side: Same as the left side, but centered at the M point. The red dashed lines represent the bands in the vicinity of the Fermi Level (not fittings). Both measurements taken at  $T = 290$  K.

series of EDMs were acquired across different temperatures for both samples. Figure 3.2 presents the series of EDMs obtained through these measurements. Typically, subtle changes are challenging to detect solely through EDMs. Therefore, it is customary to examine the Energy Distribution Curves (EDCs), depicted on the right-hand side of Figure 3.2, as these offer a means to scrutinize specific momentum points more closely. Specifically, EDCs for the  $\Gamma$  and M points were extracted at various temperatures for both samples.

Upon analyzing the EDCs at the  $\Gamma$  point, we observe an absence of discernible changes when transitioning from temperatures above to below  $T_c$ . However, a pronounced gain in spectral weight becomes apparent at approximately  $E_B \approx -0.7$  eV for the Ni-doped sample, a feature which is absent in the parent compound. This intriguing observation is indicated by the black arrow in the plot.

In initial assessments, this feature was tentatively attributed to a potential band folding phenomenon of the electronic structure, stemming from the CDW order present in the Ni-doped material. This observation fueled further investigation of this compound, compelling us to undertake a second study using a synchrotron light facility to gain a more comprehensive understanding of this alteration.

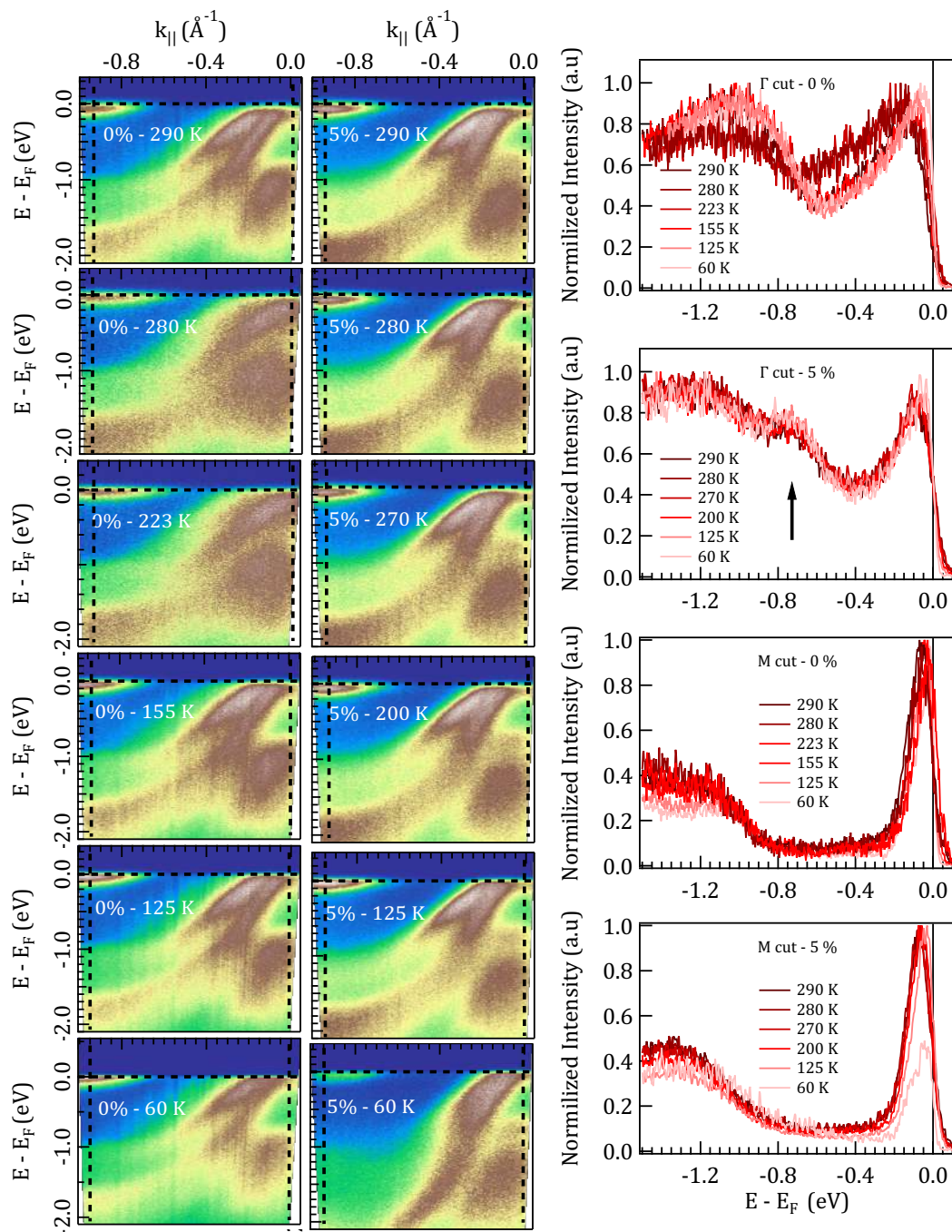


Figure 3.2: Left side: Energy Distribution Maps (EDMs) along the the  $\Gamma$ M high symmetry direction for 21.2 eV photon energy for the parent compound and the 5% Ni doped sample, for a range of temperatures. The dashed lines mark the EDCs cuts. Right Side: Energy Distribution Curves along the fixed momentum points  $\Gamma$  and M of the respective EDMs. The black arrow indicated the appearance of an spectral signal for the 5% doped sample at all temperatures.

### 3.3 Synchrotron Light Measurements

Building upon the insights gained from the preliminary measurement, a subsequent ARPES experiment was conducted at the Bloch beamline, situated within the MAX IV synchrotron facility in Lund, Sweden. This follow-up experiment was designed with the aim of obtaining a more expansive and comprehensive view of the electronic structure. Taking advantage of the high photon flux available at this facility, we could not only explore the broader electronic landscape but also to further investigate the distinct feature previously observed during the initial experiment (as detailed in section 3.2).

During this phase of the study, the photon energy range was initially spanned from 88 eV to 108 eV, corresponding to the  $A$  and  $\Gamma$  points. The temperature was maintained at 20 K, except in cases involving the Ni-doped sample, where temperatures of 100 K and 284 to 288 K were also explored. Our measurements encompassed both the  $\Gamma$ -M(A-L) and  $\Gamma$ -K(A-H) high symmetry directions, affording us a more comprehensive perspective. As in the previous experiment, the samples were subjected to cleavage *in situ* using Scotch tape. Additionally, the experimental setup accommodated both linear parallel- $\pi$  and perpendicular- $\sigma$  incident light polarizations, allowing us to explore a broader range of electronic characteristics.

This time around, we attained a momentum and resolution ranging between 0.01-0.02  $\text{\AA}^{-1}$  and 5-10 meV, respectively. Furthermore, an ultra-low pressure environment was adopted, ensuring that the pressure level remained below  $2 \times 10^{-11}$  Torr throughout the course of the experiment.

#### 3.3.1 The Parent Compound

The resulting band structure for the parent compound,  $\text{ZrTe}_2$ , is shown in Figure 3.3. As indicated by the guiding lines, it is possible to see very prominently the bands around the  $\Gamma$  point, where we identify two holelike bands that cross the Fermi Level,  $\alpha_1$  and  $\alpha_2$ . Furthermore, deeper within the electronic structure, two additional hole-like bands,  $\alpha_3$  and  $\alpha_4$ , emerge at approximately  $E_B = -0.3$  eV and  $E_B = -1$  eV, respectively. These two bands feature a strong dependence on the incident light polarization,  $\sigma$ -pol for the  $\alpha_3$  and  $\pi$ -pol for the  $\alpha_4$ . Beyond that, we can also see the electron-like band dispersion close to the Fermi Level around the M point, labeled  $\beta$ .

It is also possible to characterize the subtle difference between the electronic structure at ALH (88 eV) and  $\Gamma$ MK (108 eV) planes. As we can see in the EDCs presented on Figure 3.3, the first noticeable change is a small shift, approximately 0.1 eV toward the Fermi Level, observed in the  $\alpha_3$  band when comparing  $\Gamma$  to A. Other difference resides at the polarization dependency of this same band, which is more pronounced at A when compared to  $\Gamma$ , showcasing a higher spectral signature under  $\pi$ -polarization, although it still remains strongly influenced by  $\sigma$ -polarization. This divergence hints at varying orbital compositions along the  $z$ -axis.

As suggested by the authors in Ref [12], the 1T- $\text{ZrTe}_2$  system exhibits the potential for a linear band dispersion. Indeed, our investigation has revealed the presence of a parabolic band, denoted as  $\alpha_1$ , and a steeply linear-dispersing band, designated as  $\alpha_2$ . The latter creates a Dirac cone-like structure around the  $\Gamma$  point, crossing the Fermi Level. In order to better study this feature, we employed a standard Momentum

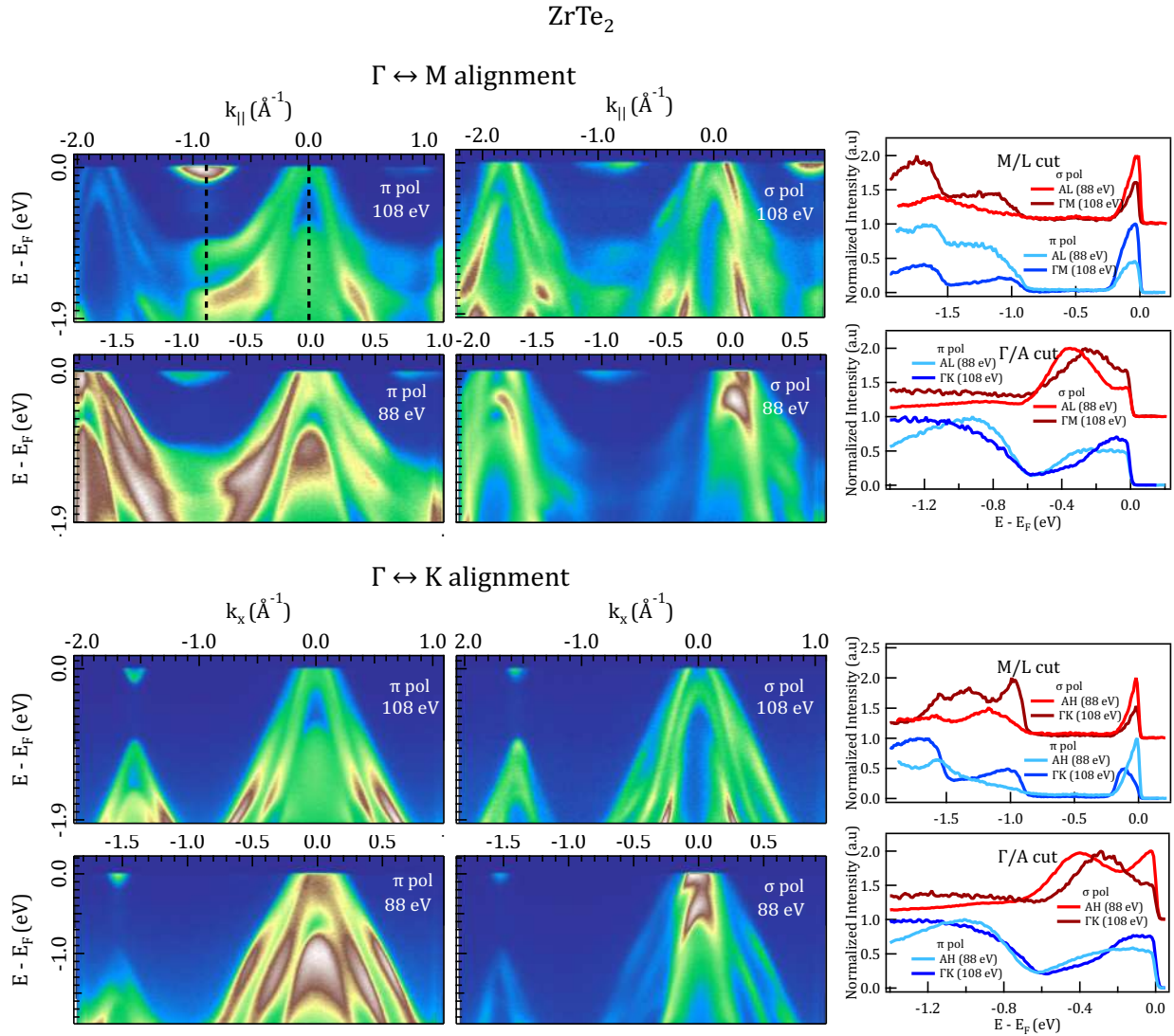


Figure 3.3: Left side: Energy Distribution Maps (EDMs) along the the  $\Gamma K$  high symmetry direction, at both  $\pi$  and  $\sigma$  light polarization for the  $\Gamma K M$  and ALH BZ plane, respectively for 108 eV and 88 eV photon energy. All measurements were taken at 20 K. The dashed lines in the upper most EDM indicates the momentum points for the EDCs presented ( $\Gamma$  and M points). Right Side: EDCs taken at the high symmetry points.

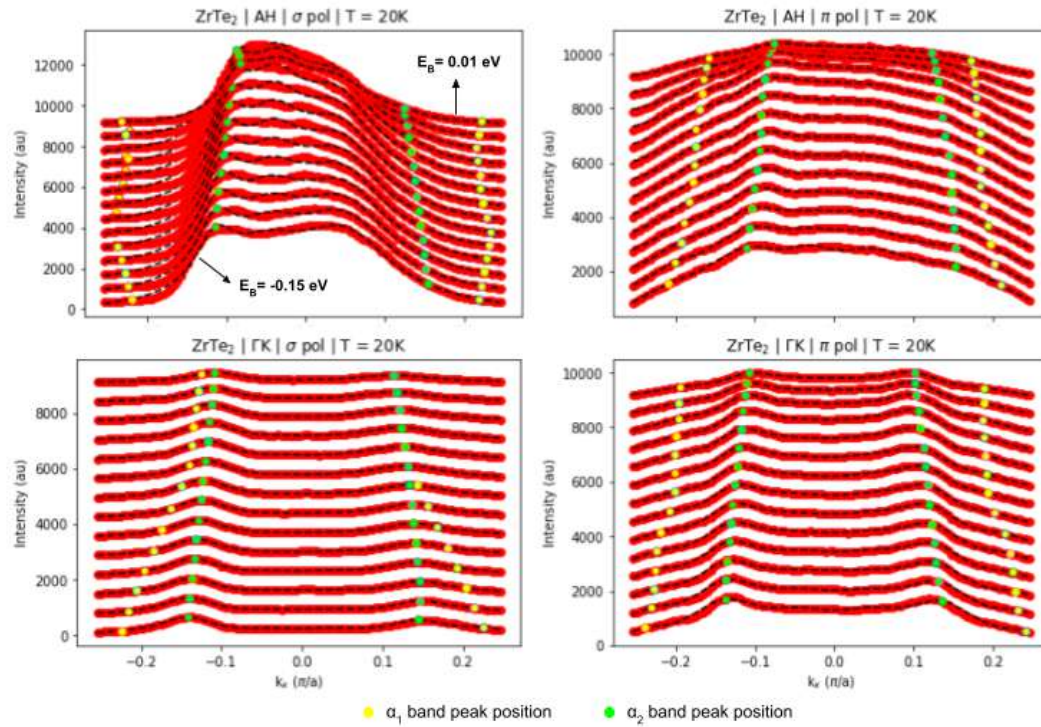


Figure 3.4: ARPES MDC analysis. Fittings (dashed black lines) of several MDCs (red lines) for increasing binding energies. Data for both light polarization and incident photon energy (88 eV and 108 eV), measured along  $\Gamma K$  at  $T = 20$  K for the parent compound, with triple band fitting (six Lorentzian peaks per profile) for a  $k$  range of  $-0.25$  to  $0.25 \text{ \AA}^{-1}$ . Only the bands  $\alpha_1$ , in yellow, and  $\alpha_2$ , in green, are highlighted.

Distribution Curve (MDC) evaluation of the band structure [61].

This method focuses on sections corresponding to a constant energy, effectively scanning how the spectral weight changes as momentum varies. By assuming that the dispersion can be linearized, MDC profiles can be modeled using Lorentzian functions. Employing Lorentzian fits to the MDCs allows us to deduce the dispersion relation by identifying the maxima of the Lorentzian peaks. The results of this analysis are presented in Figure 3.4, which showcases the MDC evaluation for both valence bands in the vicinity of the Fermi Level.

By utilizing the relation  $E = \hbar v_F k$ , we were able to estimate the Fermi velocity for the  $\alpha_2$  band. At the  $\Gamma MK$  plane, the Fermi velocity was determined to be  $v_F^\Gamma \approx 6.27(37) \times 10^5$  m/s and at the ALH plane, it was found to be around  $v_F^A \approx 6.63(23) \times 10^5$  m/s. These values were obtained as the averages of the linear segments (two for each map) for each light polarization (resulting in a total of four velocities to be averaged). Both values are consistent with the previous findings [12] and represent approximately 60% of the Fermi velocity of graphene.

Turning our attention to the Fermi Surface maps, the panel in Figure 3.5 shows the obtained results. These images portray the combined dispersion of  $k_{\parallel} \times E_B$ , with a specific focus on the cut for  $E_B = 0$ . These maps unequivocally unveil the hexagonal symmetry inherent to the system, a characteristic further reinforced by the overlay of the two-dimensional Brillouin Zone (BZ) drawn on top of the maps. Here, the electron pockets occupy positions near the M point, while the hole pockets, around  $\Gamma$ . Interestingly, the electron pocket exhibits a distinctive three-fold symmetry in its intensity, which makes the K and K' nonequivalent points.

Another type of measurement is the  $k_z$  dispersion, which is done by gradually changing the photon energy. This approach allow us access to distinct perpendicular momenta, as outlined by equation 2.16. Figure 3.6a shows the  $\Gamma$ MLA mapping for both light polarization with photon energies ranging from 85 to 110 eV in step of 1 eV, at the  $E_B = 0$ . We can see that both electron and gamma pockets have a smooth dispersion along the  $\Gamma$  to A direction. We could estimate the Fermi vectors associated to the hole pocket at  $\Gamma$  point formed by the  $\alpha_1$  band,  $k_F^{\alpha_1} \approx 0.14(2) \text{ \AA}^{-1}$ , and by the  $\alpha_2$  band,  $k_F^{\alpha_2} \approx 0.10(2) \text{ \AA}^{-1}$ , as well as for the A point, where  $k_F^{\alpha_1} \approx 0.15(2) \text{ \AA}^{-1}$  and  $k_F^{\alpha_2} \approx 0.07(2) \text{ \AA}^{-1}$ . Similar trends can be seen for the electron pocket  $\beta$  at M/L point. The estimated Fermi vector is  $k_F^{\beta} \approx 0.08(2) \text{ \AA}^{-1}$  for the  $\Gamma$  point and  $k_F^{\beta} \approx 0.12(2) \text{ \AA}^{-1}$  for the A point.

The EDMs for both high symmetry planes corroborate this significant dispersion of pockets along the  $\Gamma$ -A direction, as demonstrated in Figure 3.6b. As we can see, the deeper bands also have a relevant  $k_z$  dispersion. From these mappings, a noteworthy observation must be made which highlights a very important behaviour of the system. The spectral weight of the bands do not vanished beyond the Fermi Level, as one would expect, around the 108 eV ( $\Gamma$  point). This unexpected phenomenon posed a challenge and led to the invalidation of some measurements. This behavior has been attributed to the disparity in conductivity between the in-plane (a and b-axis) and the perpendicular direction (z-axis). The latter registers a substantially lower conductivity, implying that as electrons are photon-emitted from the sample, the bulk electrons are unable to fully compensate for the deficient surface electrons, thus giving rise to this anomalous observation.

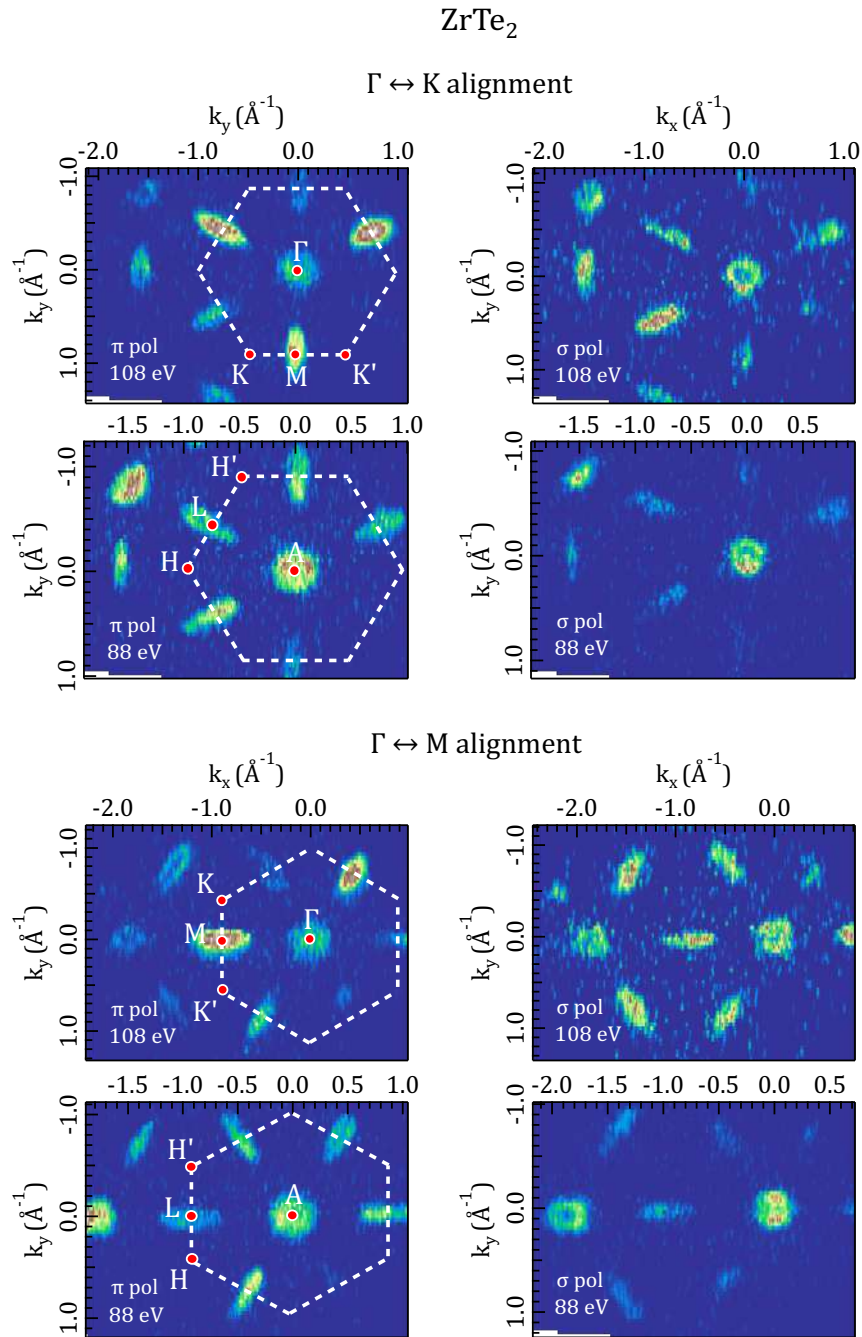


Figure 3.5: ARPES measurements of ZrTe<sub>2</sub> Fermi Maps for both high symmetry direction at both linear light polarization. The dashed white hexagon is the 2D-BZ, with the high symmetry points marked in red. All the Fermi Maps shown were measured at T = 20 K.

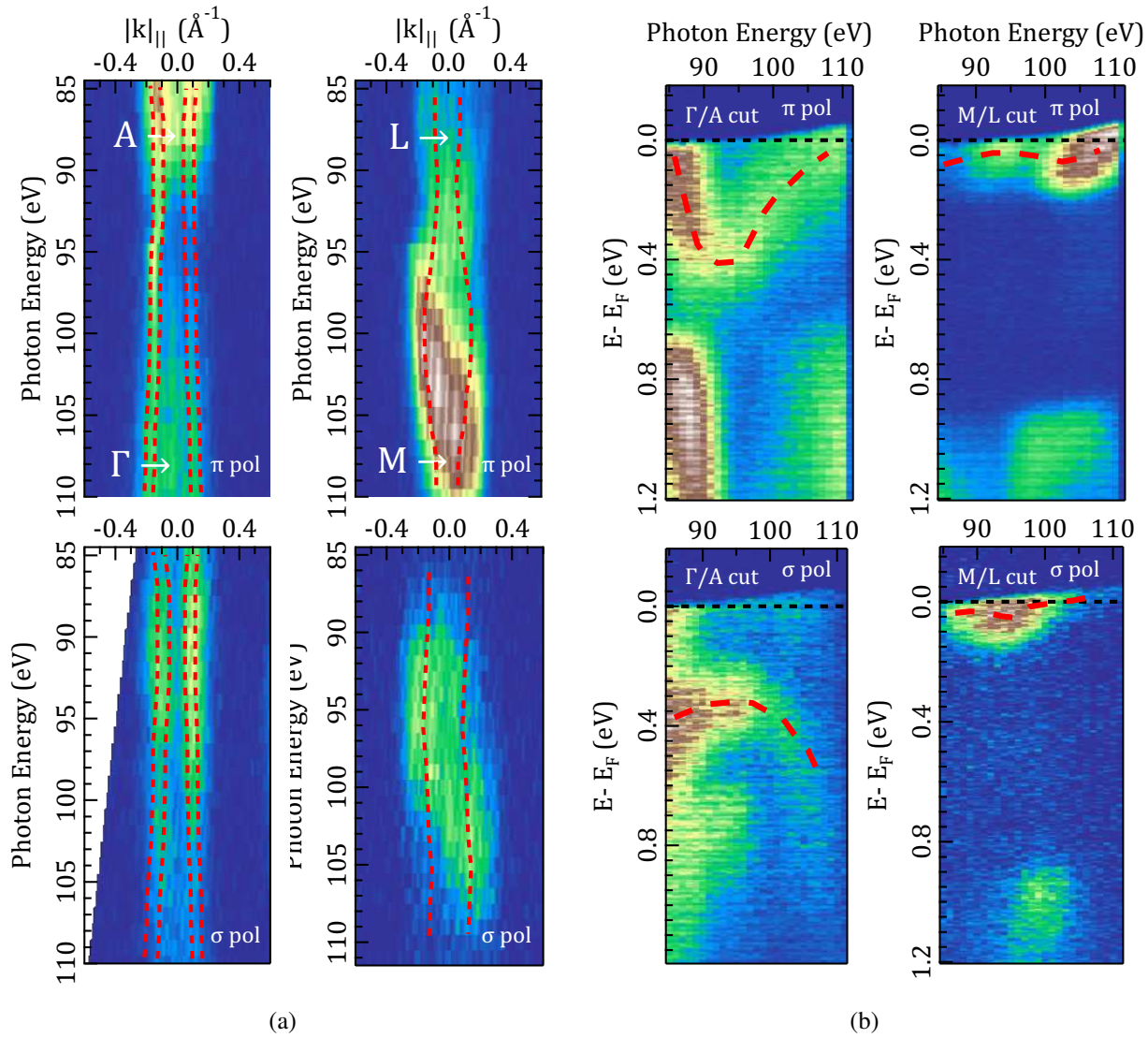


Figure 3.6:  $k_z$  dispersion of  $\text{ZrTe}_2$  for both polarization. (a):  $k_z$  dispersion along the  $\Gamma$ -A and M-L points at the Fermi Level. The dashed red lines are simply guidelines showing the crossing points of the bands. (b): EDMs for the dispersion along the  $\Gamma$ -A and M-L directions. Again, the dashed red lines are guiding the visualization of the dispersion.

### 3.3.2 The Ni-doped Sample

Next, our attention turned to the Ni-doped sample. The basic features of the band structure are preserved, as the same bands around  $\Gamma$ /A and M/L are seen. Nevertheless, there are subtle alterations on the spectral weights, associated with a new hybridization of the orbital states. The most significant deviations in the doped system reside on the introduction of two flat bands, composed of Ni-d states, positioned at binding energies of  $E_B \approx -1.2$  eV and  $E_B \approx -0.7$  eV. These newly introduced flat bands exhibit a very high



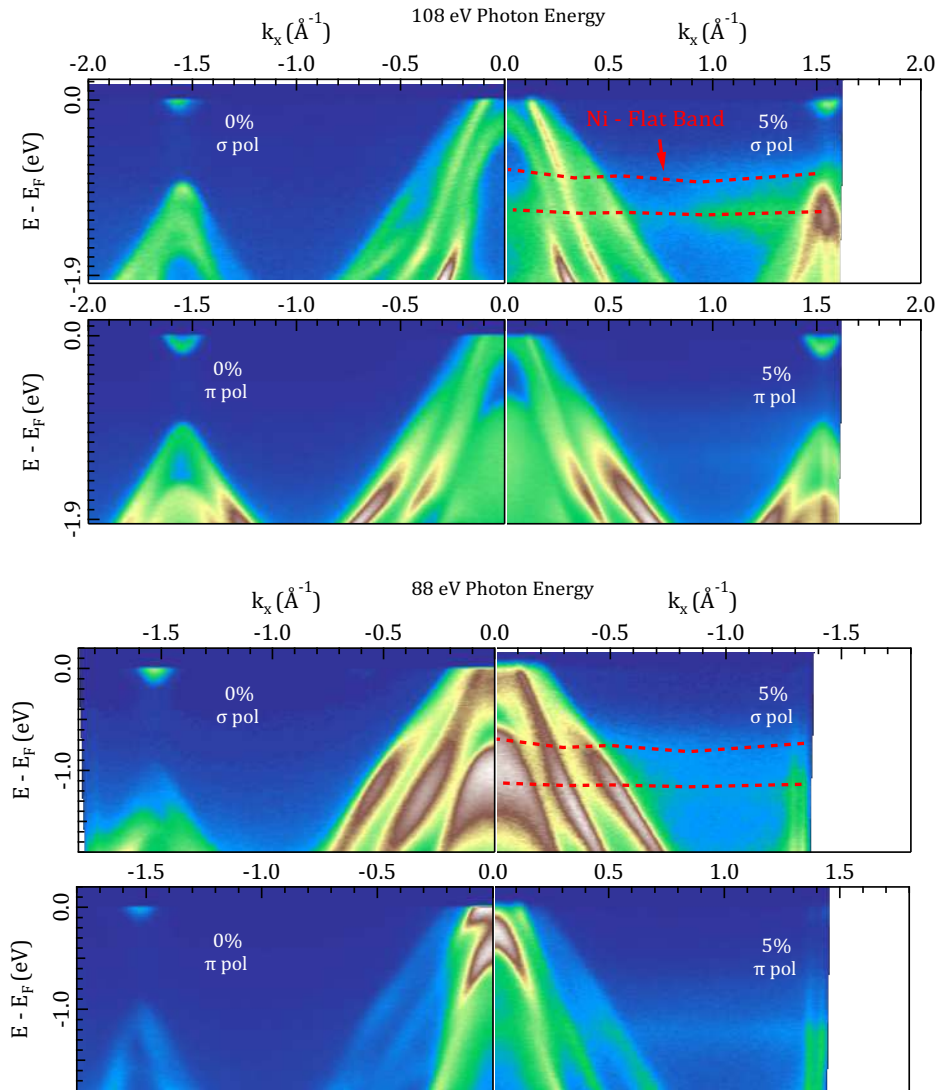


Figure 3.7: Comparison of the ARPES spectra from the parent compound (left) and the  $\text{Ni}_{0.05}\text{ZrTe}_2$  (right) for the  $\Gamma\text{K}$  high symmetry direction in both photon energy and linear light polarization. The Ni-doping features the emergence of a flat band throughout the entire reciprocal. All energy maps shown were measured at  $T = 20$  K.

sensitivity to both light polarization and sample orientation. Furthermore, there is an apparent shift of the electronic structure of approximately 100 meV towards the Fermi Level following the introduction of doping into the system. In the subsequent discussion, we delve into these findings in more details.

Figure 3.7 shows the parent compound and Ni-doped EDMs side by side for comparison. The first noticeable difference is in the emergence of a new spectral weight across the entire energy map. This new states, introduced by Ni-d orbitals from the doping, form two flat bands around the binding energies of -0.7

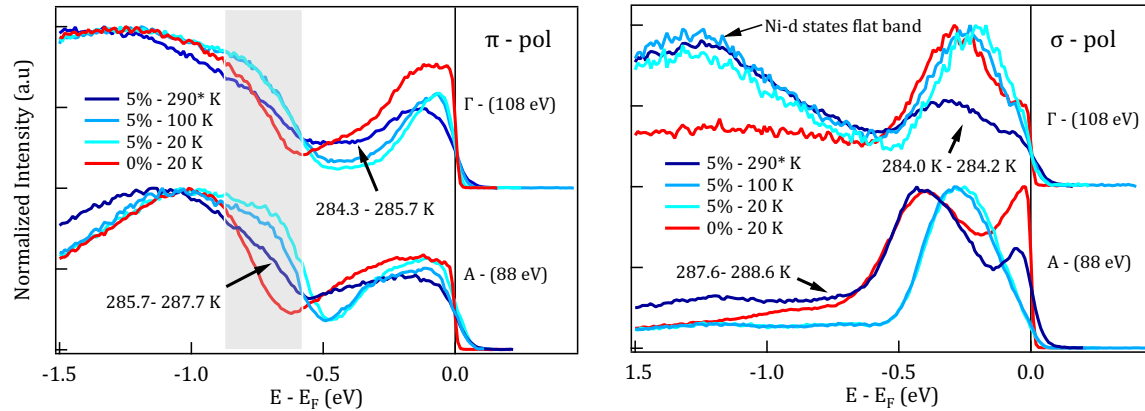


Figure 3.8: Energy Distribution Curves as function of temperature for the Ni-doped compound at  $k_x = 0$  in both BZ planes. The star mark at 290 K indicates that the temperature was not constant throughout the measurement due to an issue with the cryostat. The "kinks" discussed in the text are within the shadow region.

eV and -1.2 eV. These new states have a very strong dependence on the incoming photon polarization and reciprocal space momentum. The states are better probed when  $\sigma$ -pol photons are incident on the sample, although a vanishing spectral weight can also be seen for  $\pi$ -pol photons. Most of the spectral weight of these bands are concentrated around the edges of the BZ. Then, around half the way to the center it starts to vanish and finally close to the BZ center, it reappears with high intensity. Figure A.2 also shows the complete set energy maps that features the flat band states.

Other feature observed is the shift up (towards the Fermi Level) of the electronic band structure, mostly at the ALH plane, by the  $\alpha_3$  and  $\alpha_4$  bands, upon lowering the temperature. As it can be seen in Figure 3.8, for the  $\sigma$ -pol/88 eV (lower right EDCs), the shift is around 100 meV and is present only for the low temperature measurements ( $T = 20$  and 100 K). The high temperature EDC (dark blue) is very similar to the parent compound (red), aside from the loss of spectral weight in the vicinity of the Fermi Level. For the other cases, it was not possible to compare the high temperature doped system to the parent compound due to a technical issue. A mal-function cryostat caused the temperature to be smoothly varying during the measurements ( $\Delta T \approx 2$  K during measurements). Because of that, most high temperature measurements actually happened below the transition temperature.

On top of that, upon lowering the temperature below the transition temperature of  $T_c \approx 287$  K, the system would present a very atypical behavior. The Fermi Level became move over time, i.e., was not constant anymore. As it is not possible to perform an ARPES experiment with a shifting Fermi Level, we, thus, waited for the sample to "stabilize", which would happen only after several minutes. Even so, this erratic behavior would persist with a smaller intensity. Although we are not sure why it happened, we suspect that the conductivity in the c-axis changes past  $T_c$  such that the flow of electrons in this direction

is impaired. Because of that, the EDCs for  $T = 20$  and  $100$  K have a slight displacement compared to each other. This is an artificial shift created by the movement of the Fermi Level throughout the measurement.

Nevertheless, it is worth noting that, independently from the technical issue and the sample behavior at low temperature, the shift of the bands were much less pronounced at the  $\Gamma$ MK plane ( $108$  eV), only on the order of  $20$  meV. The fact that the shift seems to be  $k_z$  dependent can also be associated to the exquisite behavior of the material discussed above, as it might be related to the  $c$ -axis as well.

The band shift is also accompanied by a "kink" in the EDCs which is very similar to the one observed in the preliminary experiment (indicated by the black arrow in Figure 3.2). From that experiment, we can establish that the "kink" appears with the doping, not upon lowering the temperature, although decreasing temperature sharpens the feature. We note that the EDCs from Figure 3.8 for the temperatures of  $100$  K and  $20$  K are very similar, which indicates that the electronic structure is temperature independent in this range. However, the results obtained at room temperature are slightly different from the ones at low temperatures.

For the temperature just above the transition temperature ( $T = 290^*$  K,  $\sigma$ -pol/ALH plane), it is much similar to the parent compound. For the measurement through the transition ( $T = 290^*$  K,  $\pi$ -pol/ALH plane), the EDC is almost a combination between the low temperature and parent compound. Finally, the one below  $T_c$  ( $T = 290^*$  K,  $\pi$ -pol/ALH plane and  $\sigma$ -pol/ $\Gamma$ MK plane) resemble much more the low temperature curves, although not completely probably due to remaining of domains where  $T > T_c$ .

Beyond the temperature dependent measurements, we also probed different photon energies. Figures 3.9 and 3.10 shows the Energy Distribution Map taken for the  $\Gamma$ M and  $\Gamma$ K direction, respectively. By probing the energy dependency, we were able explore different sample orientations, which can be relevant for the ARPES spectral weight of low hybridized states, and regions closer to the sample surface. This can be important because the CDW state could form only in domains around the surface level. The maps, however, do not show any feature indicating the reconstruction of the electronic structure. On the other hand, as we can see very evidently for the  $E_{kin} = 40.0$  eV, we have been able to capture a flat band around  $E_B \approx -0.7$  eV. This was a surprising result, considering that the first principles calculations [7] did not capture the introduction of these states in the system. This flat band lies precisely at the binding energy of the "kink" discussed above, from which we draw the conclusion that it is a signature of this flat band.

Thus, we propose that three phenomenon are occurring concurrently:

- The introduction of the Ni-d states forming a flat band at the binding energy of  $E_B \approx -1.2$  eV, which is not temperature dependent, although very dependent on the  $\sigma$ -pol of photons;
- The formation of other Ni flat states around  $E_B \approx -0.7$  eV. We attribute this feature as the cause of the "kink" discussed previously. This feature was also seen in the preliminary measurements with He-lamp (section 3.2), which means it is consistent for different sets of samples.;
- The shift of about  $100$  meV of the electronic structure towards the Fermi Level, which is temperature dependent rather than doping dependent. This feature could be an indication that the high temperature A point is no longer equivalent to the low temperature A point, pointing towards a reconstruction that

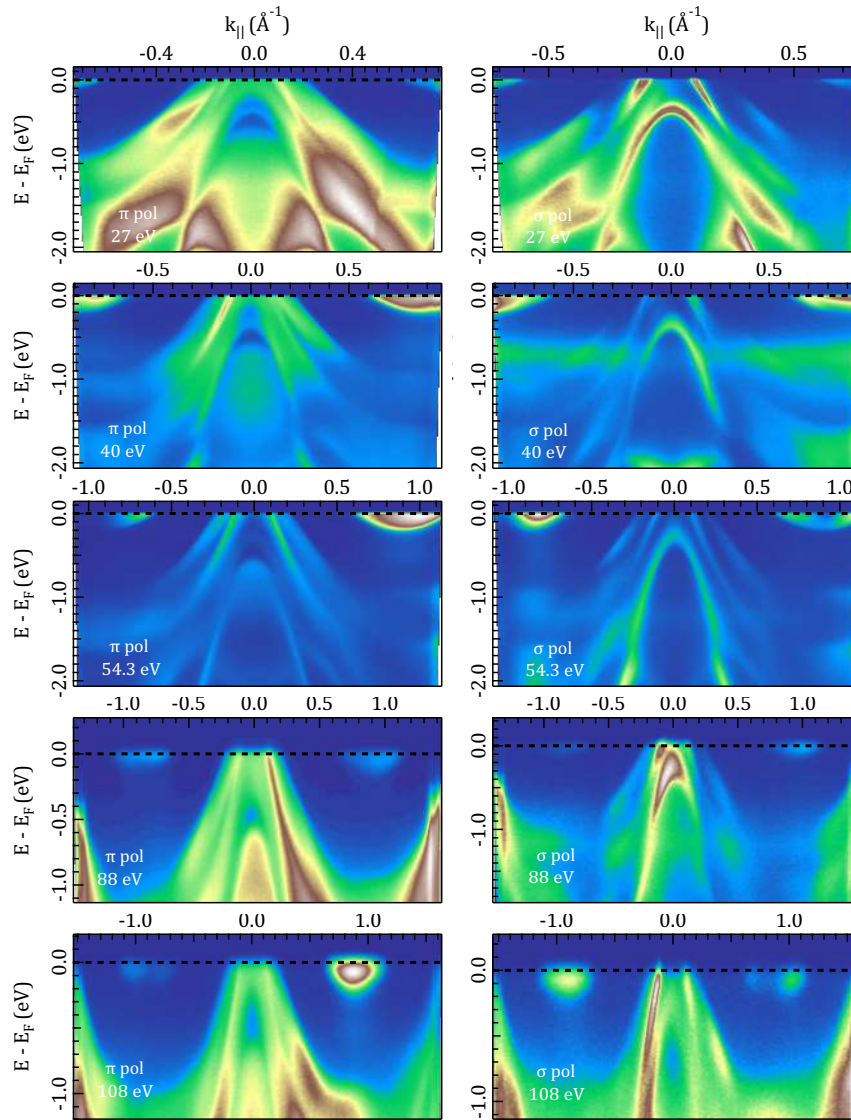


Figure 3.9: ARPES measurements of  $\text{Ni}_{0.05}\text{ZrTe}_2$  for  $\Gamma\text{M}$  high symmetry direction for different photon energy at both linear light polarization. All the energy maps taken for  $T = 20$  K.

is happening along the  $c$ -axis. However, more studies must be done in order to corroborate with this claim.

While we were unable to detect a definitive evidence of a characteristic electronic structure reconstruction of a CDW phase transition, the emergence of flat bands at binding energies of  $-0.7$  eV and  $-1.2$  eV provides a clear signature of changes in the electronic structure resulting from the Ni intercalation and these changes could be associated to the supposed CDW transition.

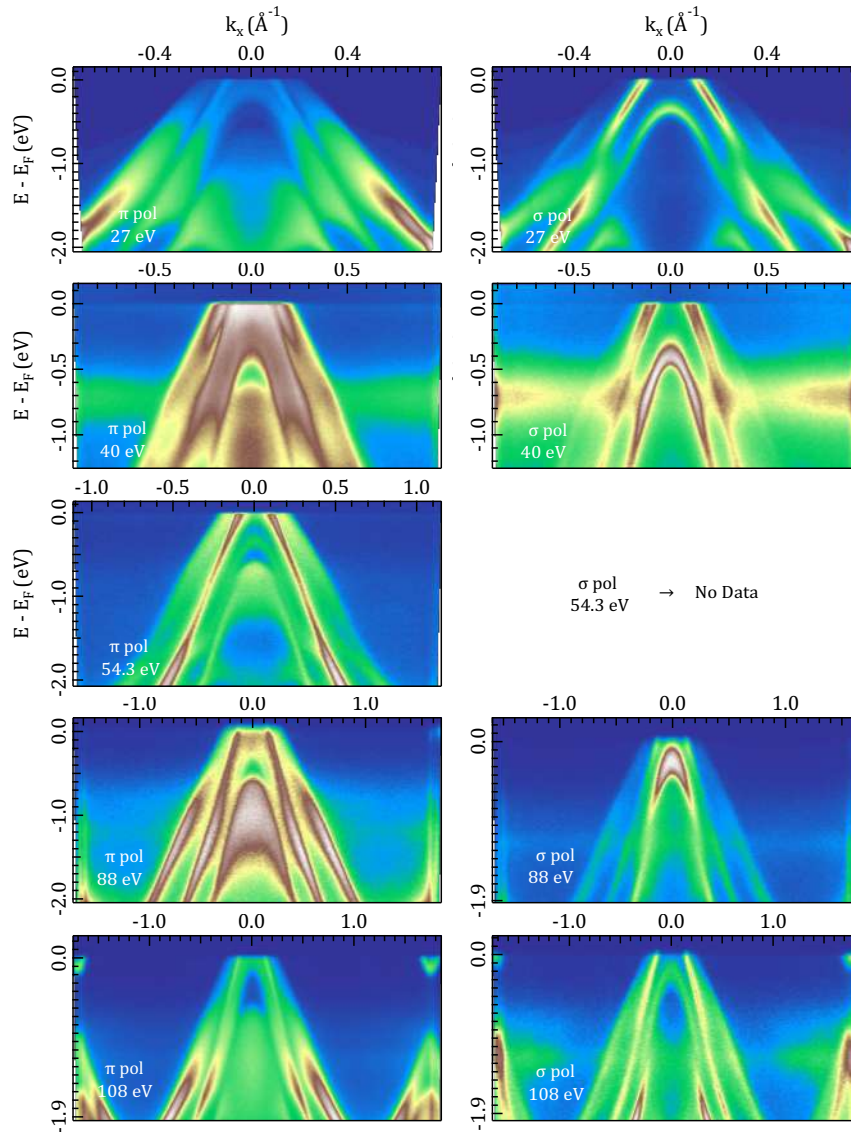


Figure 3.10: ARPES measurements of  $\text{Ni}_{0.05}\text{ZrTe}_2$  for  $\Gamma\text{K}$  high symmetry direction for different photon energy at both linear light polarization. All the energy maps taken for  $T = 20$  K.

In order to further characterize the changes in the electronic structure introduced by the Ni doping, we also employed the same procedure of MDC evaluation, which results are shown in Figure 3.11. This time, the estimated Fermi velocity for the  $\alpha_2$  band was  $v_F^\Gamma \approx 7.37(30) \times 10^5$  m/s for the  $\Gamma\text{MK}$  plane and  $v_F^A \approx 6.63(40) \times 10^5$  m/s for the ALH plane. Notably, we observe a gradual increase in the Fermi velocity going from the  $\Gamma$  plane to the A plane, which leads to a steeper linear dispersion. This new value represents approximately 70% of the Fermi velocity of graphene.

The Fermi Surface maps are shown in Figure A.3. They display the same topology discussed for the case

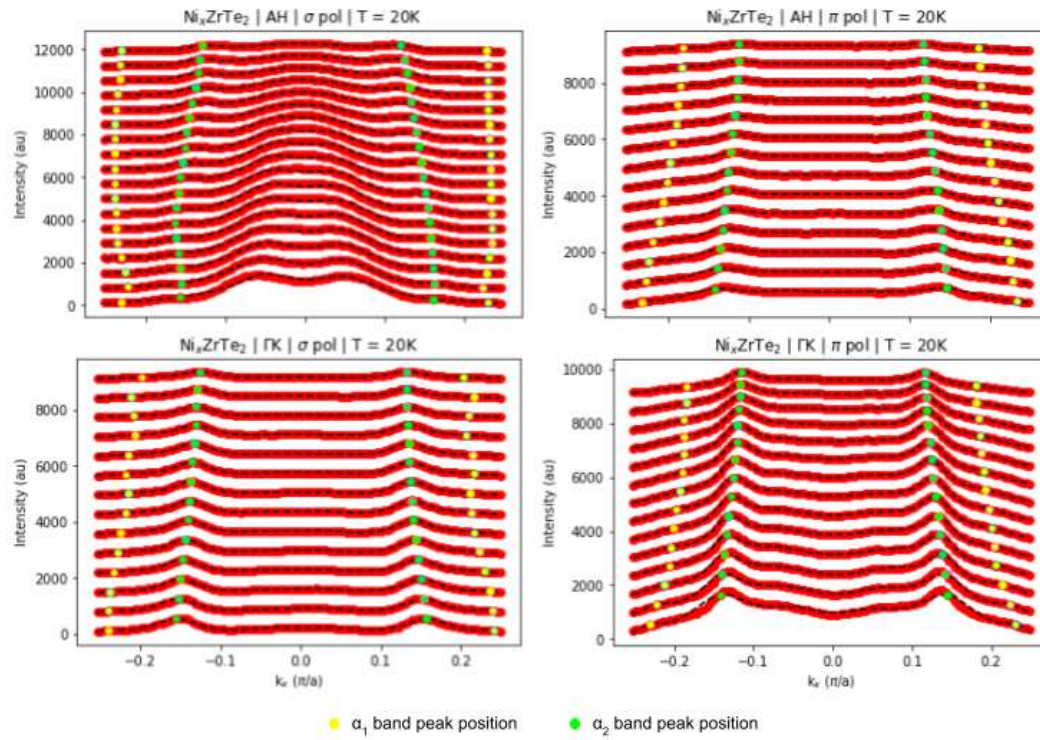


Figure 3.11: ARPES MDC analysis for the Ni-doped compound. Lorentzian fittings (dashed black lines) of several MDCs (red lines) for increasing binding energies (from 0.01 to -0.15 eV). Data for both light polarization and incident photon energy (88 eV and 108 eV), measured along  $\Gamma K$  at  $T = 20$  K for the Ni-doped compound, with triple band fitting (six Lorentzian peaks per profile). Only the bands  $\alpha_1$ , in yellow, and  $\alpha_2$ , in green, are highlighted.

of the parent compound. Again, no spectral weight associated to the reconstruction of the electronic structure could be identified. Despite that, in order to further complement the analysis of the Ni-doped system, we perform a quantitative calculation of the pockets area. The idea here was to verify the changes in the FS caused by the doping. The analysis was done as follows: with the FS maps in hands, the coordinate system was centralized at the pocket of interest; then, we obtained a series of MDCs centered around the origin with rotation angles from  $0^\circ$  to  $165^\circ$ , with  $15^\circ$  steps; four (two) Lorentzian curves were then adjusted for each MDC around the hole (electron) pocket; with this, a set of points constituting the pockets were obtained. Then, an ellipse was adjusted to these sets of points and the area of the ellipse was calculated by its standard formula. Figure 3.12 illustrates, as an example, this procedure.

We were, then, able to compare the different pocket sizes according to the Brillouin Zone plane and doping of the system. We can divide the results into two parts, as shown in Figure 3.13. The pocket  $\alpha_2$  remains constant in size, for both ALH and  $\Gamma K$  planes. On the other hand, the pocket  $\alpha_1$  presents a subtle trend towards increasing its size, consistently for both planes again. As for the case of the electron pocket

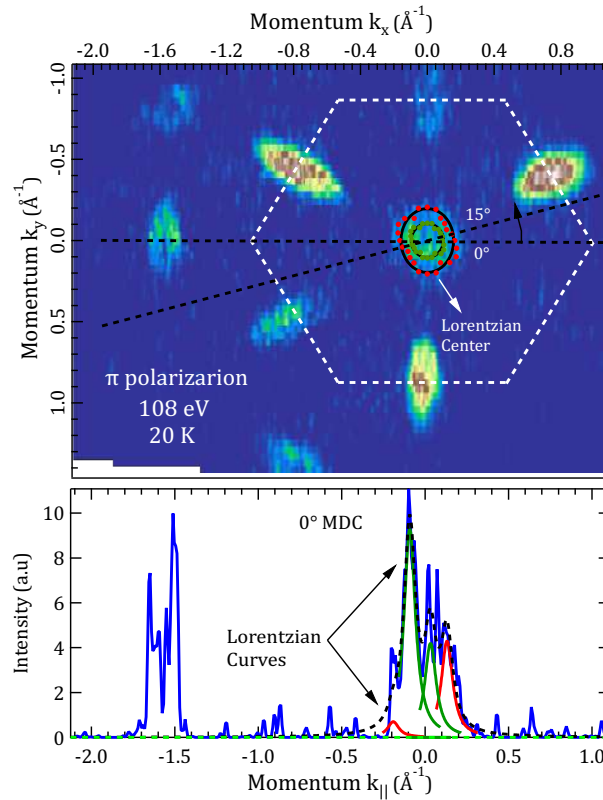


Figure 3.12: Upper panel: example of the ellipse fitting for the two hole pockets around the  $\Gamma$  point. The white hexagon delimits the 2D Brillouin Zone and the dashed black lines are the path of the Momentum Distribution Curves, taken with a  $15^\circ$  step as indicated. The red and green points are the Lorentzian curves centers for the  $\alpha_1$  and  $\alpha_2$  pockets, respectively. Lower panel: corresponding MDC for the  $0^\circ$  rotation. Four Lorentzian curves are fitted to the data, limited to the region around the center only.

$\beta$ , the uncertainty of each measurement is substantially large. This is because, in general, its spectral weight was vanishing in many cases (see Figures 3.5 and A.3). Because of that, even when one could say that there is a small increase in size for the  $\Gamma$  MK plane, for example, the relative error imposes a more conservative approach. In general, for the electron pocket, thus, the size remained constant.

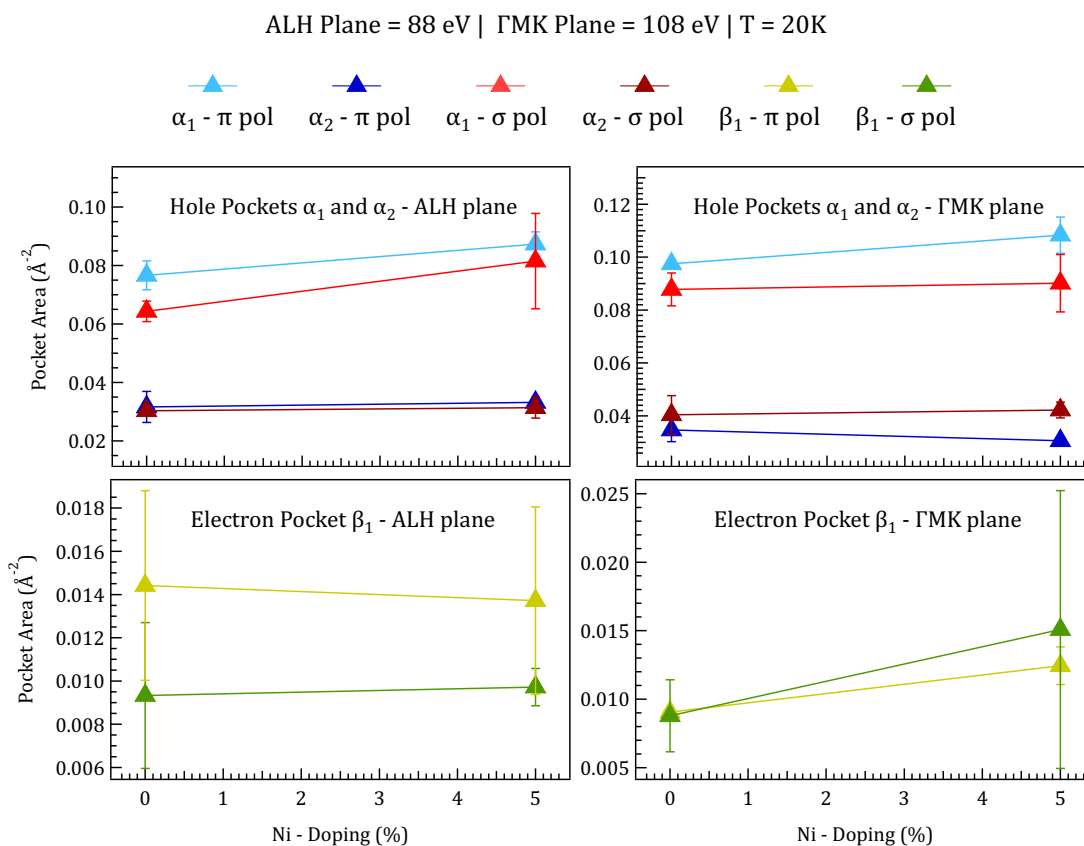


Figure 3.13: Ni-doping dependence of the pocket's areas. The left side compares the areas for the ALH plane and the right side, the  $\Gamma$ MK plane. The lines are simply a guideline to the visualization, connecting the points. Upper panel: hole pockets areas for the parent compound and the Ni-5% doped sample, for both light polarization. Lower panel: same as the other panel, but now for the electron pocket.



### 3.3.3 The Dy-doped Sample

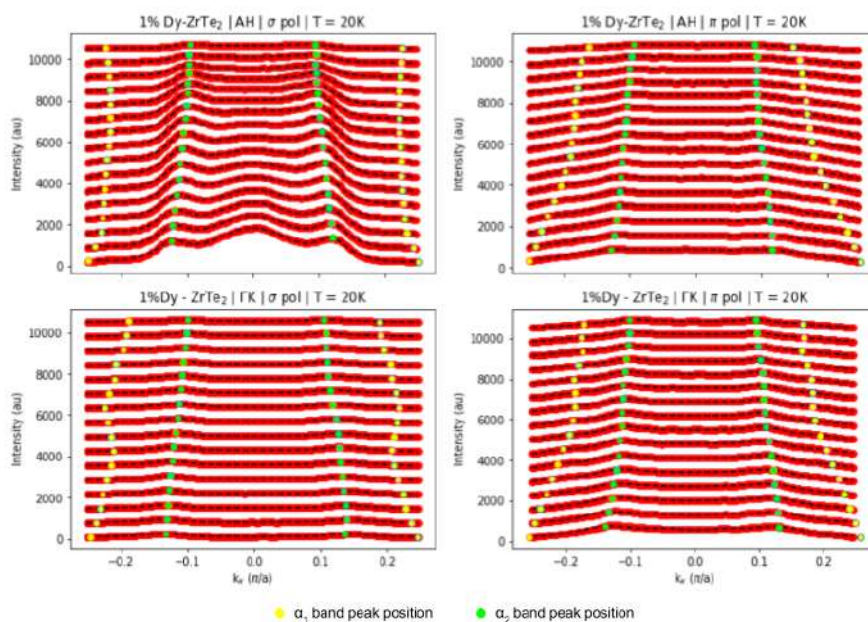
In the case of Dy doping, our investigation encompassed two distinct samples: 1%-Dy and 5%-Dy. These concentrations correspond to the near-optimal and over-doped regions, respectively, within the superconducting dome depicted in the phase diagram (Figure 1.4) [21, 7]. Analogously to the previous cases, we conducted synchrotron light ARPES experiments employing both linear light polarizations and directions of high symmetry ( $\Gamma M$  and  $\Gamma K$ ).

The Energy Maps are displayed in Figures 3.15 and 3.16, revealing that the spectral features identified here are similar to those observed in the parent compound. Specifically, all the  $\alpha$  hole-like bands and the  $\beta$  electron-like band are present in both doped systems. We also see a redistribution of spectral weight associated to the bands, a feature expected from a new orbital hybridization of electronic states upon Dy intercalation in the system.

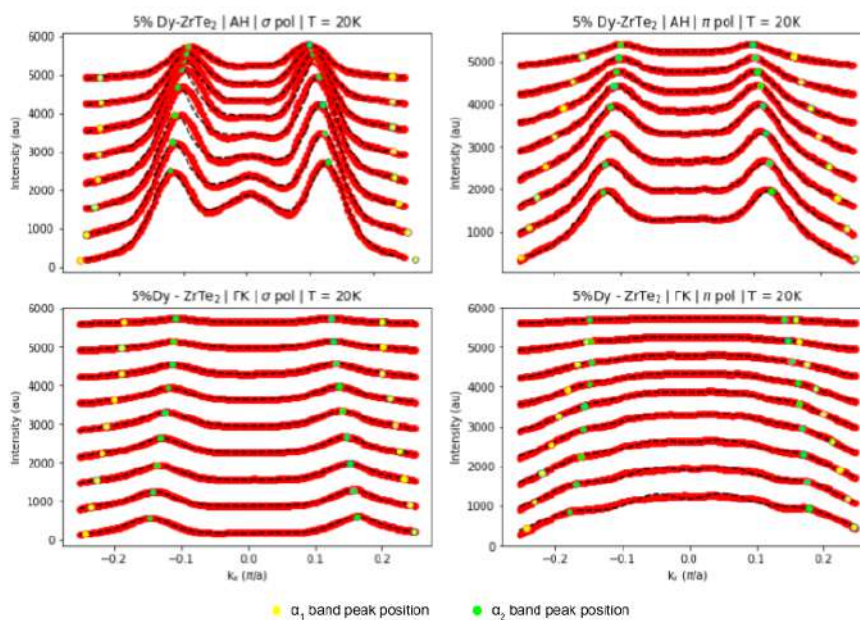
As done in both previous cases, we also adopted the MDC evaluation procedure to characterize the alterations in the Dirac cone structure. The fitting results are presented in Figure 3.14. For the case of 1% Dy doping, we estimated Fermi velocity for the  $\alpha_2$  band of  $v_F^\Gamma \approx 5.83(16) \times 10^5$  m/s at the  $\Gamma$  plane and of  $v_F^A \approx 6.89(7) \times 10^5$  m/s at the A plane. For 5% Dy doping, the estimated Fermi velocity for the  $\alpha_2$  band was  $v_F^\Gamma \approx 6.61(35) \times 10^5$  m/s at the  $\Gamma$  plane and  $v_F^A \approx 7.30(12) \times 10^5$  m/s at the A plane.

As done previously, we also computed the pocket sizes to investigate any significant alterations in the electronic structure of these doped systems. The same methodology discussed in section 3.3.2 was employed for the pocket area calculations, yielding results displayed in Figure 3.17. Here, on the other hand, the doping dependence showcases an interesting characteristic. There is a small reduction in the pocket area for the 1% doping compared to the other cases. This diminishment is evident in two Brillouin Zone (BZ) regions: firstly, within the ALH plane, where the  $\beta$  pocket experiences this reduction, whereas the hole pockets remain constant. Secondly, within the  $\Gamma MK$  plane, a reversal of roles occurs, with the hole pockets  $\alpha_1$  and  $\alpha_2$  diminishing in size, while the electron pocket remains unchanged.

Upon increasing the doping level to 5%, the pocket areas return to values consistent with those of the parent compound. Interestingly, the 1% Dy doped sample displays a small decrease in  $v_F$  at the  $\Gamma$  plane, a feature that resembles closely the behaviour of the pocket size. This non-monotonic behavior resembles the phase diagram for Dy doping in  $ZrTe_2$ . Specifically, 1% doping aligns closely with the peak of the superconducting dome, while 5% doping falls well beyond any superconducting phase transition.



(a)



(b)

Figure 3.14: ARPES MDC analysis for both Dy-doped compounds. Lorentzian fittings (dashed black lines) of several MDCs (red lines) for increasing binding energies (from 0.01 to -0.15 eV). Data for both light polarization and incident photon energy (88 eV and 108 eV), measured along  $\Gamma K$  for the parent compound, with triple band fitting (six Lorentzian peaks per profile). Only the bands  $\alpha_1$ , in yellow, and  $\alpha_2$ , in green, are highlighted.

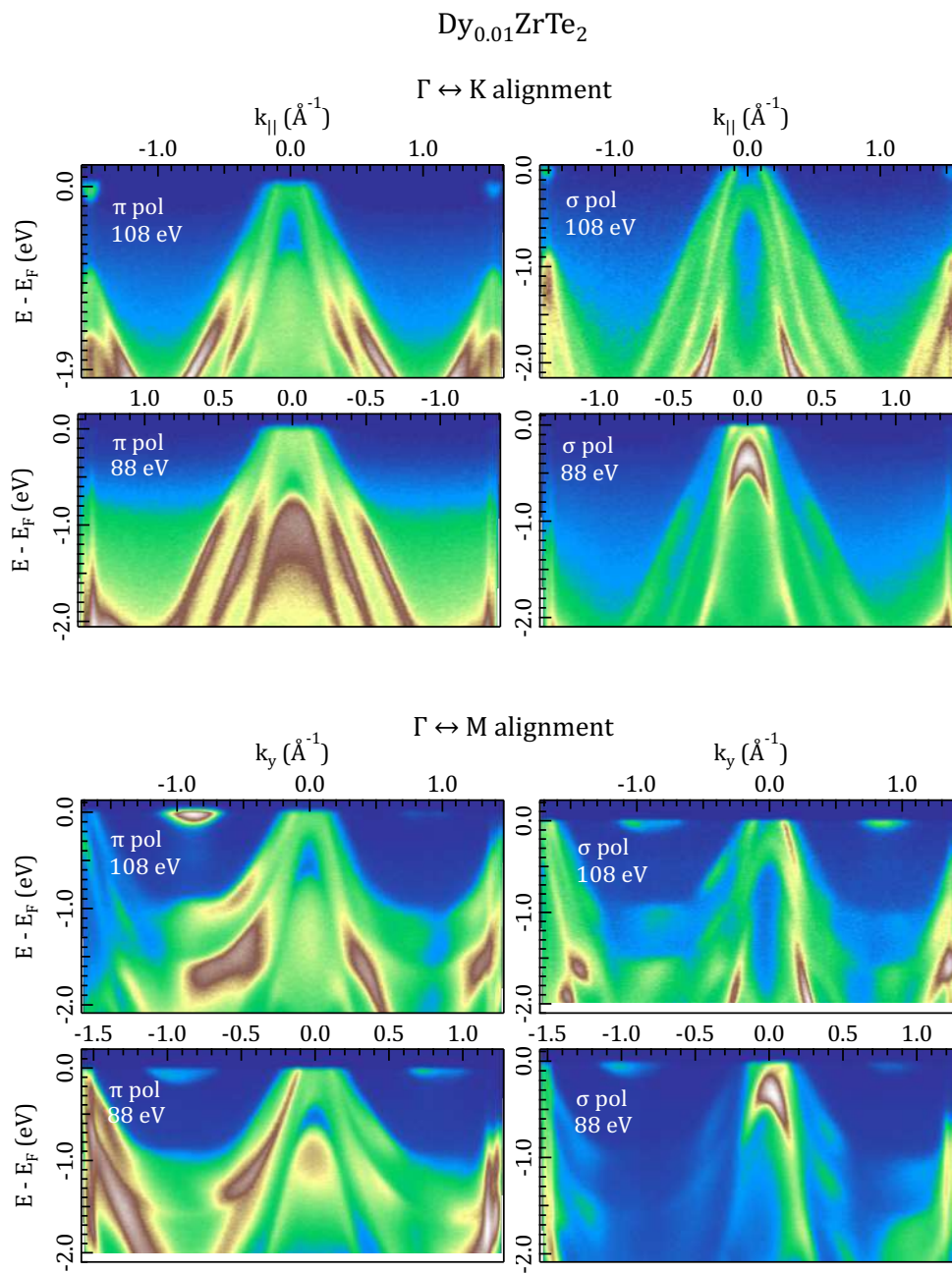


Figure 3.15: ARPES measurements of  $\text{Dy}_{0.01}\text{ZrTe}_2$  for both high symmetry direction and both linear light polarization. Measurements taken at 20 K.

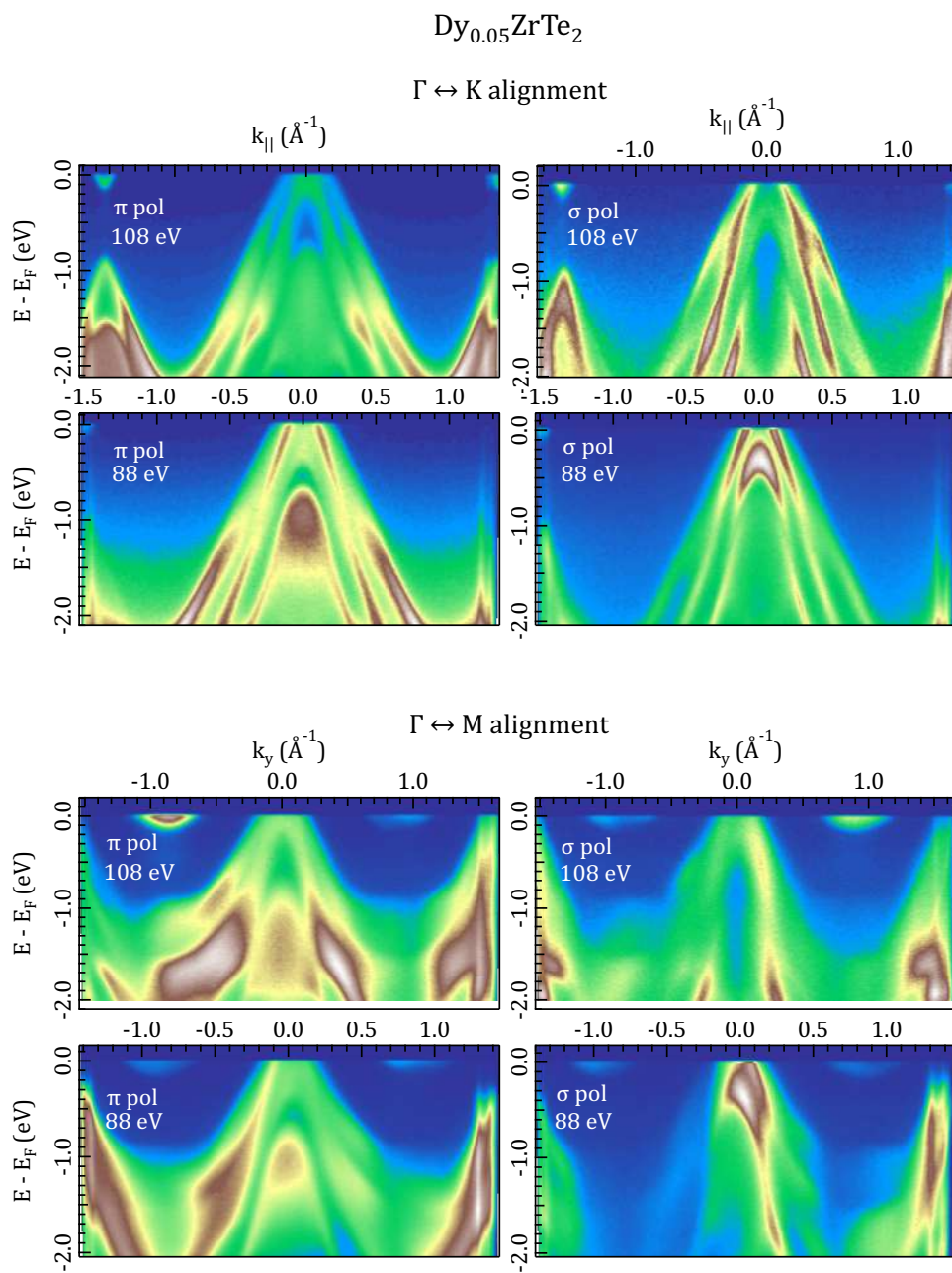


Figure 3.16: ARPES measurements of  $\text{Dy}_{0.05}\text{ZrTe}_2$  for both high symmetry direction and both linear light polarization. Measurements taken at 20 K.

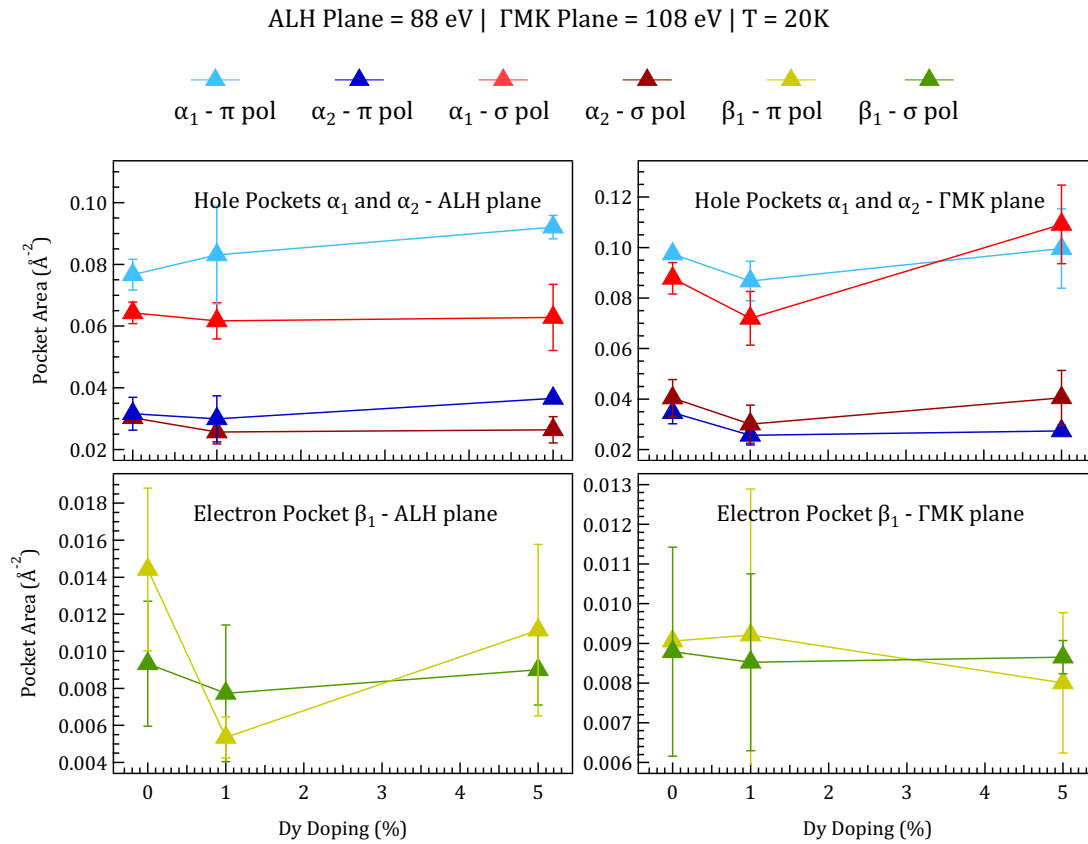


Figure 3.17: Dy-doping dependence of the pocket's areas. The left side compares the areas for the ALH plane and the right side, the  $\Gamma$ MK plane. The lines are simply a guideline to the visualization, connecting the points. Upper panel: hole pockets areas for the parent compound and the Ni-5% doped sample, for both light polarization. Lower panel: same as the other panel, but now for the electron pocket.

### 3.4 Fermi Surface Nesting Analysis

As discussed in section 1.2.2, the topology of the FS can play a very important role leading the system into a charge density wave phase transition. Thus, in order to evaluate the relevance of this characteristic in our systems, we performed a quantitatively analysis of the nesting phenomenon. The  $\text{ZrTe}_2$  system presents, as seen in section 3.3.1, two circular hole pockets around the  $\Gamma/A$  points and one elliptical electron pocket around the M point in its FS. So, vectors connecting the hole pockets to the electron pocket could be such that they are commensurate with the underlying lattice of the system. The procedure adopted here to measure the pockets was the same discussed in the previous section. With the set of points which composed the pockets in hands, we made two different analysis. One was to verify the occurrence of the nesting phenomenon in the system and the other was to check the frequency of commensurate nesting.

First, we defined a nesting vector as  $\vec{Q} = (x_2 - x_1, y_2 - y_1)$ , where  $x_1$  and  $y_1$  are the coordinates of the points obtained for the hole pockets and  $x_2$  and  $y_2$  are the coordinates of the points obtained for the electron pockets, as exemplified in Figure 3.18. We see, thus, that the nesting here is with respect to the electron-hole pockets. We compared, then, each vector  $\vec{Q}_n$  with all other possible  $\vec{Q}_m$ , in order to find those which had a compatibility of 5% or better. Only the sets of vectors which had at least two pairs were considered - i.e, a

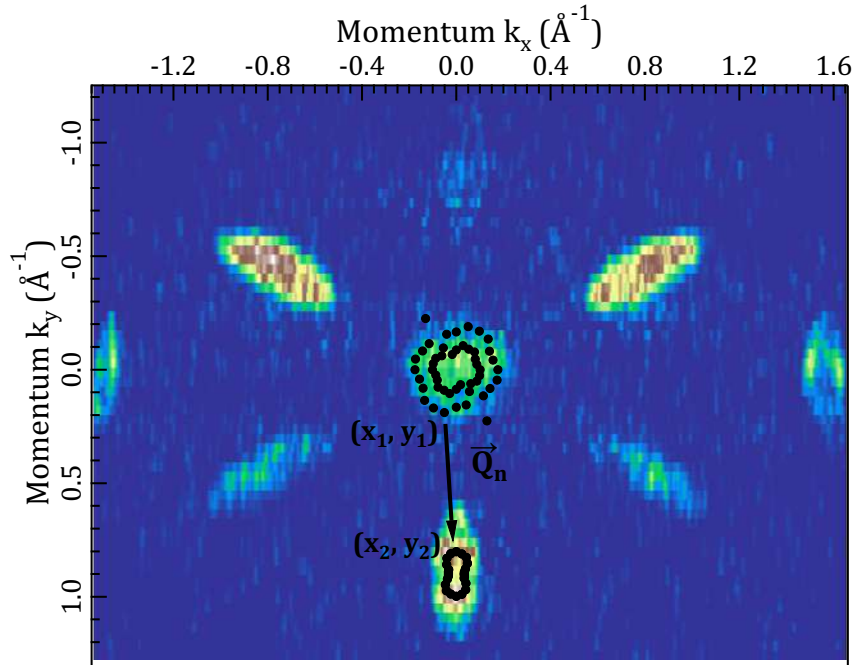


Figure 3.18: The black dots represent the positions of the centers of the fitted Lorentzian Curves in the Momentum Distribution Curves (as discussed in section 3.3.2). The black arrow shows an example of Nesting Vector, connecting a dot from the hole pocket to other dot on the electron pocket.

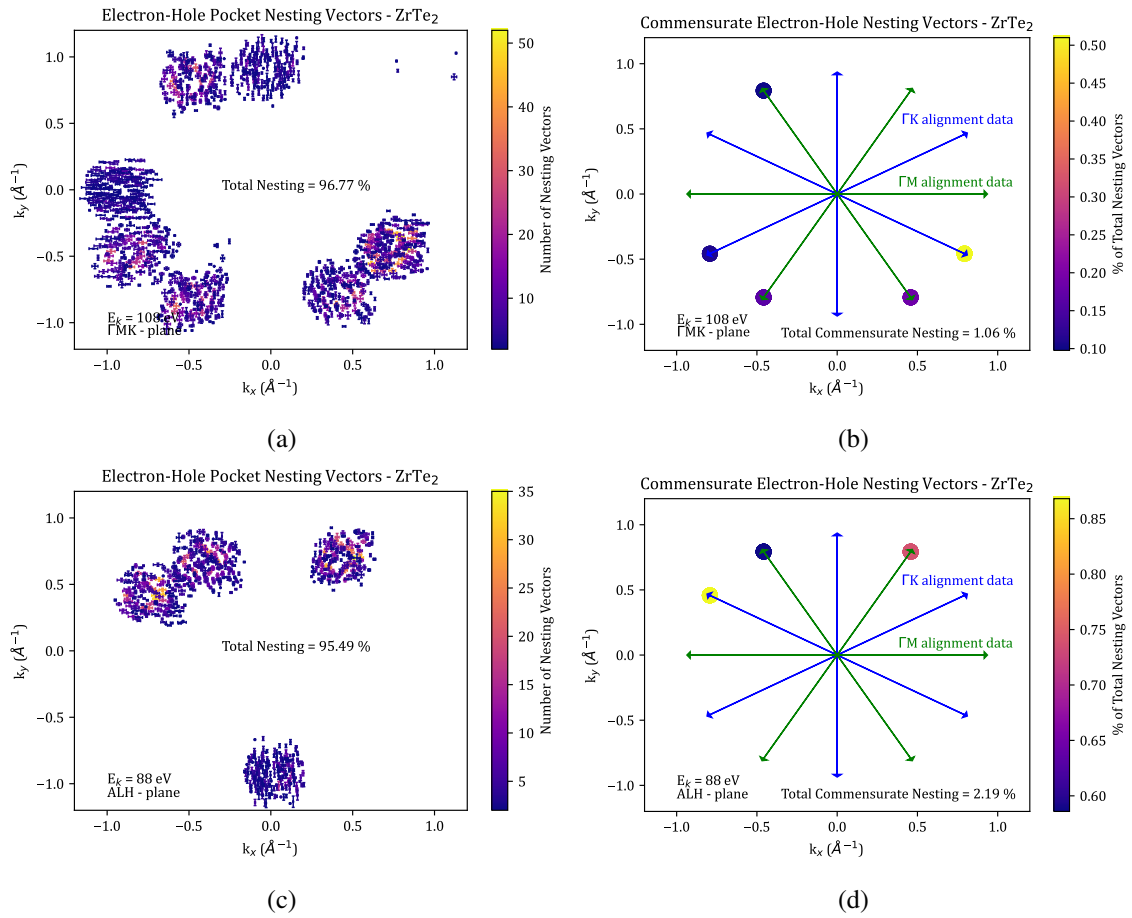


Figure 3.19: (a): Collection of coordinates for all the nesting vectors in the system of  $\text{ZrTe}_2$  at the  $\Gamma\text{MK}$  plane. (see the definition used for nesting vector in the text). Each point in the graph indicates a set (the size of the set is indicated by the colormap) of nesting vectors with coordinates indicated by the x and y-axis. (b): Group of commensurate nesting vectors for the same system. The drawn vectors are the lattice commensurate vectors. They are divided into two subgroups from the experimental data: the commensurate vectors aligned with the  $\Gamma\text{K}$  direction (blue) and with the  $\Gamma\text{M}$  direction (green). Each dot in the plot indicates a set of vectors compatible with the respect commensurate vector. Further explanation and discussion is provided in the text of the section. (c)-(d): The same for the (a) and (b), but for the ALH Brillouin Zone plane.

vector which was not compatible with any other was not taken into account. This gives us an idea of how much "nested" the FS actually is, in the sense of what are the repeated vectors the connect the electron to the hole pockets and with what frequency.

As for the second analysis, we compared the nesting vectors obtained from the experimental data with the commensurate vectors  $\vec{q}_c = (0, |\Gamma\text{M}|)$  and its  $60^\circ$  rotations analogues, in order to verify if a possible nesting of the system would be compatible with a commensurable wave vector. Note that  $\vec{q}_c = \frac{\vec{b}_2}{2}$  is a half integer of a base vector and by rotating it by  $60^\circ$  we get to equivalent points in the reciprocal space. There is, however, a certain observation to be pointed out here. When measuring the Fermi Surface maps, the sample

would be positioned in such a way that the angle-axis (or momentum-axis) was parallel to the  $\Gamma M$  or to the  $\Gamma K$  direction, depending on which energy map was of interest. This means that, depending on this alignment, the vector  $\vec{q}_c$  could be rotated by  $30^\circ$  - equivalently it would be defined as  $\vec{q}_c = (|\Gamma M|, 0)$ . So, the nesting vectors had to be compared with actually two sets of commensurate vectors, one set with the  $\vec{q}_c = (0, |\Gamma M|)$  and its analogues, and other set with  $\vec{q}_c = (|\Gamma M|, 0)$  and its analogues. These two sets of commensurate vectors are represent in Figure 3.19 as blue and green vectors.

The results obtained for the parent compound  $ZrTe_2$  are shown in Figure 3.19. The general nesting of the system at the  $\Gamma MK$  plane ( $E_{kin} = 108$  eV) was found to be of 96.77%, which means that only around 3% of the nesting vectors were not compatible (within the 5% tolerance) with any other. This scenario is essentially the same for the ALH plane ( $E_{kin} = 88$  eV), with a general nesting of 95.49%. However, when checking for the compatibility with commensurate vectors, we see a drastic change: only 1.06% (2.19%) of the experimental measured nesting vectors are compatible with commensurability for the  $\Gamma MK$  (ALH) plane. This an indication that, although nesting isn't itself difficult to occur, commensurate nesting is a very weak condition in the  $ZrTe_2$  system.

For the case of the Ni-doped sample, the results are shown in Figure 3.20. Here, the general nesting is approximately the same as in the previous case, with 95.70% (97.16%) for the  $\Gamma MK$  (ALH) plane. The small changes in the percentages have a strong relation with the quality of the available data for the analysis, i.e, variation in the spectral signal of the pockets. The same tendency for the weak commensurate is seen as well, with a compatibility with commensurate vectors of 1.87% (1.56%) for the  $\Gamma MK$  (ALH) plane. Both of these results indicate that the doping with Ni does not change the nesting conditions in a relevant way.

Lastly, we have the case of the Dy-doped compounds, shown in Figures 3.21 and 3.22. Different from the case of the Ni doping, here the nesting conditions seen to be more affected by Dy the doping. The general nesting picture is essentially the same of the previous cases, in the range of around 95% for the two doping cases (see graphs for details). However, the commensurate nesting presents a slightly different result. Although for the 5% Dy-doping it stays at around 1.50%, as in the cases of the parent and Ni-doped compounds, there is a subtle increase when going from the  $\Gamma MK$  to the ALH plane of the 1% Dy-doped compound, from 1.40% to 4.11%, which is about 3 times as large as the values yield for all other cases.

When we take into consideration the SC phase diagram of the  $Dy_xZrTe_2$  system (see Figure 1.4), it is possible to propose an explanation to the results found. We observe that for a high doping, the superconducting dome vanishes, essentially recovering the conditions of the parent compound. This is also what happens for our nesting vector analysis: for both the parent compound and 5%-Dy doping the nesting compatibility is approximately the same, around 1.1% for the  $\Gamma MK$  plane and with a small decrease from 2.19% to 1.28%. On the other hand, the 1% Dy-doping sits well within the superconducting dome. Its compatibility with commensurate nesting, when compared to the parent compound, has a slight increase, from 2.19% to 4.11%, which means that it could be almost twice as large and, thus, relevant for a phase transition.



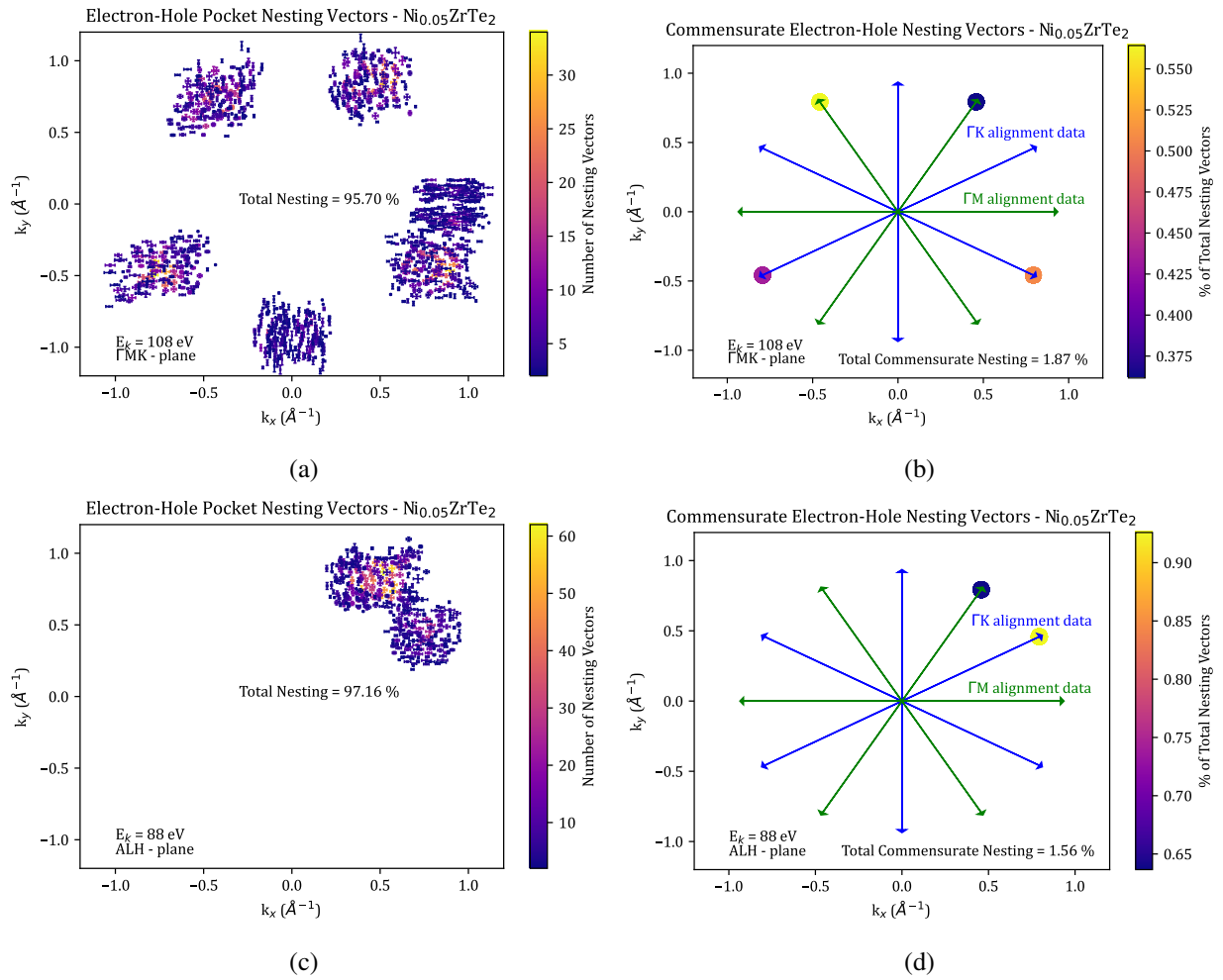


Figure 3.20: (a) and (c): Collection of coordinates for all the nesting vectors in the system of  $\text{Ni}_{0.05}\text{ZrTe}_2$  at the  $\Gamma\text{MK}$  and AHL plane, respectively. (b) and (d): Group of commensurate nesting vectors for the same system, for the  $\Gamma\text{MK}$  and AHL planes.

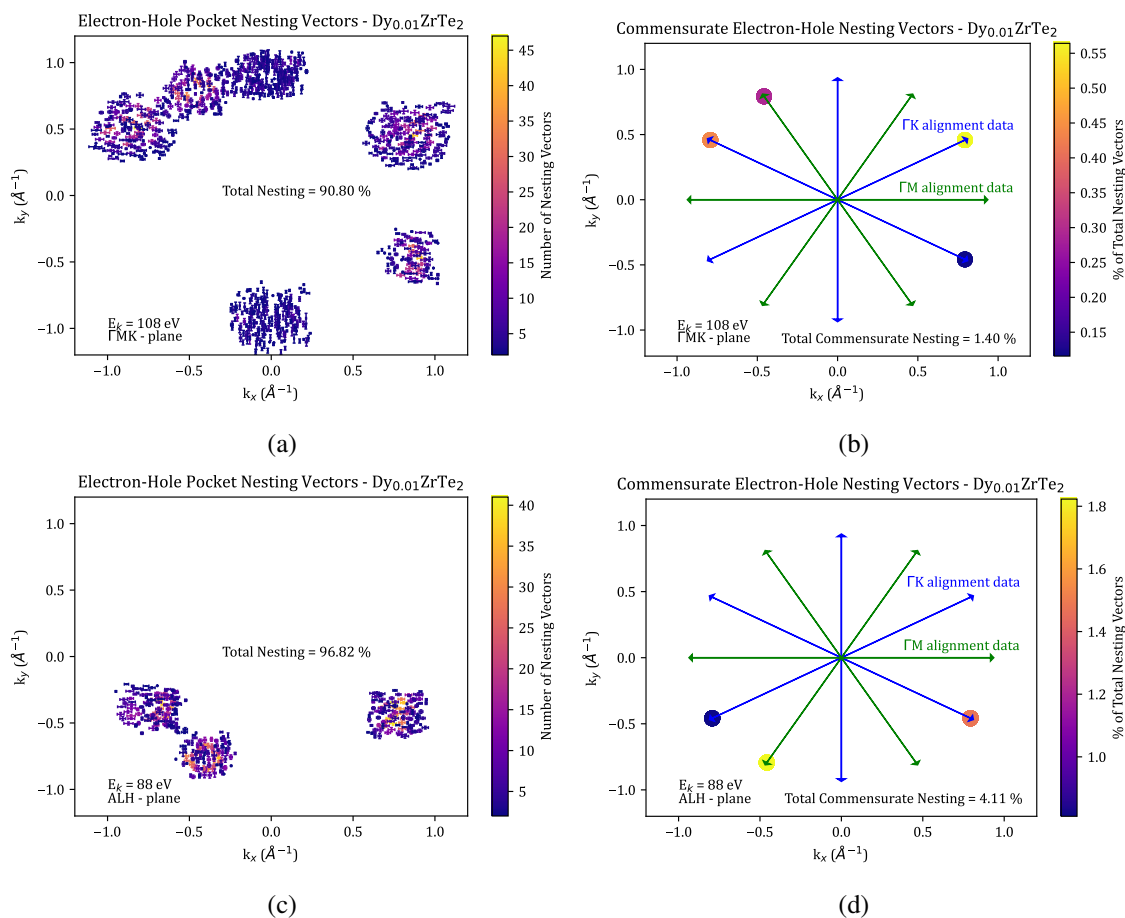


Figure 3.21: (a) and (c): Collection of coordinates for all the nesting vectors in the system of  $\text{Dy}_{0.01}\text{ZrTe}_2$  at the  $\Gamma\text{MK}$  and AHL plane, respectively. (b) and (d): Group of commensurate nesting vectors for the same system, for the  $\Gamma\text{MK}$  and AHL planes.

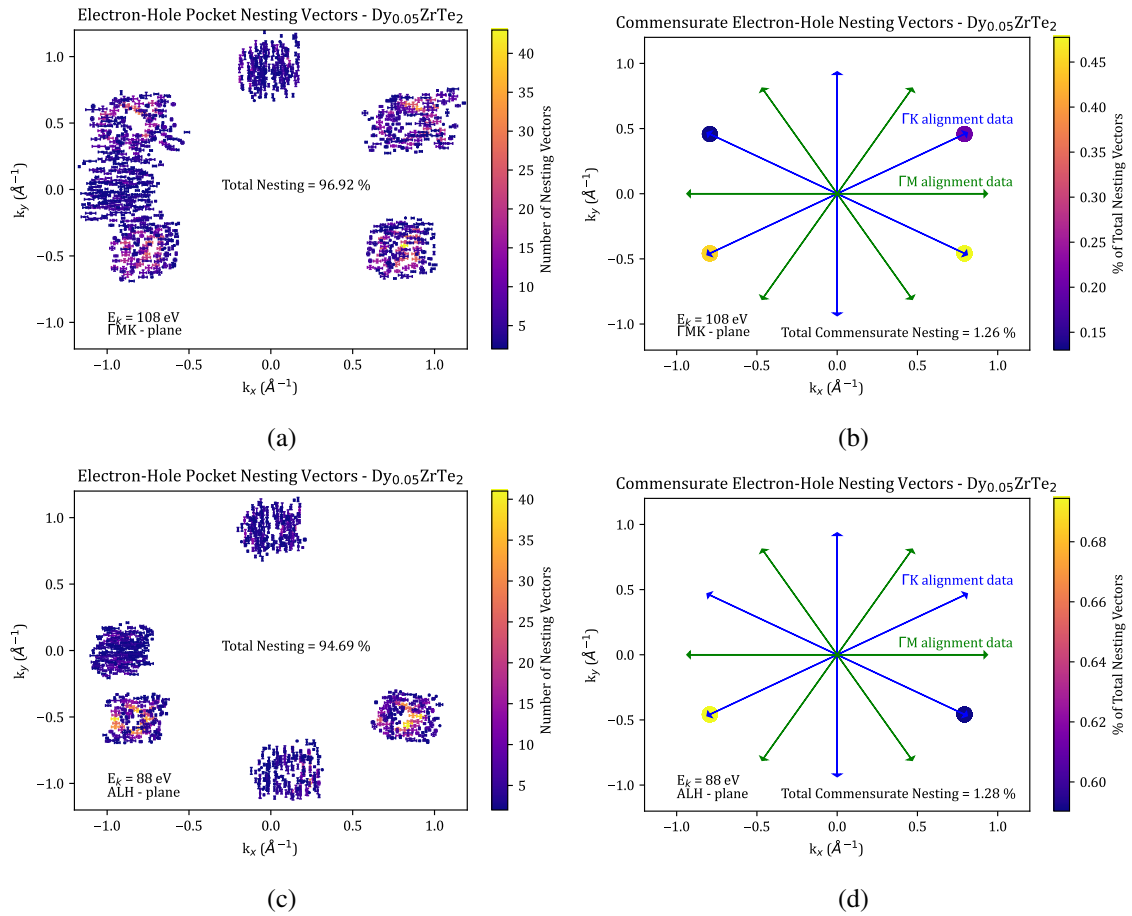


Figure 3.22: (a) and (c): Collection of coordinates for all the nesting vectors in the system of  $\text{Dy}_{0.05}\text{ZrTe}_2$  at the  $\Gamma\text{MK}$  and AHL plane, respectively. (b) and (d): Group of commensurate nesting vectors for the same system, for the  $\Gamma\text{MK}$  and AHL planes.



## Chapter 4

# Conclusion

This dissertation offers an informative ARPES study of 1T-ZrTe<sub>2</sub> and its Ni and Dy intercalated derivatives. The primary motivation behind investigating these materials was to explore their electronic characteristics and the modifications induced by both charge density wave (CDW) and superconducting (SC) transitions.

In the case of the ZrTe<sub>2</sub> compound, our measurements unveiled a band structure closely aligned with previous first-principle calculations [7] and consistent with other experimental findings [13, 12]. This overarching band structure comprises two hole pockets centered around the  $\Gamma$  point and one electron pocket near the M point, with a linearly dispersed band intersecting the Fermi Level.

For the Ni-doped sample, the anticipated features associated with band folding, indicative of a charge density wave (CDW) phase transition, were notably absent. However, the introduction of flat band Ni-d states was evident upon transition metal intercalation, in alignment with density of states (DOS) calculations [7]. The spectral weight of these flat bands was notably concentrated around a binding energy ( $E_B$ ) of approximately -1.2 eV for  $E_{kin} = 108/88$  eV. Further experiments with varying incident photon energies unveiled an additional flat band, situated at  $E_B \approx -0.7$  eV for  $E_{kin} = 40$  eV.

Two plausible explanations emerge from these observations. The band structure may indeed encompass two distinct flat band states, supported by the discernible kink in the spectral weight of the energy distribution curve (EDC) precisely around  $\Gamma$  at  $E_B \approx -0.7$  eV. The absence of simultaneous observation of both flat bands may be attributed to the fact that these measurements were conducted on different days, utilizing different samples and experimental alignments.

Alternatively, conducting the experiment with a lower incident photon energy may provide a glimpse into the electronic structure of only the first few surface layers of the material. This suggests that the second flat band observed could potentially be a surface state rather than a representation of the bulk material's electronic structure.

Regarding Fermi surface analysis of the Ni-doped samples, it was discerned that doping had a negligible impact on pocket sizes, remaining relatively constant within the margin of error. This consistency aligns with

the results of the commensurability analysis, which revealed an average commensurability of 1.87% (1.56%) for the  $\Gamma$  (A) plane, closely resembling the values of 1.06% (2.19%) observed in the parent compound. This suggests that in both the parent compound and the Ni-doped sample, the compatibility of nesting vectors with the commensurate vectors of the lattice is a weak condition, likely playing an inconsequential role in any material transitions.

Regarding the Dy-doped samples, we did not observe any significant changes indicative of the introduction of flat bands. The fundamental electronic structure of the system remained consistent, albeit with slight modifications in the spectral weight (SW) attributed to the incorporation of Dy f-states, resulting in orbital mixing. However, a noteworthy observation arises from our pocket size analysis. We identified a non-monotonic behavior in the electron and hole pockets as a function of doping. Specifically, with a 1% Dy doping, both the electron pocket area at  $\Gamma$  and the hole pocket area at A exhibited a modest decrease. Surprisingly, upon increasing the doping to 5%, these areas reverted to values akin to those of the parent compound.

This non-monotonic trend was corroborated by our nesting commensurability analysis. For 1% Dy doping, we calculated an increase in commensurability from 2.19% to 4.11%. However, when the doping level was elevated to 5%, this value decreased to 1.26%, resembling the commensurability of the parent compound. It's important to exercise caution when interpreting these values due to the inherent uncertainty associated with the fitting method. Nonetheless, they intriguingly reflect the non-monotonic behavior observed in the superconducting (SC) dome of the  $\text{Dy}_x\text{ZrTe}_2$  phase diagram, where superconductivity is lost when  $x = 5\%$ .

In conclusion, the  $\text{ZrTe}_2$  system represents a promising and relatively unexplored material that has only recently garnered attention in the research community. As such, there exists a substantial opportunity for further exploration in terms of both experimental techniques and theoretical frameworks. This study has shed light on the essential aspects of the electronic structure of  $\text{ZrTe}_2$ , as well as its compounds intercalated with Ni and Dy. However, it is crucial to acknowledge that many of its properties remain enigmatic, underscoring the significance of continued empirical and theoretical investigations into  $\text{ZrTe}_2$ . We anticipate that the findings presented in this work will contribute to the broader understanding of charge density wave (CDW) and superconductivity (SC) in transition metal dichalcogenide (TMD) materials, thereby inspiring new avenues of research and innovative proposals in this exciting field.

# Bibliography

- [1] Sajedeh Manzeli et al. “2D transition metal dichalcogenides”. en. In: *Nature Reviews Materials* 2.8 (June 2017). Number: 8 Publisher: Nature Publishing Group, pp. 1–15. ISSN: 2058-8437. DOI: 10.1038/natrevmats.2017.33. URL: <https://www.nature.com/articles/natrevmats201733> (visited on 03/24/2022).
- [2] Charles Kittel. *Introduction to Solid State Physics*. Edição: 8th. Hoboken, NJ: John Wiley & Sons, Nov. 2004. ISBN: 978-0-471-41526-8.
- [3] Steven H. Simon. *The Oxford Solid State Basics*. Edição: 1. Oxford: Oxford University Press, Usa, Aug. 2013. ISBN: 978-0-19-968077-1.
- [4] Gang Hee Han et al. “van der Waals Metallic Transition Metal Dichalcogenides”. In: *Chemical Reviews* 118.13 (July 2018). Publisher: American Chemical Society, pp. 6297–6336. ISSN: 0009-2665. DOI: 10.1021/acs.chemrev.7b00618. URL: <https://doi.org/10.1021/acs.chemrev.7b00618> (visited on 03/24/2022).
- [5] G. Dresselhaus. “Spin-Orbit Coupling Effects in Zinc Blende Structures”. In: *Phys. Rev.* 100 (2 Oct. 1955), pp. 580–586. DOI: 10.1103/PhysRev.100.580. URL: <https://link.aps.org/doi/10.1103/PhysRev.100.580>.
- [6] E I Rashba and V I Sheka. “Symmetry of Energy Bands in Crystals of Wurtzite Type II. Symmetry of Bands with Spin-Orbit Interaction Included”. In: ().
- [7] Lucas E. Correa et al. “Evidence for multiband superconductivity and charge density waves in Ni-doped ZrTe<sub>2</sub>”. In: *Journal of Alloys and Compounds* 907 (June 25, 2022), p. 164477. ISSN: 0925-8388. DOI: 10.1016/j.jallcom.2022.164477. URL: <https://www.sciencedirect.com/science/article/pii/S0925838822008684> (visited on 09/23/2022).
- [8] Fernando A. Garcia. *Lecture Notes: Graphene. 2022*. URL: <https://drive.google.com/file/d/1Lc6EIuR7VuAucYPeXwWa4l6D-ThtCshV/view> (visited on 09/14/2023).
- [9] K. S. Novoselov et al. “Two-dimensional gas of massless Dirac fermions in graphene”. In: *Nature* 438.7065 (Nov. 2005), pp. 197–200. ISSN: 0028-0836, 1476-4687. DOI: 10.1038/nature04233. URL: <http://www.nature.com/articles/nature04233> (visited on 09/19/2022).

- [10] Aaron Bostwick et al. “Quasiparticle dynamics in graphene”. In: *Nature Physics* 3.1 (Jan. 2007). Number: 1 Publisher: Nature Publishing Group, pp. 36–40. ISSN: 1745-2481. DOI: 10.1038/nphys477. URL: <https://www.nature.com/articles/nphys477> (visited on 01/11/2024).
- [11] Imran Saeed, Hyuk Kyu Pak, and Tsvi Tlusty. “Quasiparticles, flat bands and the melting of hydrodynamic matter”. In: *Nature Physics* 19.4 (Apr. 2023). Number: 4 Publisher: Nature Publishing Group, pp. 536–544. ISSN: 1745-2481. DOI: 10.1038/s41567-022-01893-5. URL: <https://www.nature.com/articles/s41567-022-01893-5> (visited on 01/11/2024).
- [12] Polychronis Tsipas et al. “Massless Dirac Fermions in ZrTe<sub>2</sub> Semimetal Grown on InAs(111) by van der Waals Epitaxy”. en. In: *ACS Nano* 12.2 (Feb. 2018), pp. 1696–1703. ISSN: 1936-0851, 1936-086X. DOI: 10.1021/acsnano.7b08350. URL: <https://pubs.acs.org/doi/10.1021/acsnano.7b08350> (visited on 06/05/2023).
- [13] Indrani Kar et al. “Metal-chalcogen bond-length induced electronic phase transition from semiconductor to topological semimetal in  $\text{ZrX}_2$  ( $X = \text{Se}$  and Te)”. In: *Physical Review B* 101.16 (Apr. 20, 2020), p. 165122. DOI: 10.1103/PhysRevB.101.165122. URL: <https://link.aps.org/doi/10.1103/PhysRevB.101.165122> (visited on 08/07/2021).
- [14] Feng Tang et al. “Comprehensive search for topological materials using symmetry indicators”. In: *Nature* 566.7745 (Feb. 2019). Number: 7745 Publisher: Nature Publishing Group, pp. 486–489. ISSN: 1476-4687. DOI: 10.1038/s41586-019-0937-5. URL: <https://www.nature.com/articles/s41586-019-0937-5> (visited on 09/06/2023).
- [15] Emil J. Bergholtz and Zhao Liu. “Topological flat band models and fractional chern insulators”. In: *International Journal of Modern Physics B* 27.24 (Sept. 30, 2013). Publisher: World Scientific Publishing Co., p. 1330017. ISSN: 0217-9792. DOI: 10.1142/S021797921330017X. URL: <https://www.worldscientific.com/doi/10.1142/S021797921330017X> (visited on 01/11/2024).
- [16] Evelyn Tang and Liang Fu. “Strain-induced partially flat band, helical snake states and interface superconductivity in topological crystalline insulators”. In: *Nature Physics* 10.12 (Dec. 2014). Number: 12 Publisher: Nature Publishing Group, pp. 964–969. ISSN: 1745-2481. DOI: 10.1038/nphys3109. URL: <https://www.nature.com/articles/nphys3109> (visited on 01/11/2024).
- [17] Rovi Angelo B. Villaos et al. “Evolution of the Electronic Properties of ZrX<sub>2</sub> (X = S, Se, or Te) Thin Films under Varying Thickness”. en. In: *The Journal of Physical Chemistry C* 125.1 (Jan. 2021), pp. 1134–1142. ISSN: 1932-7447, 1932-7455. DOI: 10.1021/acs.jpcc.0c10085. URL: <https://pubs.acs.org/doi/10.1021/acs.jpcc.0c10085> (visited on 06/05/2023).



- [18] Bo Zhang et al. “Electronic Structures of Cr-Intercalated ZrTe<sub>2</sub> Revealed by Angle-Resolved Photoemission Spectroscopy”. In: *The Journal of Physical Chemistry C* 124.30 (July 30, 2020), pp. 16561–16567. ISSN: 1932-7447. DOI: 10.1021/acs.jpcc.0c04168. URL: <https://doi.org/10.1021/acs.jpcc.0c04168> (visited on 08/07/2021).
- [19] L. E. Correa et al. “Superconductivity in Te-deficient ZrTe<sub>2</sub>”. In: (2022). Publisher: arXiv Version Number: 1. DOI: 10.48550/ARXIV.2212.02358. URL: <https://arxiv.org/abs/2212.02358> (visited on 12/12/2022).
- [20] Yekai Song et al. “Signatures of excitonic insulating state in monolayer 1T-ZrTe<sub>2</sub>”. In: *arXiv:2201.11592 [cond-mat]* (Jan. 27, 2022). arXiv: 2201.11592. URL: <http://arxiv.org/abs/2201.11592> (visited on 03/24/2022).
- [21] *Private Communications*. In collab. with Machado, A. J. S; Correa, L. E.
- [22] Stuart Brown and George Grüner. “Charge and Spin Density Waves”. In: *Scientific American* 270.4 (Apr. 1994), pp. 50–56. ISSN: 0036-8733. DOI: 10.1038/scientificamerican0494-50. URL: <https://www.scientificamerican.com/article/charge-and-spin-density-waves> (visited on 08/08/2022).
- [23] R. E. Peierls. *Quantum Theory of Solids*. Oxford Classic Texts in the Physical Sciences. Oxford, New York: Oxford University Press, Apr. 5, 2001. 240 pp. ISBN: 978-0-19-850781-9.
- [24] Michael Fowler. “The Peierls Transition: an unexpected insulator”. In: *Michael Fowler’s Lecture Notes Online*. University of Virginia Physics. URL: <http://galileo.phys.virginia.edu/~mfli/home.html> (visited on 06/23/2023).
- [25] P Aebi et al. “On the search for Fermi surface nesting in quasi-2D materials”. In: *Journal of Electron Spectroscopy and Related Phenomena* 117-118 (June 2001), pp. 433–449. ISSN: 03682048. DOI: 10.1016/S0368-2048(01)00262-6. URL: <https://linkinghub.elsevier.com/retrieve/pii/S0368204801002626> (visited on 08/08/2022).
- [26] Xuetao Zhu et al. “Misconceptions associated with the origin of charge density waves”. In: *Advances in Physics-X* 2.3 (2017). WOS:000418770700009, pp. 622–640. ISSN: 2374-6149. DOI: 10.1080/23746149.2017.1343098.
- [27] K. Rossnagel. “On the origin of charge-density waves in select layered transition-metal dichalcogenides”. In: *Journal of Physics: Condensed Matter* 23.21 (May 11, 2011). Publisher: IOP Publishing, p. 213001. ISSN: 0953-8984. DOI: 10.1088/0953-8984/23/21/213001. URL: <https://iopscience.iop.org/article/10.1088/0953-8984/23/21/213001/meta> (visited on 03/24/2022).
- [28] J. Frenkel. “On the Transformation of light into Heat in Solids. I”. In: *Phys. Rev.* 37 (1 Jan. 1931), pp. 17–44. DOI: 10.1103/PhysRev.37.17. URL: <https://link.aps.org/doi/10.1103/PhysRev.37.17>.

- [29] Gregory H. Wannier. “The Structure of Electronic Excitation Levels in Insulating Crystals”. In: *Phys. Rev.* 52 (3 Aug. 1937), pp. 191–197. DOI: 10.1103/PhysRev.52.191. URL: <https://link.aps.org/doi/10.1103/PhysRev.52.191>.
- [30] N. F. Mott. “The Transition to the Metallic State”. In: *Philosophical Magazine* 6.62 (1961), pp. 287–309. DOI: 10.1080/14786436108243318.
- [31] R. S. Knox. “Introduction to Exciton Physics”. In: *Collective Excitations in Solids*. Ed. by Baldassare Di Bartolo. NATO Advanced Science Institute Series. Boston, MA: Springer US, 1983, pp. 183–245. ISBN: 978-1-4684-8878-4. DOI: 10.1007/978-1-4684-8878-4\_5. URL: [https://doi.org/10.1007/978-1-4684-8878-4\\_5](https://doi.org/10.1007/978-1-4684-8878-4_5) (visited on 09/04/2023).
- [32] Vitor M. Pereira. “Topological excitons”. In: *Nature Physics* 18.1 (Jan. 2022). Number: 1 Publisher: Nature Publishing Group, pp. 6–7. ISSN: 1745-2481. DOI: 10.1038/s41567-021-01466-y. URL: <https://www.nature.com/articles/s41567-021-01466-y> (visited on 07/03/2023).
- [33] Yanyu Jia et al. “Evidence for a monolayer excitonic insulator”. In: *Nature Physics* 18.1 (Jan. 2022). Number: 1 Publisher: Nature Publishing Group, pp. 87–93. ISSN: 1745-2481. DOI: 10.1038/s41567-021-01422-w. URL: <https://www.nature.com/articles/s41567-021-01422-w> (visited on 09/05/2023).
- [34] Bosong Sun et al. “Evidence for equilibrium exciton condensation in monolayer WTe<sub>2</sub>”. In: *Nature Physics* 18.1 (Jan. 2022). Number: 1 Publisher: Nature Publishing Group, pp. 94–99. ISSN: 1745-2481. DOI: 10.1038/s41567-021-01427-5. URL: <https://www.nature.com/articles/s41567-021-01427-5> (visited on 09/05/2023).
- [35] H. Cercellier et al. “Evidence for an excitonic insulator phase in 1T-TiSe<sub>2</sub>”. In: *PHYSICAL REVIEW LETTERS* 99.14 (Oct. 5, 2007). ISSN: 0031-9007. DOI: 10.1103/PhysRevLett.99.146403.
- [36] Thomas Mueller and Ermin Malic. “Exciton physics and device application of two-dimensional transition metal dichalcogenide semiconductors”. In: *npj 2D Materials and Applications* 2.1 (Sept. 10, 2018), p. 29. ISSN: 2397-7132. DOI: 10.1038/s41699-018-0074-2. URL: <https://doi.org/10.1038/s41699-018-0074-2>.
- [37] J.A. Wilson, F.J. Di Salvo, and S. Mahajan. “Charge-density waves and superlattices in the metallic layered transition metal dichalcogenides”. In: *Advances in Physics* 24.2 (Mar. 1, 1975). Publisher: Taylor & Francis \_eprint: <https://doi.org/10.1080/00018737500101391>, pp. 117–201. ISSN: 0001-8732. DOI: 10.1080/00018737500101391. URL: <https://doi.org/10.1080/00018737500101391> (visited on 07/04/2023).

- [38] R. Brouwer and F. Jellinek. “The low-temperature superstructures of 1T-TaSe<sub>2</sub> and 2H-TaSe<sub>2</sub>”. In: *Physica B+C* 99.1 (Jan. 1, 1980), pp. 51–55. ISSN: 0378-4363. DOI: 10.1016/0378-4363(80)90209-0. URL: <https://www.sciencedirect.com/science/article/pii/0378436380902090> (visited on 07/04/2023).
- [39] F. J. Di Salvo, D. E. Moncton, and J. V. Waszczak. “Electronic properties and superlattice formation in the semimetal TiSe<sub>2</sub>”. In: *Physical Review B* 14.10 (Nov. 15, 1976), pp. 4321–4328. ISSN: 0556-2805. DOI: 10.1103/PhysRevB.14.4321. URL: <https://link.aps.org/doi/10.1103/PhysRevB.14.4321> (visited on 07/04/2023).
- [40] Qiang Gao et al. “Evidence of high-temperature exciton condensation in a two-dimensional semimetal”. In: *Nature Communications* 14.1 (Feb. 22, 2023), p. 994. ISSN: 2041-1723. DOI: 10.1038/s41467-023-36667-x. arXiv: 2302.03876 [cond-mat]. URL: <http://arxiv.org/abs/2302.03876> (visited on 11/10/2023).
- [41] Keita Kobayashi et al. “Superconductivity in repulsively interacting fermions on a diamond chain: Flat-band-induced pairing”. In: *Physical Review B* 94.21 (Dec. 1, 2016). Publisher: American Physical Society, p. 214501. DOI: 10.1103/PhysRevB.94.214501. URL: <https://link.aps.org/doi/10.1103/PhysRevB.94.214501> (visited on 09/14/2023).
- [42] Rafael M. Fernandes. “Lecture Notes: BCS theory of superconductivity”. In: 2015. URL: <https://api.semanticscholar.org/CorpusID:84841081>.
- [43] Michael P. Marder. *Condensed Matter Physics: Marder/Condensed*. Hoboken, NJ, USA: John Wiley & Sons, Inc., Oct. 25, 2010. ISBN: 978-0-470-94995-5 978-0-470-61798-4. DOI: 10.1002/9780470949955. URL: <http://doi.wiley.com/10.1002/9780470949955> (visited on 09/13/2022).
- [44] V. I. Iglovikov et al. “Superconducting transitions in flat-band systems”. In: *Physical Review B* 90.9 (Sept. 11, 2014). Publisher: American Physical Society, p. 094506. DOI: 10.1103/PhysRevB.90.094506. URL: <https://link.aps.org/doi/10.1103/PhysRevB.90.094506> (visited on 04/05/2023).
- [45] Hideo Aoki. “Theoretical Possibilities for Flat Band Superconductivity”. In: *Journal of Superconductivity and Novel Magnetism* 33 (Aug. 1, 2020). DOI: 10.1007/s10948-020-05474-6.
- [46] Zhiming Zhang et al. “Flat bands in twisted bilayer transition metal dichalcogenides”. In: *Nature Physics* 16.11 (Nov. 2020). Number: 11 Publisher: Nature Publishing Group, pp. 1093–1096. ISSN: 1745-2481. DOI: 10.1038/s41567-020-0958-x. URL: <https://www.nature.com/articles/s41567-020-0958-x> (visited on 04/12/2023).

- [47] Zhen Bi, Noah F. Q. Yuan, and Liang Fu. “Designing flat bands by strain”. In: *Physical Review B* 100.3 (July 31, 2019). Publisher: American Physical Society, p. 035448. DOI: 10.1103/PhysRevB.100.035448. URL: <https://link.aps.org/doi/10.1103/PhysRevB.100.035448> (visited on 04/13/2023).
- [48] Valerio Vitale et al. *Flat band properties of twisted transition metal dichalcogenide homo- and hetero-bilayers of MoS<sub>2</sub>, MoSe<sub>2</sub>, WS<sub>2</sub> and WSe<sub>2</sub>*. May 17, 2021. arXiv: 2102.03259 [cond-mat]. URL: <http://arxiv.org/abs/2102.03259> (visited on 06/07/2023).
- [49] Leon Balents et al. “Superconductivity and strong correlations in moiré flat bands”. In: *Nature Physics* 16.7 (July 2020). Number: 7 Publisher: Nature Publishing Group, pp. 725–733. ISSN: 1745-2481. DOI: 10.1038/s41567-020-0906-9. URL: <https://www.nature.com/articles/s41567-020-0906-9> (visited on 04/11/2023).
- [50] Yong Hu et al. “Topological surface states and flat bands in the kagome superconductor CsV<sub>3</sub>Sb<sub>5</sub>”. In: *Science Bulletin* 67.5 (Mar. 15, 2022), pp. 495–500. ISSN: 2095-9273. DOI: 10.1016/j.scib.2021.11.026. URL: <https://www.sciencedirect.com/science/article/pii/S2095927321007349> (visited on 04/10/2023).
- [51] Rustem Khasanov et al. *Emergence of flat bands and their impact on superconductivity of Mo<sub>5</sub>Si<sub>3-x</sub>P<sub>x</sub>*. May 28, 2023. arXiv: 2305.17669 [cond-mat]. URL: <http://arxiv.org/abs/2305.17669> (visited on 06/07/2023).
- [52] Andrea Damascelli, Zahid Hussain, and Zhi-Xun Shen. “Angle-resolved photoemission studies of the cuprate superconductors”. In: *Rev. Mod. Phys.* 75 (2 Apr. 2003), pp. 473–541. DOI: 10.1103/RevModPhys.75.473. URL: <https://link.aps.org/doi/10.1103/RevModPhys.75.473>.
- [53] C. N. Berglund and W. E. Spicer. “Photoemission Studies of Copper and Silver: Theory”. In: *Phys. Rev.* 136 (4A Nov. 1964), A1030–A1044. DOI: 10.1103/PhysRev.136.A1030. URL: <https://link.aps.org/doi/10.1103/PhysRev.136.A1030>.
- [54] Stefan Hüfner. *Photoelectron Spectroscopy*. Advanced Texts in Physics. Berlin, Heidelberg: Springer, 2003. ISBN: 978-3-642-07520-9 978-3-662-09280-4. DOI: 10.1007/978-3-662-09280-4. URL: <http://link.springer.com/10.1007/978-3-662-09280-4> (visited on 01/11/2024).
- [55] Andrea Damascelli, Zahid Hussain, and Zhi-Xun Shen. “Angle-resolved photoemission studies of the cuprate superconductors”. In: *Reviews of Modern Physics* 75.2 (Apr. 17, 2003). Publisher: American Physical Society, pp. 473–541. DOI: 10.1103/RevModPhys.75.473. URL: <https://link.aps.org/doi/10.1103/RevModPhys.75.473> (visited on 03/28/2022).
- [56] Danny Haberer. “Electronic Properties of Functionalized Graphene Studied With Photoemission Spectroscopy”. PhD thesis. Oct. 9, 2012.

- [57] Hongyun Zhang et al. “Angle-resolved Photoemission Spectroscopy”. In: ().
- [58] *Atomic orbital Molecular orbital Pi bond Principal quantum number Orbital hybridisation, others, angle, text, symmetry png | PNGWing*. URL: <https://www.pngwing.com/en/free-png-xejyf> (visited on 09/27/2023).
- [59] Kevin Raduenz Pakuszewski. “Investigação da estrutura eletrônica de materiais com estados topológicos complexos por meio de espectroscopia de fotoemissão resolvida em ângulo”. Doutorado em Física. Campinas: Universidade Estadual de Campinas, May 19, 2023. URL: <https://www.teses.usp.br/teses/disponiveis/43/43134/tde-03072023-080732/>.
- [60] Marli Dos Reis Cantarino. “Electronic structure and magnetic excitations of magnetic superconductors”. Doutorado em Física. São Paulo: Universidade de São Paulo, June 14, 2023. DOI: 10.11606/T.43.2023.tde-03072023-080732. URL: <https://www.teses.usp.br/teses/disponiveis/43/43134/tde-03072023-080732/> (visited on 09/06/2023).
- [61] R. Kurlito and J. Fink. “About two-dimensional fits for the analysis of the scattering rates and renormalization functions from angle-resolved photoelectron spectroscopy data”. In: *Journal of Electron Spectroscopy and Related Phenomena* 253 (Dec. 1, 2021), p. 147127. ISSN: 0368-2048. DOI: 10.1016/j.elspec.2021.147127. URL: <https://www.sciencedirect.com/science/article/pii/S0368204821000785> (visited on 11/06/2023).
- [62] Karl Hoffmann. *An Introduction to Measurements using Strain Gages*. Darmstadt: Hottinger Baldwin Messtechnik GmbH, 1989.
- [63] G. Binnig and H. Rohrer. “Scanning tunneling microscopy”. In: *Surface Science* 126.1 (Mar. 1983), pp. 236–244. ISSN: 00396028. DOI: 10.1016/0039-6028(83)90716-1. URL: <https://linkinghub.elsevier.com/retrieve/pii/0039602883907161> (visited on 09/12/2022).
- [64] *LAB UNIT 5: Scanning Tunneling Microscopy*. 2009.
- [65] Øystein Fischer et al. “Scanning tunneling spectroscopy of high-temperature superconductors”. In: *Reviews of Modern Physics* 79.1 (Mar. 13, 2007), pp. 353–419. ISSN: 0034-6861, 1539-0756. DOI: 10.1103/RevModPhys.79.353. URL: <https://link.aps.org/doi/10.1103/RevModPhys.79.353> (visited on 12/23/2022).
- [66] J. Tersoff and D. R. Hamann. “Theory and Application for the Scanning Tunneling Microscope”. In: *Physical Review Letters* 50.25 (June 20, 1983), pp. 1998–2001. ISSN: 0031-9007. DOI: 10.1103/PhysRevLett.50.1998. URL: <https://link.aps.org/doi/10.1103/PhysRevLett.50.1998> (visited on 01/10/2023).
- [67] R. S. Markiewicz. “VAN HOVE SINGULARITIES AND HIGH-T<sub>c</sub> SUPERCONDUCTIVITY: A REVIEW”. In: *International Journal of Modern Physics B* 05.12 (July 20, 1991), pp. 2037–2071. ISSN: 0217-9792, 1793-6578. DOI: 10.1142/S0217979291000791. URL: <https://www.worldscientific.com/doi/abs/10.1142/S0217979291000791> (visited on 09/14/2022).

- [68] M. Kavitha and Manu Jaiswal. “Graphene : A review of optical properties and photonic applications”. In: 2016.
- [69] Si-Yu Li et al. *Evidence of electron-electron interactions around Van Hove singularities of a graphene Moiré superlattice*. May 9, 2017. arXiv: 1702.03501 [cond-mat]. URL: <http://arxiv.org/abs/1702.03501> (visited on 09/19/2022).
- [70] R. Bistritzer and A. H. MacDonald. “Moire bands in twisted double-layer graphene”. In: *Proceedings of the National Academy of Sciences* 108.30 (July 26, 2011), pp. 12233–12237. ISSN: 0027-8424, 1091-6490. DOI: 10.1073/pnas.1108174108. arXiv: 1009.4203 [cond-mat]. URL: <http://arxiv.org/abs/1009.4203> (visited on 09/19/2022).
- [71] Nanosurf AG. *Nanosurf NaoSTM - Operating Instructions for Nao Control Software Version 3.6*. Switzerland, 2015.
- [72] Eva Y. Andrei, Guohong Li, and Xu Du. “Electronic properties of graphene: a perspective from scanning tunneling microscopy and magneto-transport”. In: *Reports on Progress in Physics* 75.5 (May 1, 2012), p. 056501. ISSN: 0034-4885, 1361-6633. DOI: 10.1088/0034-4885/75/5/056501. arXiv: 1204.4532 [cond-mat]. URL: <http://arxiv.org/abs/1204.4532> (visited on 11/17/2022).
- [73] Q Dubout et al. “Giant apparent lattice distortions in STM images of corrugated  $sp^2$ -hybridised monolayers”. In: *New Journal of Physics* 18.10 (Oct. 19, 2016), p. 103027. ISSN: 1367-2630. DOI: 10.1088/1367-2630/18/10/103027. URL: <https://iopscience.iop.org/article/10.1088/1367-2630/18/10/103027> (visited on 12/06/2022).
- [74] Zheyong Fan et al. “Bimodal Grain-Size Scaling of Thermal Transport in Polycrystalline Graphene from Large-Scale Molecular Dynamics Simulations”. In: *Nano letters* 17 (Sept. 2017). DOI: 10.1021/acs.nanolett.7b01742.
- [75] I. Brihuega et al. “Unraveling the Intrinsic and Robust Nature of van Hove Singularities in Twisted Bilayer Graphene by Scanning Tunneling Microscopy and Theoretical Analysis”. In: *Physical Review Letters* 109.19 (Nov. 8, 2012), p. 196802. ISSN: 0031-9007, 1079-7114. DOI: 10.1103/PhysRevLett.109.196802. URL: <https://link.aps.org/doi/10.1103/PhysRevLett.109.196802> (visited on 12/06/2022).

## **Appendix A**

# **Complementary Figures**

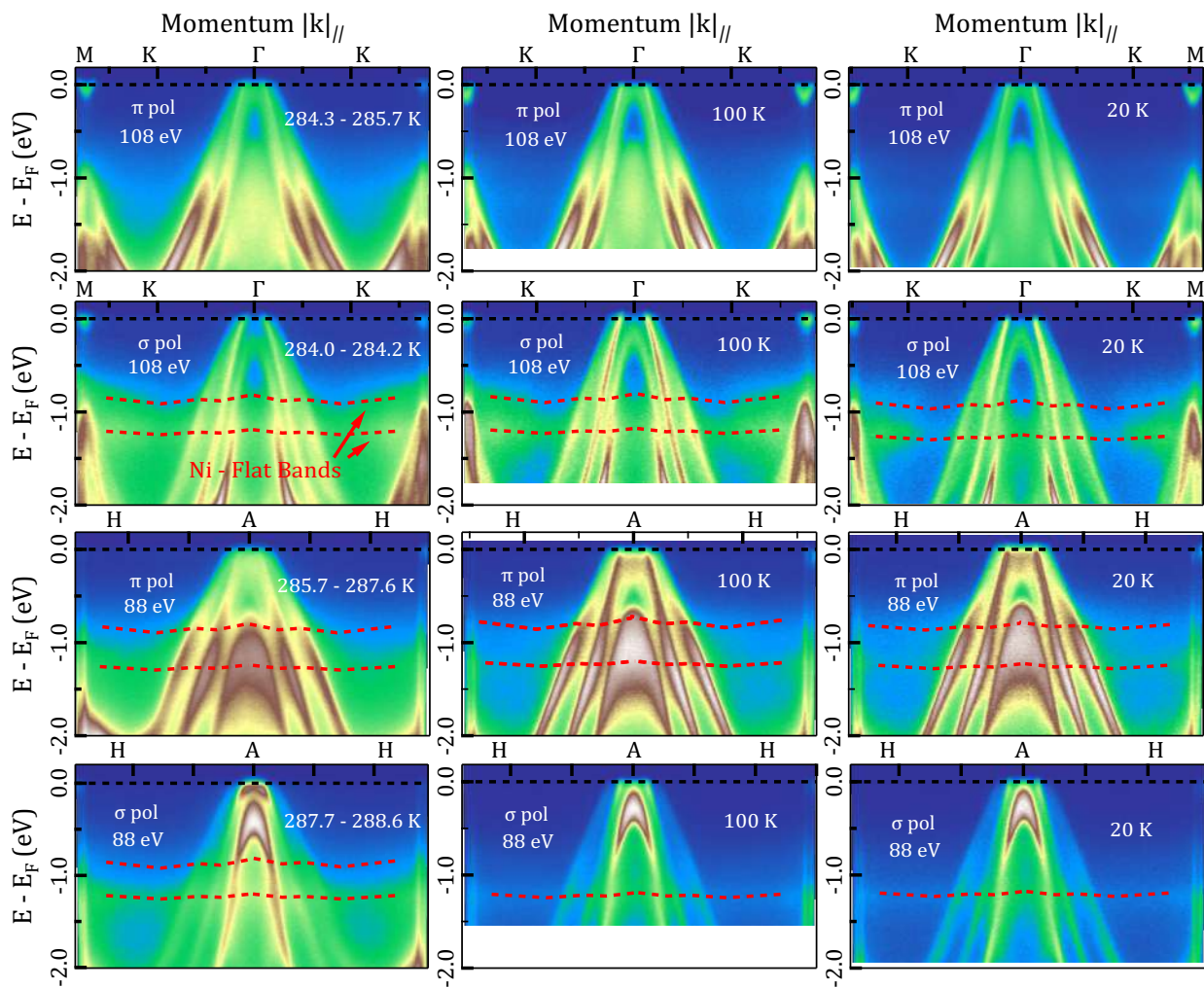


Figure A.1: ARPES measurements of  $\text{Ni}_{0.05}\text{ZrTe}_2$  energy maps for the  $\Gamma\text{K}$  high symmetry direction at both linear light polarization and incident photon energies of 88 and 108 eV.



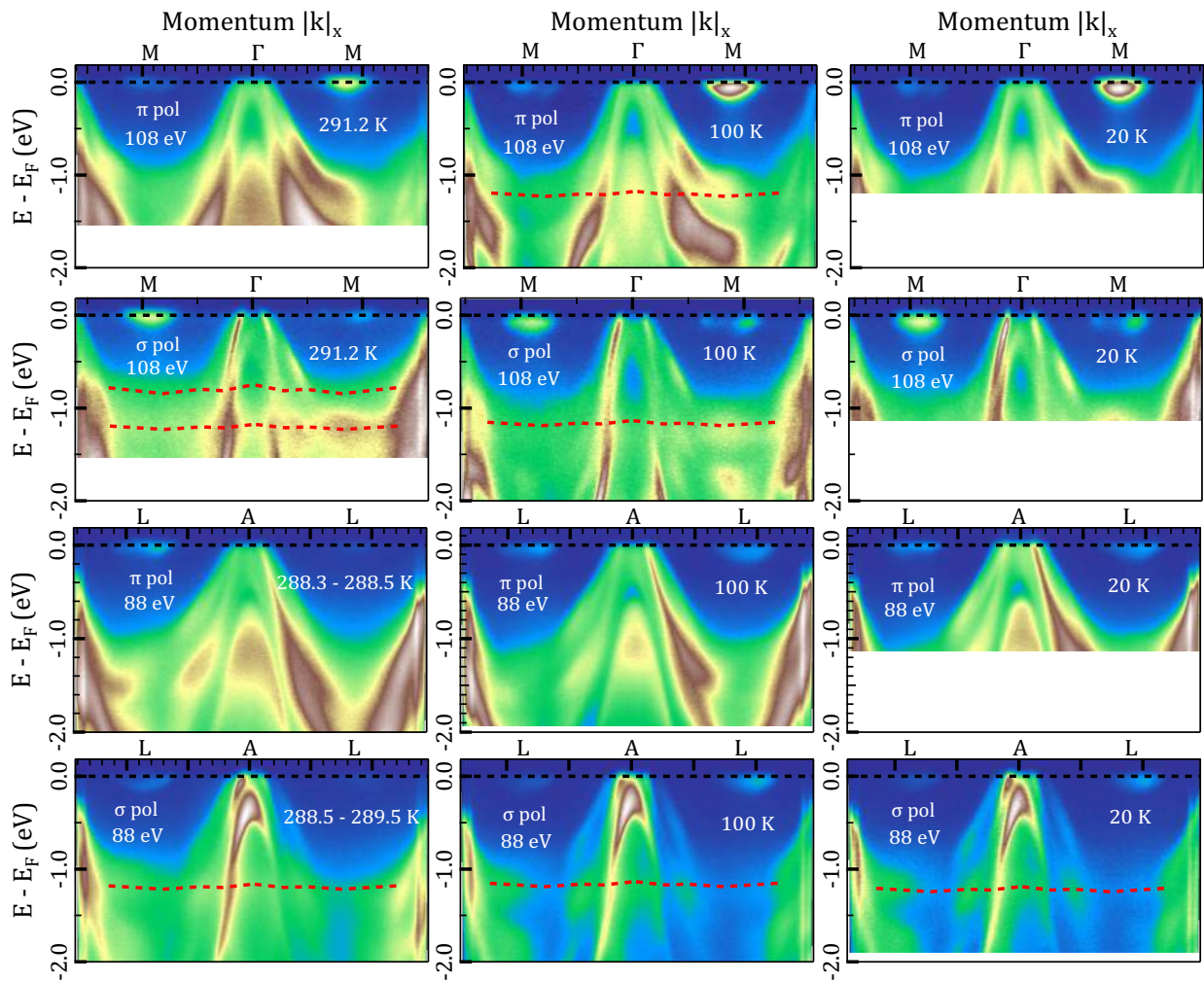


Figure A.2: ARPES measurements of  $\text{Ni}_{0.05}\text{ZrTe}_2$  energy maps for the  $\Gamma\text{M}$  high symmetry direction at both linear light polarization and incident photon energies of 88 and 108 eV.

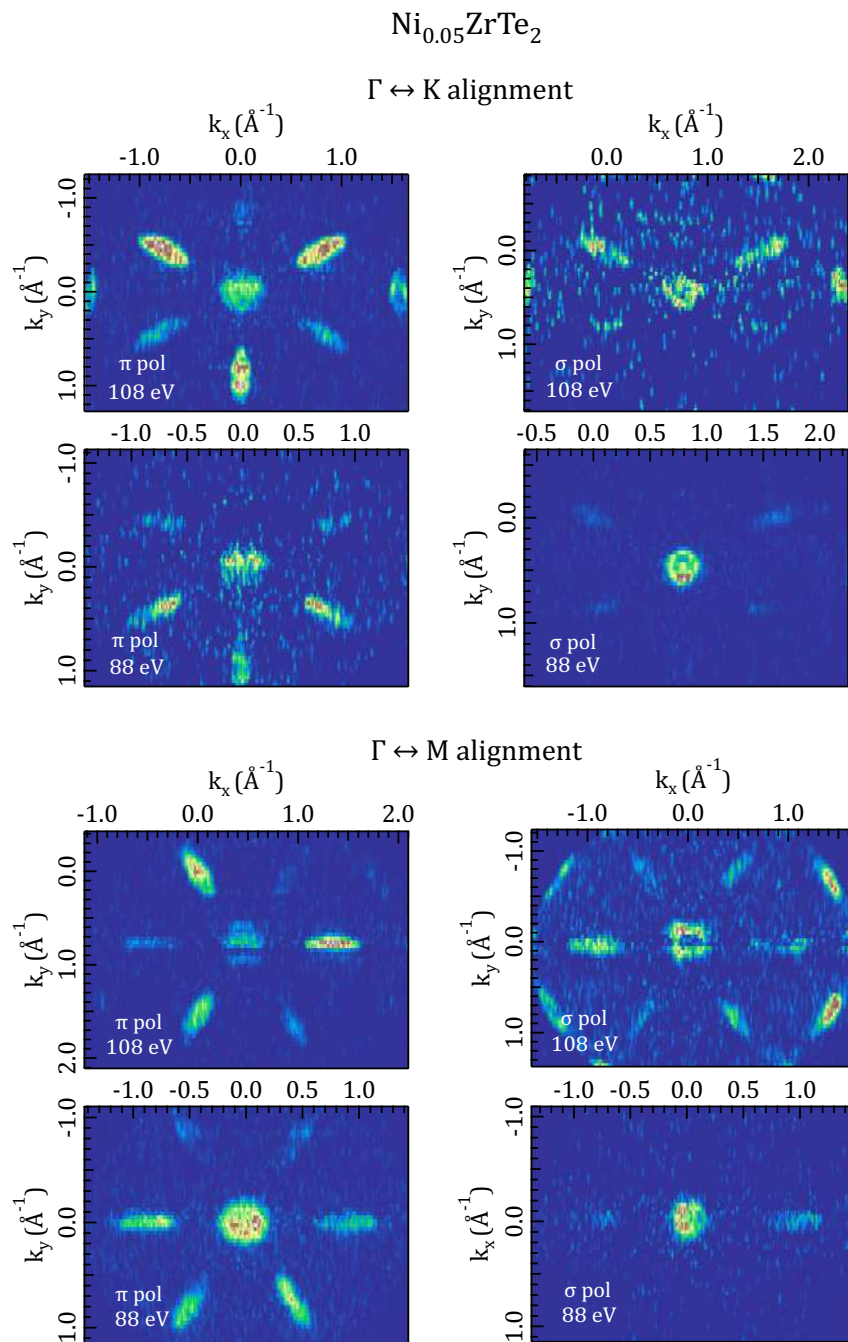


Figure A.3: ARPES measurements of  $\text{Ni}_{0.05}\text{ZrTe}_2$  Fermi Maps for both high symmetry direction at both linear light polarization.

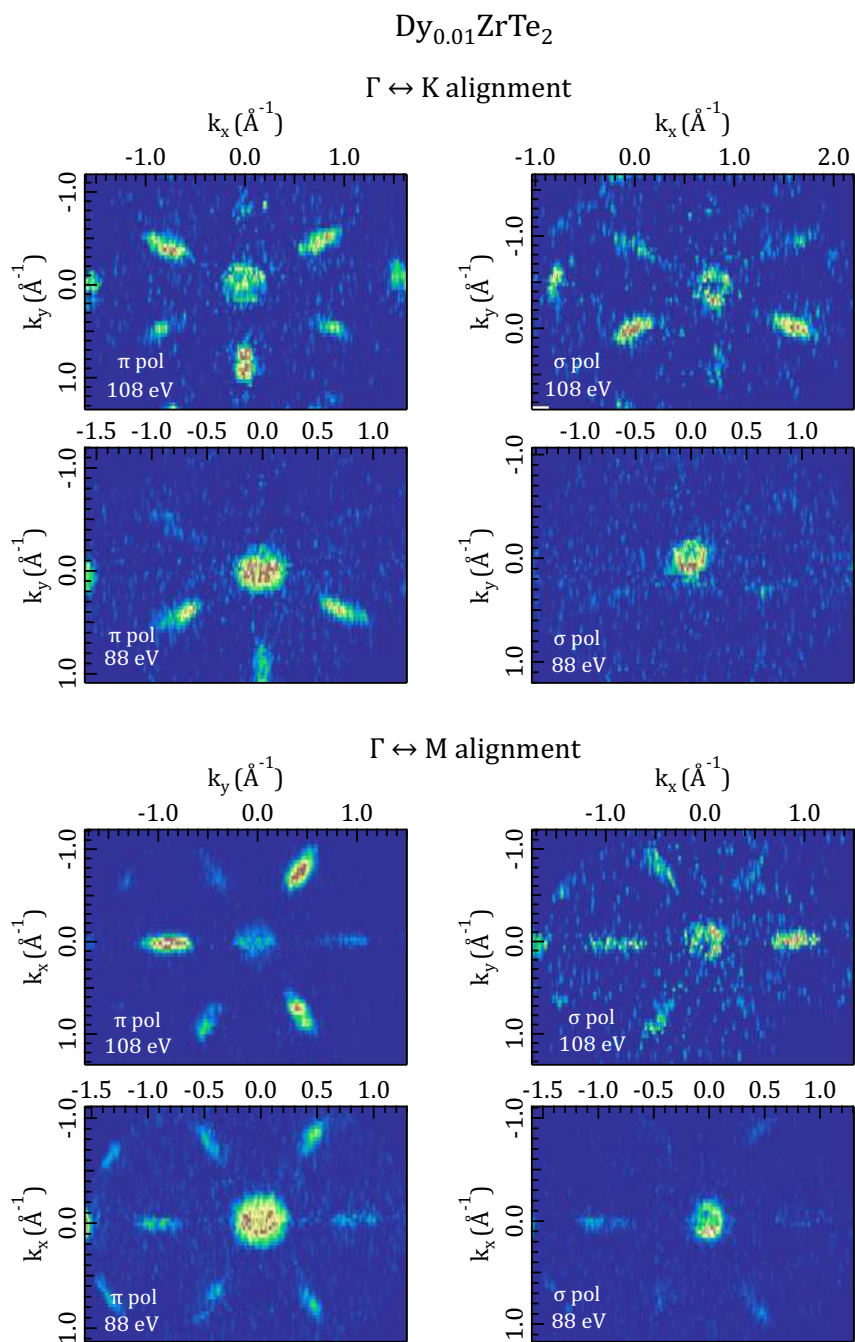


Figure A.4: ARPES measurements of  $\text{Dy}_{0.01}\text{ZrTe}_2$  Fermi Maps for both high symmetry direction at both linear light polarization.

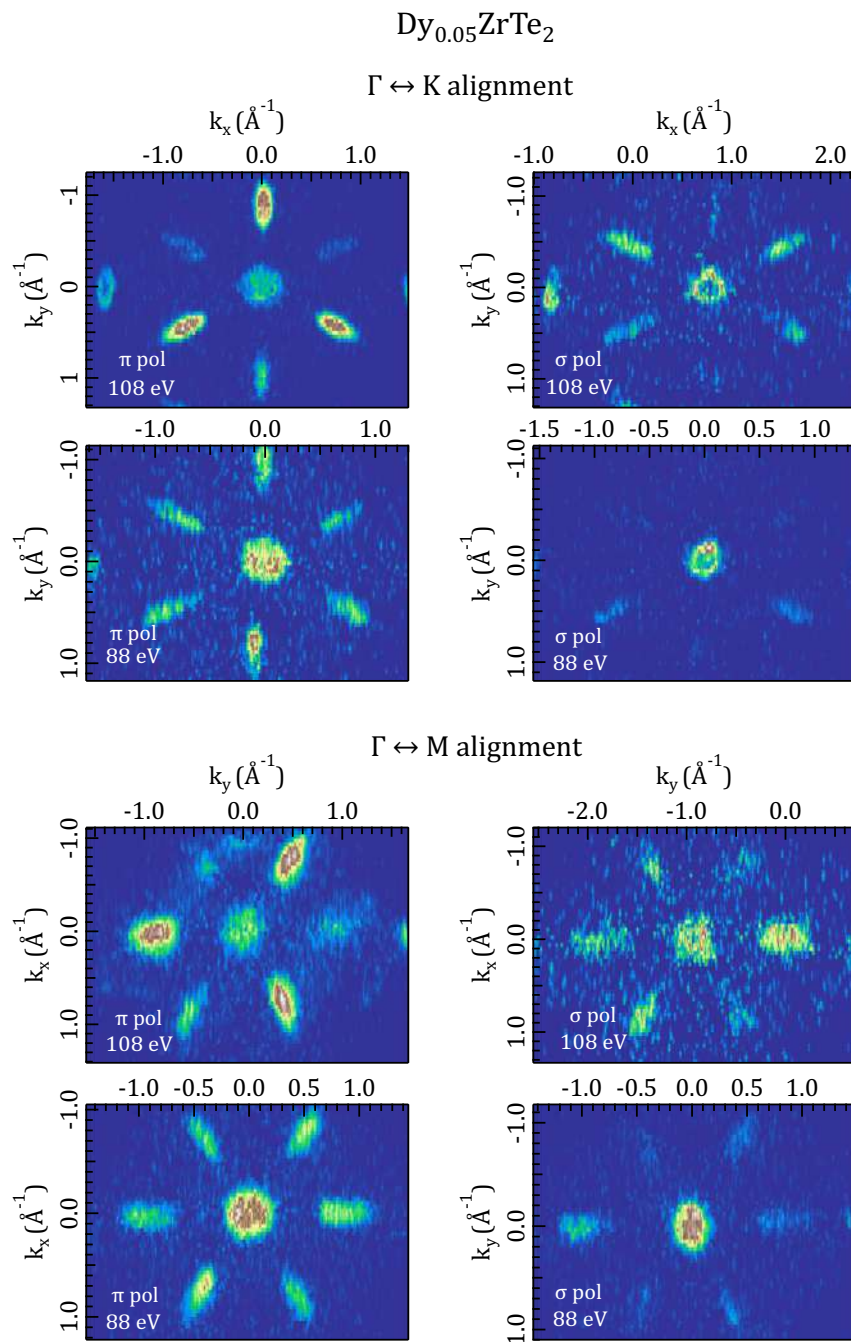


Figure A.5: ARPES measurements of  $\text{Dy}_{0.05}\text{ZrTe}_2$  Fermi Maps for both high symmetry direction at both linear light polarization.

## Appendix B

# Strain Device Project

Strain is a very well-known mechanical property in materials science which represents the relative displacement of particles in a rigid system compared to a length of reference, usually from the relaxed system. It is a very fundamental property of solid state physics, relevant for technological applications, from the proper engineering of large structures employing concrete, steel and other materials to the fine design of electronic devices. However, controlling other properties of materials by means of an external applied strain, particularly for the field of quantum materials, is a rather unexplored territory which offers a lot of interesting possibilities. With the perspective of being able to perform experiments which measure properties of materials under the variation of the applied strain, our research group decided to build and characterize a strain device for future applications within the group's projects and collaborations.

So, in order to build such a device, we based our design on the one proposed by the group of Professor Dr. Claude Monney and his research group from the Department of Physics of the University of Fribourg. The device is shown in Figure B.1a. It is composed of basically three parts: a base plate that is a modified sample holder made of CuBe, which has holes for screws to be threaded; an CuBe bridge structure that is connected to the base plate by the screws is placed on top of the base structure; and an Al rectangular block with a rounded top which goes under the bridge. The height of the Al block is set to be slightly larger than the size from the surface of the base plate to the lower part of the CuBe-bridge. Thus, as the bridge is pushed against the Al block by the tightening of the screws, a strain is generated by the bending of the bridge forced by the presence of the Al block. It is important to say that the designed of the parts, particularly the base plate, were adapted in order to fit the dimensions of the ARPES setup that is currently being built on the SAPE beamline at the Laboratório Nacional de Luz Síncrotron (LNLS).

The next step is to characterize the strain magnitude somehow. This was done by using the commercial strain gauge 1-LM11-3/350GE (conferir o numero de serie) from Omega Engineering/HBM. For the strain gauge to actually measure the material's change in size, it was integrated to a home-built balanced Wheatstone bridge circuit in the so-called "quarter bridge configuration", as shown in Figure B.1b. The circuit can be divided into two parts. The first one is composed of two strain gauges with nominal resistance of 350 and

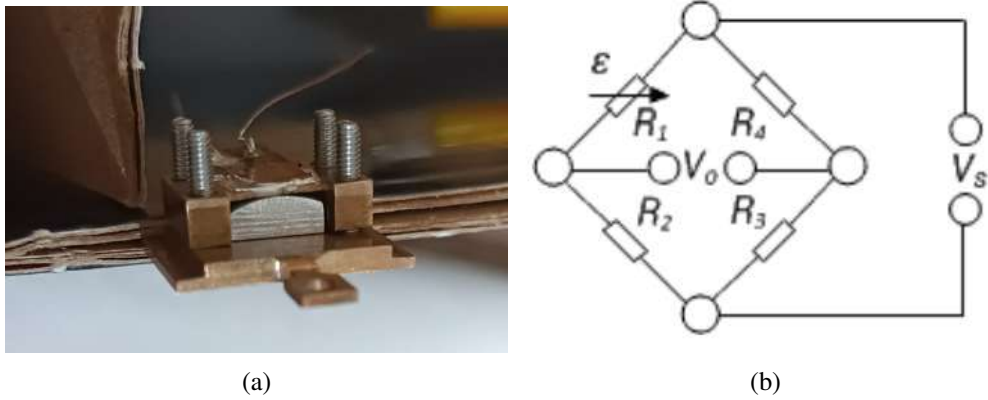


Figure B.1: (a): The strain device is composed of one CuBe base, where the screws are fixed, one CuBe bridge, on top of which the strain gauge is attached and the Al monoblock which generates the strain when the screws are tighten. (b): Wheatstone bridge configuration. The strain is measured by the increase/decrease of the output voltage  $V_0$ .

gauge factor  $k = 2.34\%$ , one of them is attached to an unstrained device and the other one is a passive gauge, which is not attached to any device, acting just as a simple resistor. The second part is consistent of two  $330 \Omega$  resistors. In order to balance the circuit a  $10 \Omega$  variable resistor was also used. Finally, a voltage of  $V_s = 5$  V from a source was applied. It is important to point out that for strain measurements in the Wheatstone bridge, the pair of resistances  $R_1/R_2$  and  $R_3/R_4$  must be equal.

Note that if the bridge is balanced,

$$\frac{R_1}{R_2} = \frac{R_3}{R_4}$$

and the bridge output will be zero. Then, with the presence of strain, the resistance of the strain gauge will change by some value  $\Delta R$ . This is expressed, after some algebraic development and proper approximations [62], as

$$\frac{V_0}{V_s} = \frac{1}{4} \left( \frac{\Delta R_1}{R_1} - \frac{\Delta R_2}{R_2} + \frac{\Delta R_3}{R_3} - \frac{\Delta R_4}{R_4} \right) \quad (\text{B.1})$$

where  $V_0$  is the measured voltage. The change in resistance translates into strain by the gauge factor  $k$ , as in following expression

$$\frac{\Delta R}{R} = k \cdot \epsilon \quad (\text{B.2})$$

which than give us

$$\frac{V_0}{V_s} = \frac{k}{4} (\epsilon_1 - \epsilon_2 + \epsilon_3 - \epsilon_4) \quad (\text{B.3})$$

Since the only actual resistance that changes is the one from the strain gauge, we can write the previous expression in the final form

$$\epsilon = \frac{4 V_0}{k V_s} \quad (\text{B.4})$$

The total strain  $\epsilon$  here can be divided into two components, the bending (tensile) strain and the perpendicular (compressive) strain. However, for this strain device configuration, the bending strain is much higher than the perpendicular component. For this reason when talking about the applied strain, we are always referring to the tensile component. The characterization of both components would only be possible by using additional strain gauges in such a way that is not feasible for this device geometry and size.

Finally, we were able to measure a change in the output voltage of about  $\Delta V \approx 1.20(15)\text{mV}$  upon completely tightening the screws. This converts into a strain of about  $\epsilon \approx 0.0406\%$ . This value was obtained after several cycles of tightening and releasing the screws. It is compatible with the measurements performed by the University of Fribourg's group, which found  $\epsilon \approx 0.05\%$ . Our device, thus, was able to generate a reasonable strain for applications which require only a very small strain on the sample.





## Appendix C

# Investigation of van Hove Singularities in BLG by STM and STS Techniques

### C.1 Scanning Tunneling Microscopy (STM)

The Scanning Tunneling Microscopy (STM) is one of the most common techniques employed to study the surface of materials, which allows the imaging of surface topographies in real space and work function profiles on an atomic scale [63]. The STM was developed by Gerd Binnig and Heinrich Rohrer, at IBM Zürich in 1981 and, since then, have been evolving and improving to become the standard technique in surface science.

The physical concept behind STM is the quantum tunneling effect, which allows particles to propagate through a potential barrier, usually imposed by the vacuum, but can be originated by other mediums as well. The essential idea of the experiment is, then, to approximate a very sharp metallic tip, ideally one with a single or just a few atoms at the end, close to a conducting surface, in a metal-insulator-metal configuration. When sufficiently close, a bias voltage is applied between them, which allows the electrons to tunnel through the potential barrier separating them, as shown in Figure C.1. This creates a tunneling current flowing from the surface to the tip (or vice-versa) [43, 2].

The tunneling current depends, thus, on many parameters. The most essential ones are the gap distance,  $z$ , between the tip and the sample surface, which causes an exponential decay on the transmission probability; the applied voltage,  $V_{bias}$ , and the density of states (DOS) of the sample at the Fermi level,  $\rho_s(E_F)$ . This leads to the following equation, within the Wentzel-Kramers-Brillouin (WKB) approximation [43, 64],

$$I \propto \rho_s(E_F) V_{bias} e^{-2d\sqrt{\frac{2m\phi}{\hbar^2}}} \quad (C.1)$$

where  $\hbar$  is Planck's constant,  $m$  is the electron mass,  $z$  is the gap distance and  $\phi$  is the average of the work functions of the tip and the surface.

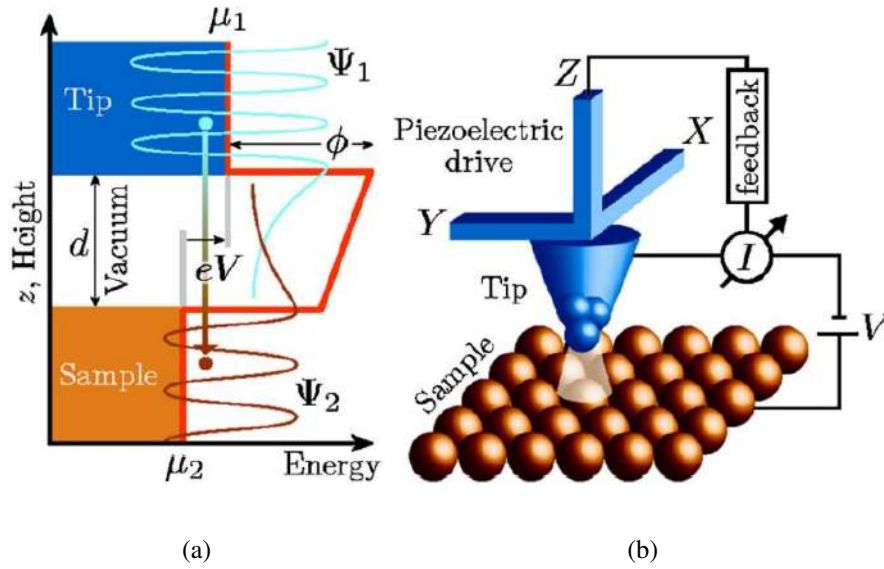


Figure C.1: (a): The diagram shows the physical working principle of STM. When the height  $z$  is small, the electron wave functions have a small overlap, which allows the tunneling from one part to the other. Applying a positive bias voltage  $V_{bias}$  to the sample causes the electrons to tunnel from the tip to the available states at the sample. (b): Schematics of the STM. Image from [65].

Finally, by measuring the current as the tip move across the surface, a 2D intensity color map of the surface topography is generated. An schematic of this process is presented also in Figure C.1. Since the tip is very sharp, it is remarkably responsive to the surface topography making possible the detection in atomic-scale variations in both horizontal and vertical directions.

## C.2 Scanning Tunneling Spectroscopy (STS)

Scanning Tunneling Spectroscopy (STS) is a very sophisticated application technique, which is possible due to the incredible resolution the STM instrumentation has. Here, the idea is to measure the tunneling current,  $I(V)$ , signal while modifying the bias voltage,  $V_{bias}$ , making sure the  $z$  parameter is constant. This way one can have access to a reconstruction of the electronic Local Density of States (LDOS) through the tunneling conductance  $\frac{dI}{dV}$  [65]. In this work, the tunneling conductance was obtained by directly differentiating the tunneling current  $I(V)$ .

To put it in a simple form, the correspondence between the tunneling conductance and sample DOS can be described by [65]

$$\frac{dI}{dV} \propto \int d\omega [-f'(\omega - eV)] \rho_{sample}(\mathbf{x}, \omega) \quad (\text{C.2})$$

where  $\mathbf{x}$  denotes the tip center of curvature,  $f'$  is the derivative of the Fermi function and  $\rho_{sample}(\mathbf{x}, \omega)$  is the LDOS. Therefore, STS data can be interpreted as a measurement of the thermally smeared LDOS of

the sample at the position of the tip.

However, it is more illustrative to consider the case of experiments which are performed at room temperature or below and at small voltage in the metal-insulator-metal tunneling. Within these limits, we can write the tunneling current as [66]

$$I = \frac{2\pi}{\hbar} e^2 V \sum_{\mu\nu} |M_{\mu\nu}|^2 \delta(E_\mu - E_F) \delta(E_\nu - E_F) \quad (\text{C.3})$$

Then, by calculating the tunneling matrix element  $M_{\mu\nu}$  as in [66], considering that the tip can be described by a spherical shape we get

$$I = 32\pi^3 \hbar^{-1} e^2 V \phi^2 D_t(E_F) R^2 k^{-4} e^{2kR} \times \sum_{\nu} |\Psi_{\nu}(\vec{r}_0)|^2 \delta(E_{\nu} - E_F) \quad (\text{C.4})$$

where  $\rho_{sample}(\vec{r}_0; E_F) = \sum_{\nu} |\Psi_{\nu}(\vec{r}_0)|^2 \delta(E_{\nu} - E_F)$  is the desired local density of states,  $R$  is the radius of the tip and  $k = \frac{\sqrt{2m\phi}}{\hbar}$ . Thus, by substituting common values for metals into equation C.4, we finally obtain the tunneling conductance as [66]

$$\frac{dI}{dV} \approx 0.1 R^2 e^{2kR} \rho(\vec{r}_0; E_F) \quad (\text{C.5})$$

Here, distances are given in atomic units and energy in electron volts. If we remember that  $|\Psi_{\nu}(\vec{r}_0)|^2 \propto e^{2k(R+d)}$ , we recover the proportionality relation in expression C.1.

### C.3 van Hove singularities (vHs)

The density of states (DOS) of a system influences many properties of interest in materials, specially when considering the surroundings of the Fermi level. The increase in DOS at this region enhance electronic correlations, resulting in different ordering instabilities, such as density waves and superconductivity at low temperatures. Therefore, it is of great importance and interest to be able to tune this property. One of the most widely studied topic regarding this aspect of emergent correlated phenomena is the van Hove singularities.

A van Hove singularity is a critical point, either a local maximum, minimum or a saddle point, in the electronic energy dispersion relation [67]. This feature in the electronic band structure has a very particular property of generating a singularity in the density of states of the system. In order to understand how the DOS may be affected by the vHs, one can write down the expression for the density of states as

$$D(E) = \frac{2}{(2\pi)^d} \int_{S(E)} \frac{dS}{|\nabla_{\vec{k}} E(\vec{k})|}. \quad (\text{C.6})$$

The integral in equation C.6 is carried over of the surface of constant energy  $S(E)$ , where  $E(\vec{k})$  is the energy dispersion relation and  $d$  is the dimensionality of the system [43]. We see, then, that the density of states will present a singularity when the electron velocity,  $\vec{v}_k$ , becomes zero, since it is proportional to the

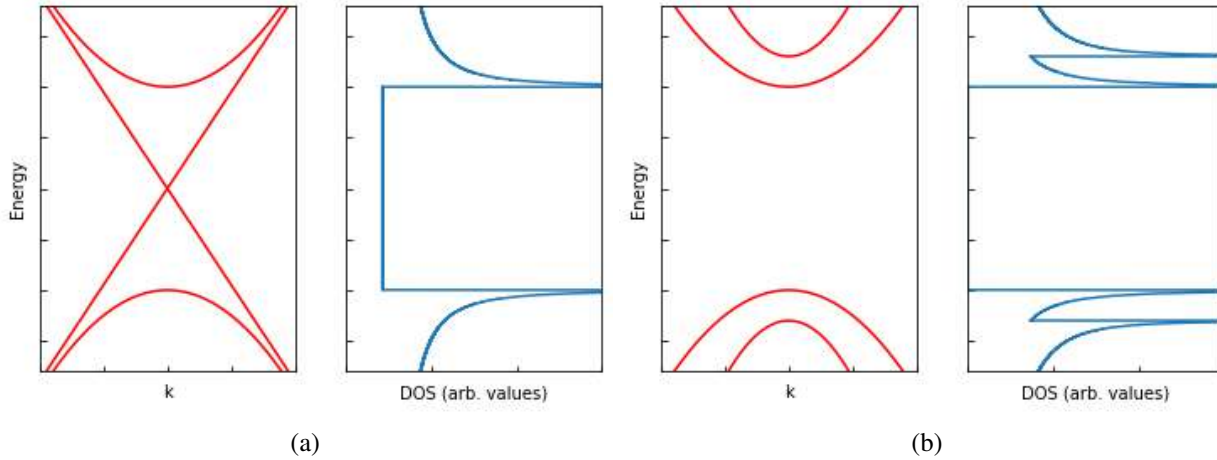


Figure C.2: Calculation of the density of states for a 1D system, which electronic band structure is composed of a linear and quadratic dispersion close to the Fermi level. The closer we are from the minimum and maximum of the dispersion, the higher is the density of states, until there is a jump - or singularity.

energy gradient - that means where the band structure has a local maximum, a local minimum or a saddle point, as long as the integral doesn't goes to zero faster than the inverse gradient diverges. Figure C.2 shows a qualitative example of the appearance of vHs in a one dimensional system with linear (Dirac Cone-like) and parabolic (free electron-like) band dispersion.

### C.3.1 vHs on Twisted Bilayer Graphene (TBG) and the Moiré effect

Graphene is a two dimensional system of carbon atoms arranged in a honeycomb lattice. The graphene monolayer is held together by  $\sigma$ -bonding between the three nearest neighbours of each atom in the system, formed by  $sp^2$  hybridized orbitals. Beyond the strong in-plane bonding, the electrical and optical properties are determined by the  $\pi$ -bond formed by un-hybridized p-orbitals of neighboring carbon atoms [68]. Figure C.3 presents the graphene monolayer system. This configuration yields a semimetal with very unique electronic, thermal, optical, magnetic and mechanical properties.

One of the most studied characteristic of the graphene properties is related to its linear energy dispersion in the electronic band structure. At point K of the reciprocal space, the valence and conduction bands touch each other, forming a so called Dirac cone. This also makes graphene be classified as a semimetal, since the DOS in the Fermi level is also reasonably small. Around this cone, the energy dispersion relation is linear, rather than quadratic, in  $\vec{k}$ , which means that electron transport can be essentially described by the Dirac equation, where the charge carries are effectively massless [9].

Beyond that, an adjacent system which has attracted great attention of the community in the past few years is the Twisted Bilayer Graphene (TBG), which is composed of two layers of graphene on top of each other slightly mismatched by a characteristic twist angle  $\theta$ . This relative twist between the two stacked honeycomb patterns causes the formation of a so called Moiré pattern, as shown in figure C.4. The twist

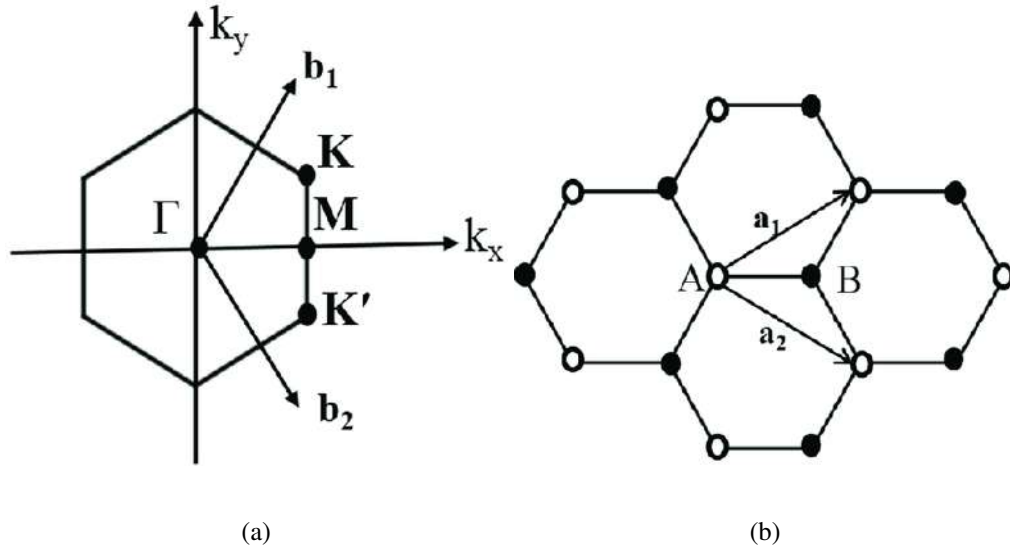


Figure C.3: (a) Honeycomb structure of graphene. Note that the Bravais lattice is actually a triangular lattice with an atomic basis given by carbon atoms represented by A and B. The lattice vectors are given by  $a_1$  and  $a_2$ . (b) Corresponding Brillouin Zone of the system, displaying the high-symmetry points and reciprocal lattice vectors. Images from [68].

angle  $\theta$  is related to the new period  $L$ , originated by the Moiré superlattice, by the expression

$$L = \frac{a}{2 \sin \frac{\theta}{2}} \quad (\text{C.7})$$

with  $a = 0.246$  nm the graphene lattice constant [69].

One of the most interesting aspects about the formation of such pattern is that in the low twist angle regime, the inter-layer coupling becomes more strong and the electron velocity at Dirac point goes to zero, originating two low-energy saddle points in the band structures, which induces vHs in the density of states of the system [70]. At a certain angle, the dispersion of the bands at the Fermi Level become completely flat, which causes huge vHs. Tuning the vHs to the Fermi level cause the electron-electron interactions to increase, which allows for a range of new and interesting correlated states in graphene [69].

## C.4 STM/STS Experimental Setup and Measurements

In order to accomplish the proposed measurements, the Nanosurf NaoSTM was used. It is a compact kit for room temperature and atmospheric conditions measurements. The system is connected to a computer, where the apparatus is controlled. The experiments were performed according to the company's manual of instruction [71].

First, the sample must be attached to a metallic cylindrical sample holder, which allows the system to move the sample's surface further or closer to the tip. Then, a fine approximation is made automatically by

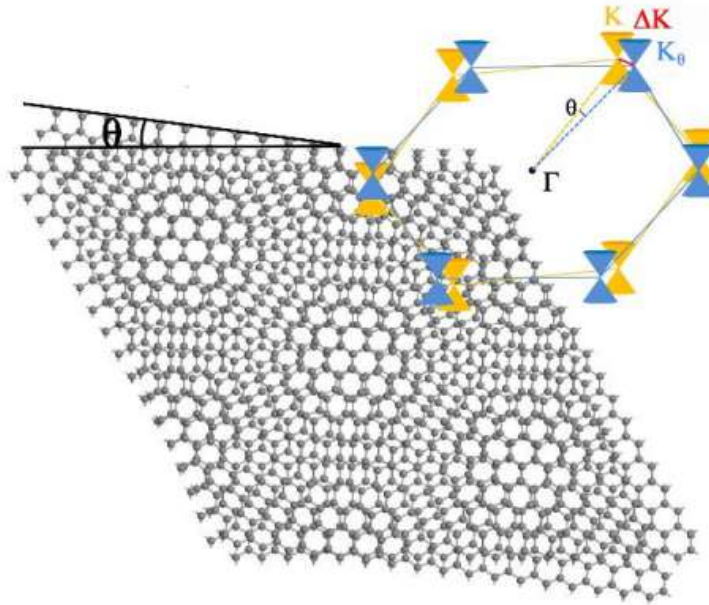


Figure C.4: Schematic of two mismatched graphene sheets by a twist angle  $\theta$ . It is possible to see the formation of a Moiré pattern, which gives the system a new periodicity. The inset shows the intersection of the two Dirac points of the two layers at  $K$  and  $K_\theta$  in momentum space. Image from [69].

a built-in routine that executes small steps iterations, the sample holder moves the sample over the tip. The process continues until the tunneling current reaches a defined threshold, after then the scan on the  $xy$  surface sample plane begins. The high precision movement of the tip through the surface is achieved by applying a voltage to the three mutually perpendicular piezoelectric transducers, making them expand or contract. A schematic of the piezodriven and the surface scanning process is shown in Figure C.5a

Finally, as the tip moves, the measured tunneling current changes according to the surface's topography, due to the atomic structure of the material. The  $z$ -piezo retracts the tip from the sample when the measured current is above a certain reference value (which was set as 1 nA, as suggested by [71]), and *vice-versa*. A set of equilibrium  $z$  positions is then generated from which a contour plot of the position-dependent tunneling current is obtained. This is the so called constant current operational mode and all STM images in this report were collected in this mode.

There is a second operating mode of the STM, the constant height mode. In this procedure, the tunneling current is measured as the tip scans the surface at a constant height. As well as the previous method, a map of the intensity of the current over the "xy" plane is then generated. This mode allows for a quicker surface sweep, although it has the disadvantage that the tip might crash into the sample with there is some misalignment between the plan of the tip scan and the surface or if the material topography is not so regular.

For the voltage spectroscopy measurements, each set contained 256 or 512 data points (chosen according to the experimental conditions of each measurement), taken as an average of different region over a prede-

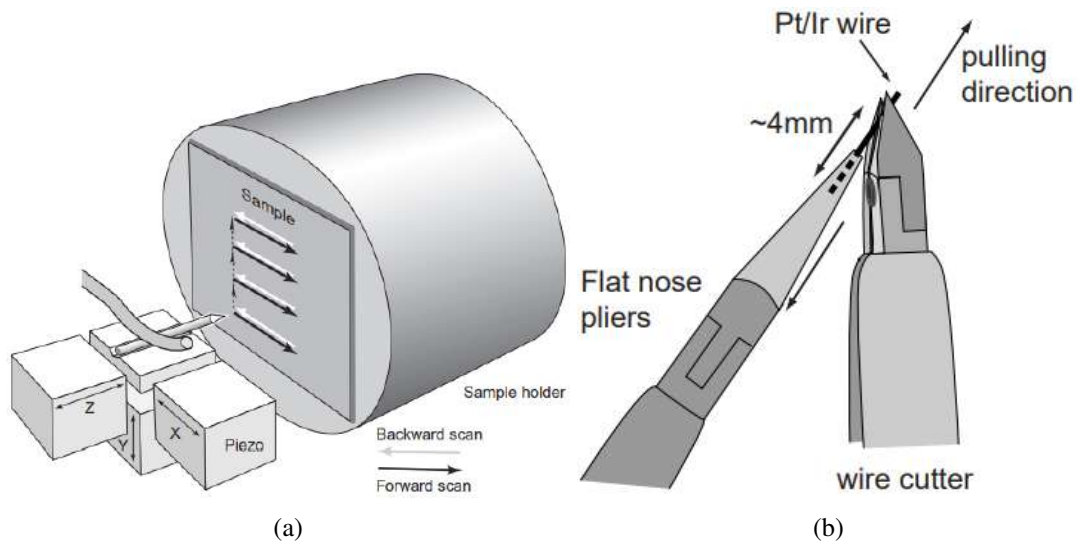


Figure C.5: Schematic of the scanning process (a) and tip crafting (b). Images from [71].

fined area, within different bias voltage ranges, as seen in the graphs presented in section C.5.

#### C.4.1 Measurements Quality Factors and Preparation

When performing the STM and STS experiments, the quality of measurements is influenced by three major factors: interfering signals, tip sharpness and sample's surface morphology and purity.

Regarding the interfering signals, the most common sources are mechanical vibrations and electrical fields. To avoid mechanical vibrations, the whole experimental setup was placed on a shock absorption table, on top of the already built-in vibrational isolation system of the NaoSTM. Once the tunneling current was established, external electromagnetic interference was diminished by covering the STM system with an metallic cover which worked as a Faraday box. Figure C.6 shows the STM setup used for the experiments and the metallic cover.

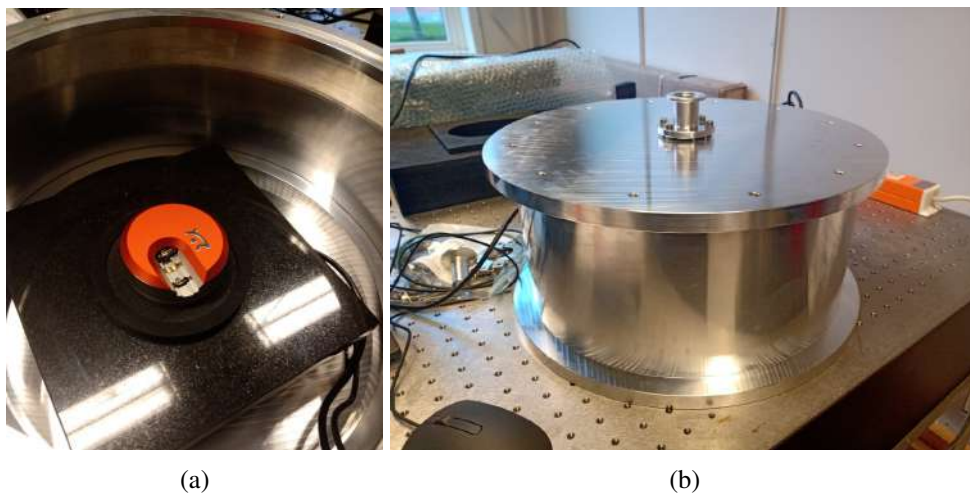


Figure C.6: (a): Picture of the STM setup used for the experiments. (b): Picture of the metallic cover installed in order to reduce interfering electromagnetic signals

Another very important interfering factor is the non-vacuum experimental environment. The atmospheric conditions of the measurements intrinsically introduces oxygen and water molecules which may be stuck in the sample surface or the tip, causing disturbances in the tunneling current.

The most difficult stage of the measurements preparation is the tip manufacturing process. The tip is cut from a Pt-Ir alloy wire and placed in a single conducting clamp. It required some practice to both cut as obliquely as possible by tearing off the tip from the wire and manipulating it with tweezers, as shown in Figure C.5. In order to avoid contaminating the sample and the STM components, gloves were used during any manipulation process and all tools were always cleaned beforehand with isopropanol.

Considering all the preparations steps, learning curve and the intrinsic difficulty related to ambient atmospheric conditions and room temperature type-of-measurements, it would typically take many attempts in order to get good images and spectroscopy data. Overall, one month and two weeks of the project designated time were dedicated entirely to the experimental data acquisition.

#### C.4.2 The Substrate Effect - Graphene on $\text{SiO}_2$

The samples probed in this work were all composed of graphene (mono and bilayer) deposited on  $\text{SiO}_2$ , which is an insulating substrate. It is well established that this type of substrates generate a random potential, which causes an inhomogeneous local charging, leading to electron/hole concentrated regions around the Dirac point [72]. This means that the zero carrier density at the Fermi Level cannot be realized, as schematically shown in the left of Figure C.7



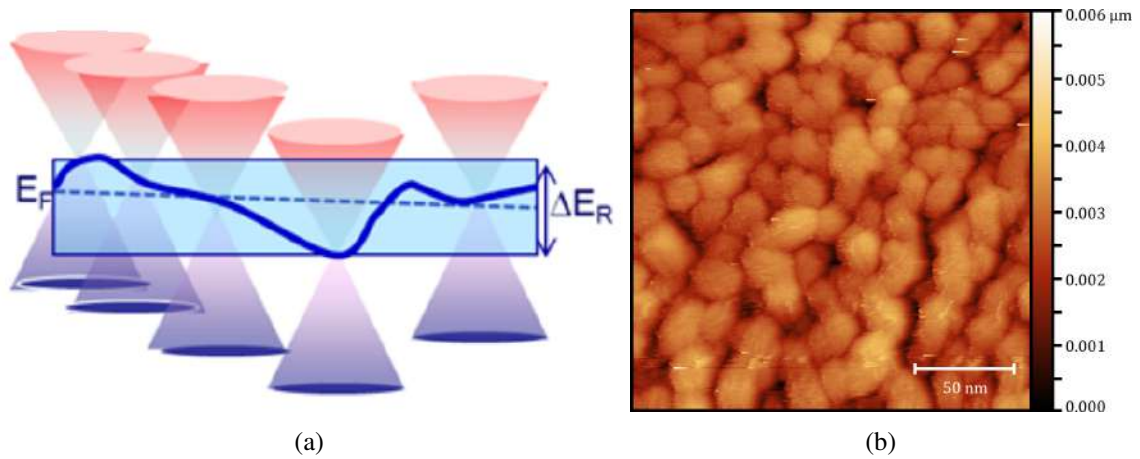


Figure C.7: (a): Schematic view on the Fermi Level shift due to the random potential in the sample Image from [72]. (b): Wide 200 nm x 200 nm view of the graphene surface deposited on  $\text{SiO}_2$  substrate.

Also graphene on  $\text{SiO}_2$  presents noticeable corrugations, which can range from large-scale ( $\approx 30$  nm) to smaller ( $\approx 15$  nm) associated to the  $\text{SiO}_2$  rough surface and to free standing graphene portions [72], as shown in the left of Figure C.7. A third type of corrugations, the formation of wrinkles, is also likely to occur due to the deposition process. This can cause a strong perturbation which breaks the graphene sublattice symmetry into a triangular pattern, which can be seen in Figure C.8

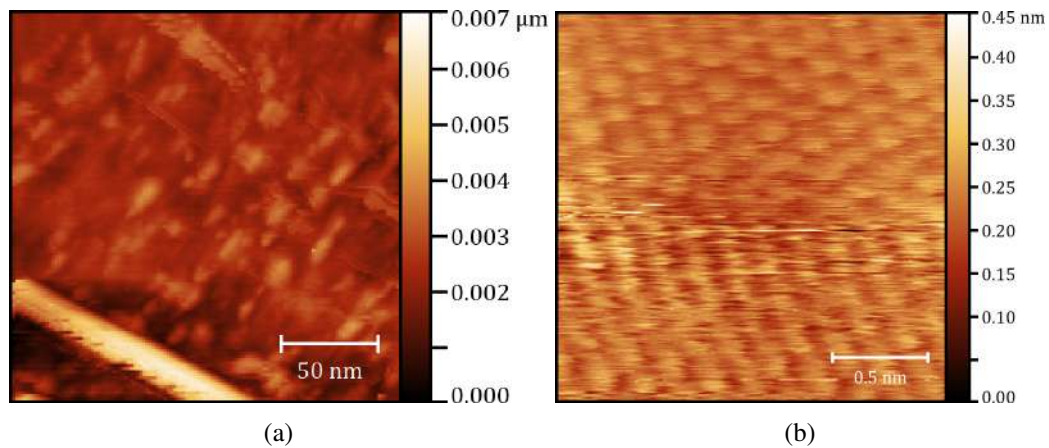


Figure C.8: (a): Example of a wrinkle formation during the deposition process. (b): Example of a triangular lattice formation in the monolayer graphene.

## C.5 Results

### C.5.1 Graphene Monolayer STM Data

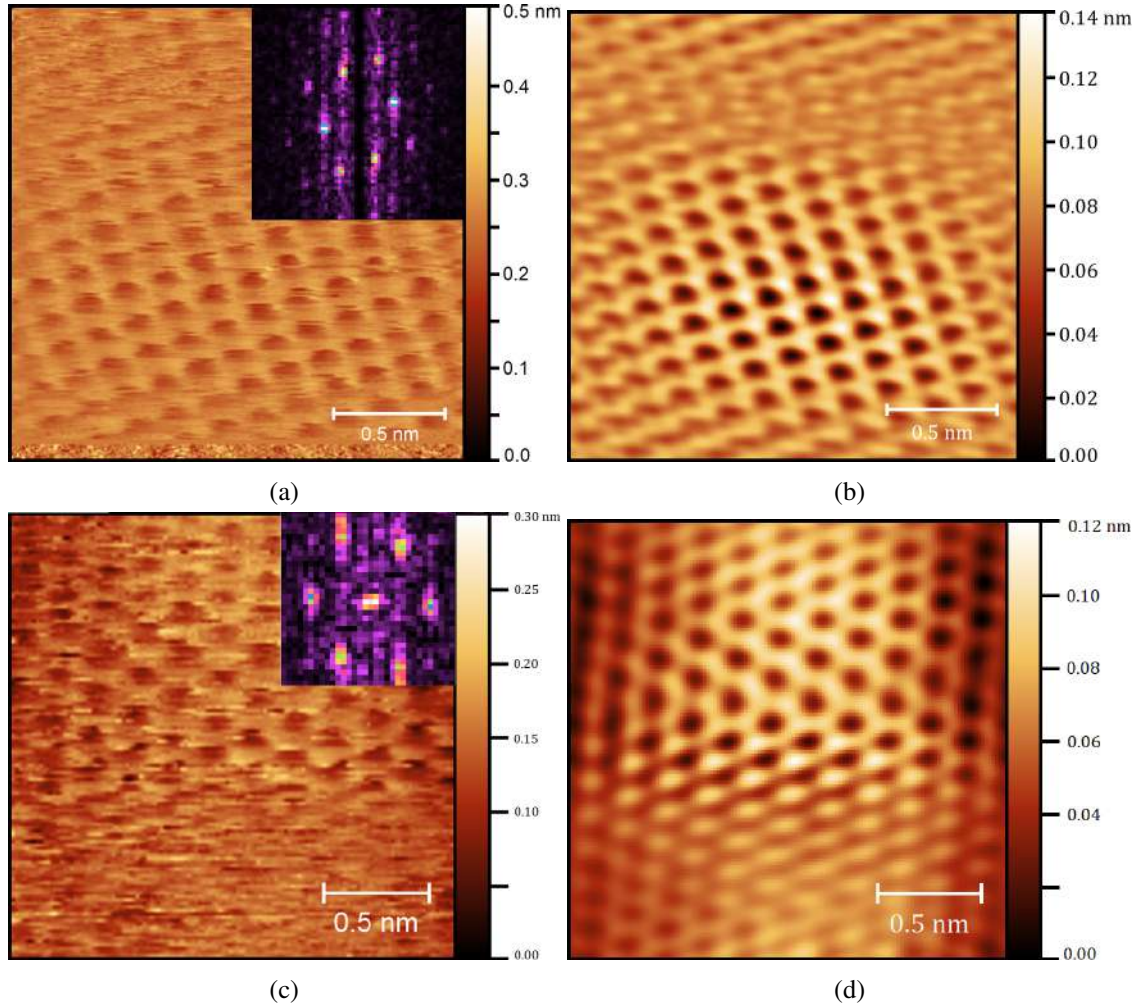


Figure C.9: (a), (c): Unfiltered STM measurement of the graphene monolayer sample. The inset shows the FFT, from there the hexagonal symmetry peaks were localized and filtered. (b), (d): Filtered STM image of the graphene monolayer. The lattice vectors  $\vec{a}_1$  and  $\vec{a}_2$  of the system were extracted from the upper image, where we can see a noticeable difference between them (see discussion on section C.6).

The first step regarding the STM experiment was to measure the standard monolayer graphene sample, which best results are shown in Figure C.9. The expected honeycomb lattice of the carbon atoms was resolved by the STM image (left). The 2D FFT (shown in the inset) was able to capture the very clear peaks associated to the hexagonal symmetry, which made possible good filtering of the noise, resulting in a more polished final image (right). The images were processed using the software **Gwyddion 2.61**.

In order to calculate the lattice vector, the distances between the dark gaps in the honeycomb structure

were measured and then an average over the values were taken. The result obtained were  $|\vec{a}_1| = 2.43(5)$  Å, within the reference value of  $a = 2.46$  Å, and  $|\vec{a}_2| = 1.82(7)$  Å, which is about 27% smaller. This anisotropy between the crystallographic directions, something not expected for the graphene system, can be explained by a few factors addressed in section C.6.

### C.5.2 Graphene Monolayer STS Data

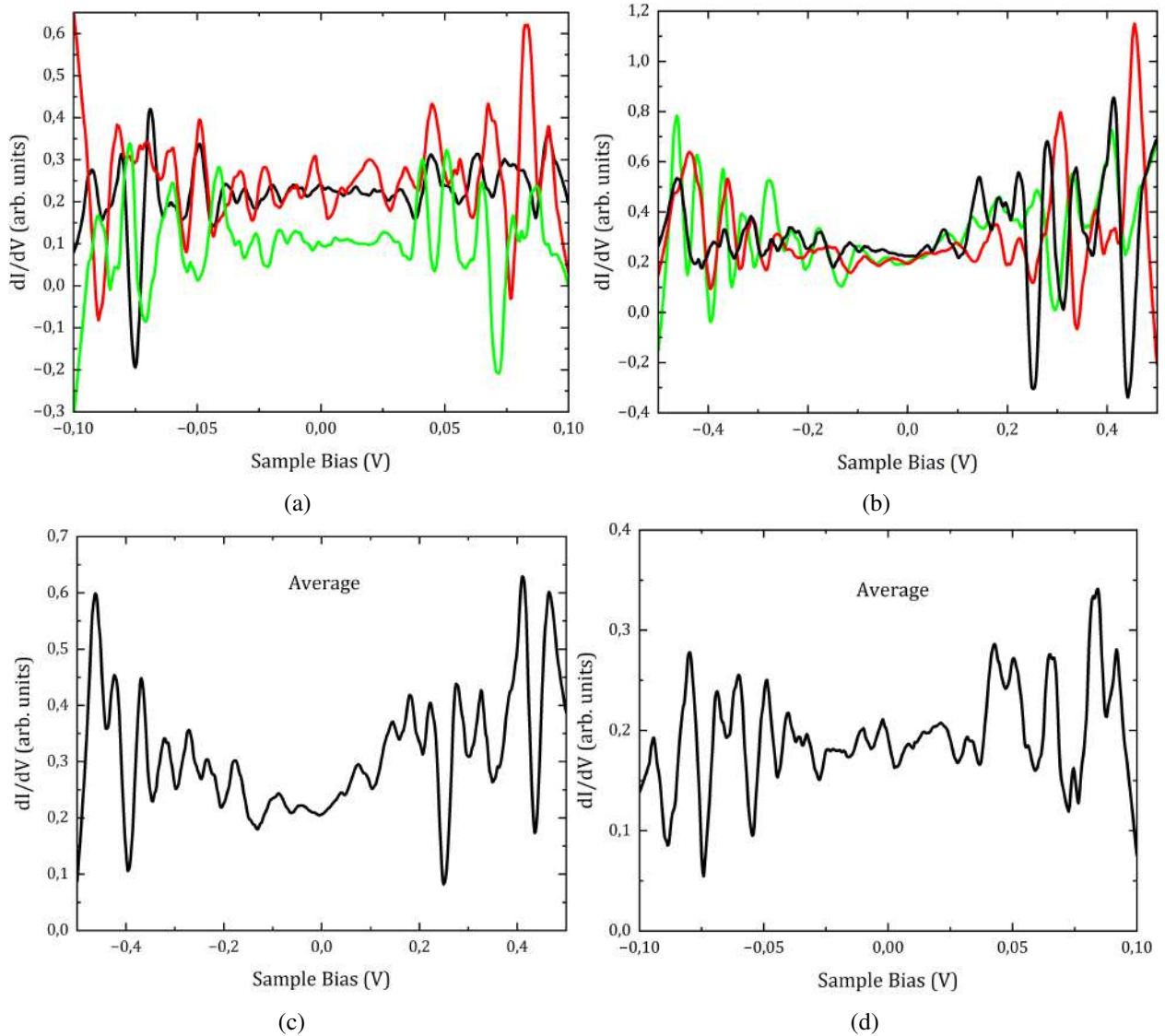


Figure C.10: Complete set of the acquired data on the tunneling conductance of the graphene monolayer sample for a sample bias sweep of: (a), (c): -0.1V to 0.1V; (b), (d): -0.5V to 0.5V. Each color curve is a different set of processed data from the STS measurement. The average of each set of measurements is also presented.

In order to obtain the  $\frac{dI}{dV}$  curves, the software **OriginPro 2022b - Learning Edition** was utilized. First, the  $I \times V$  curve was smoothed by using the method of Savitzky-Golay with 30 points window (chosen properly according to the number of data points). Then, the first derivative of the smoothed curve would be calculated and, finally, the derivative curve was smoothed by the same method, but with 20 points window now. The average of these curves were present in section 3.

The collected spectroscopy data for the monolayer sample is shown in Figure C.10. It displays the average tunneling conductance of a series of measurements for a bias voltage of  $-0.5V < V_{bias} < 0.5V$  and  $-0.1V < V_{bias} < 0.1V$ . Here, only the average was taken in order to reinforce statistical significance for the measurements and to compare with the bilayer sample data.

### C.5.3 Graphene Bilayer STM Data

After performing the measurements in the standard graphene monolayer, the next step was to start measuring the bilayer system. Since the objective here is to analyze the van Hove singularities in this system, it was interesting to be able to identify the Moiré superlattices. The best results are shown in Figure C.11.

The lattice parameters, once again, exhibited a discrepancy between the  $|\vec{a}_1| = 2.48(10) \text{ \AA}$ , and  $|\vec{a}_2| = 1.98(27) \text{ \AA}$ , about 20% less than the expected value. The Moiré superstructure has different calculated periodicity for each measurement. This feature is discussed in section C.6.

### C.5.4 Graphene Bilayer STS Data

Together with the STM measurements, STS data was also collected. Each spectroscopy measurement was repeated multiple times in order to give statistical relevance to the data. Three ranges of sample bias voltage were probed,  $-1V < V_{bias} < 1V$ ,  $-0.5V < V_{bias} < 0.5V$  and  $-0.3V < V_{bias} < 0.3V$ . The features associated to vHs should be symmetrical to the Fermi Level and persistent throughout different measurements in order to separate it from thermal excitation and background noise.

First, a broad measurement was performed, from  $-1V < V_{bias} < 1V$ , in order to identify possible vHs in the DOS of the system. A typical curve obtained is shown in Figure C.12. Each set of measurements represents a group of measurements done one next to the other, which means that they should be probing approximately the same surface area (because of the thermal drift). Each curve represents a different measurement and it is not possible to see a clear distinction between the vHs peaks and noise.

Then, in order to search for the hidden singularities, a more close bias voltage sweep, as shown in Figure C.13. Here, there is no clear indication of the vHs, as the noise can dominate the data. A final trial was attempted at an even shorter range, which is shown in Figure C.14. The noise once again surpasses any peak associated to a possible vHs in the system. Further discussion regarding the STS data is presented in section C.6.

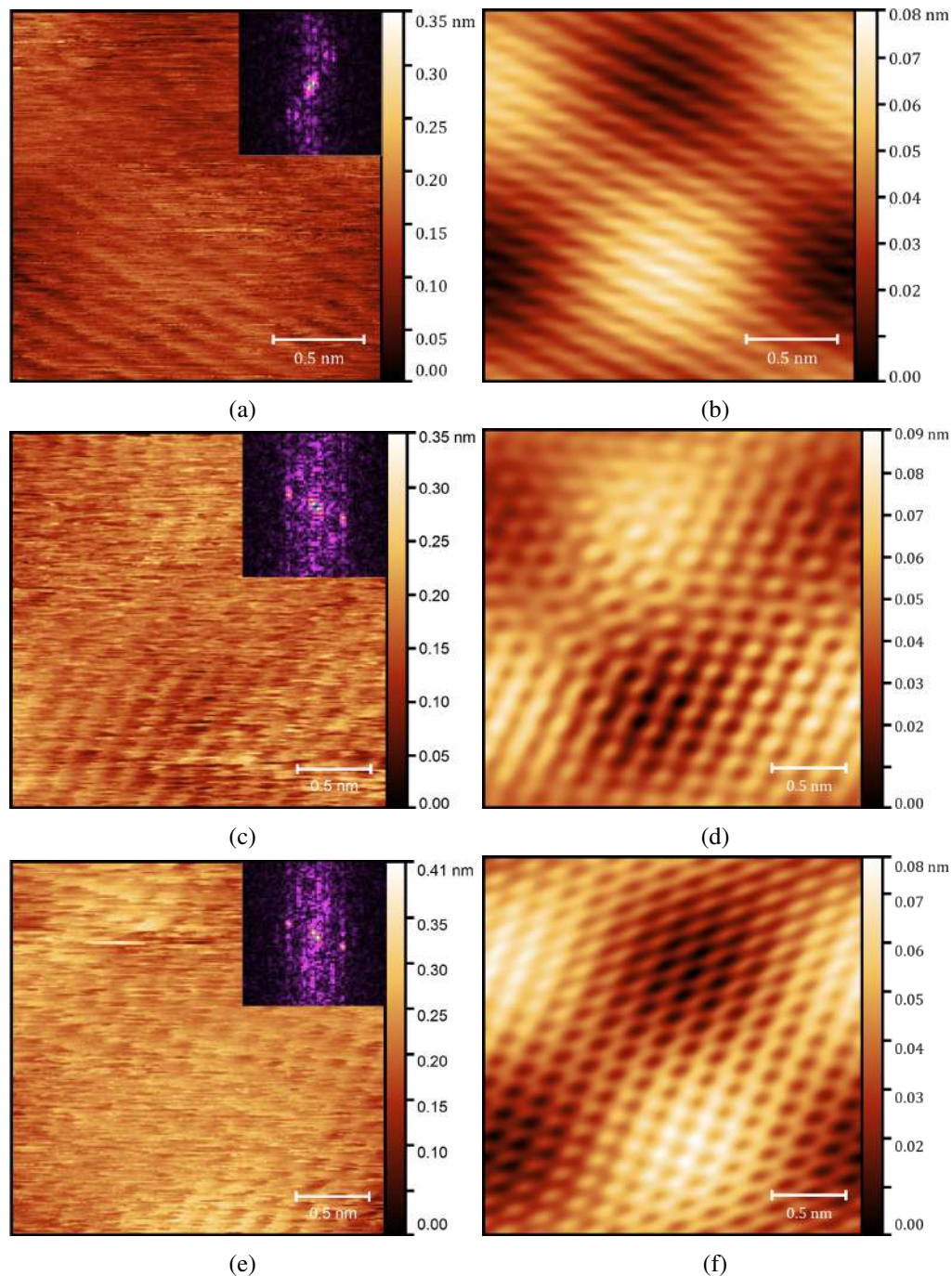


Figure C.11: (a), (c), (e): unfiltered STM measurement of the graphene bilayer sample. The inset shows the FFT. The hexagonal symmetry peaks associated to the graphene lattice are the external ones, while the Moiré superlattice peaks are concentrated in the center. (b), (d), (f): Filtered STM image of the system, where the Moiré superlattice becomes more evident.

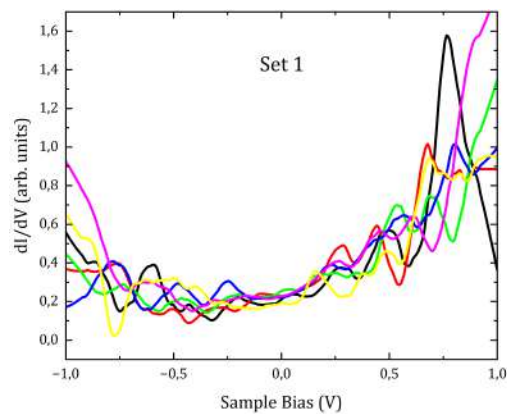


Figure C.12: Tunneling conductance of the bilayer graphene sample over the set of measurements for the sample bias of -1 V to 1 V. Each color represent a different measurement.

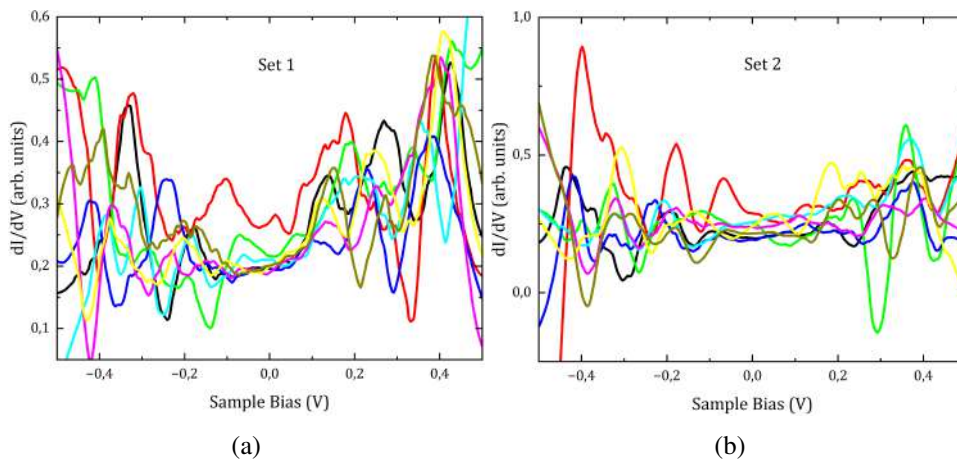


Figure C.13: Tunneling conductance of the bilayer graphene sample over the two sets of measurements for the sample bias of -0.5 V to 0.5 V. Each color represent a different measurement.

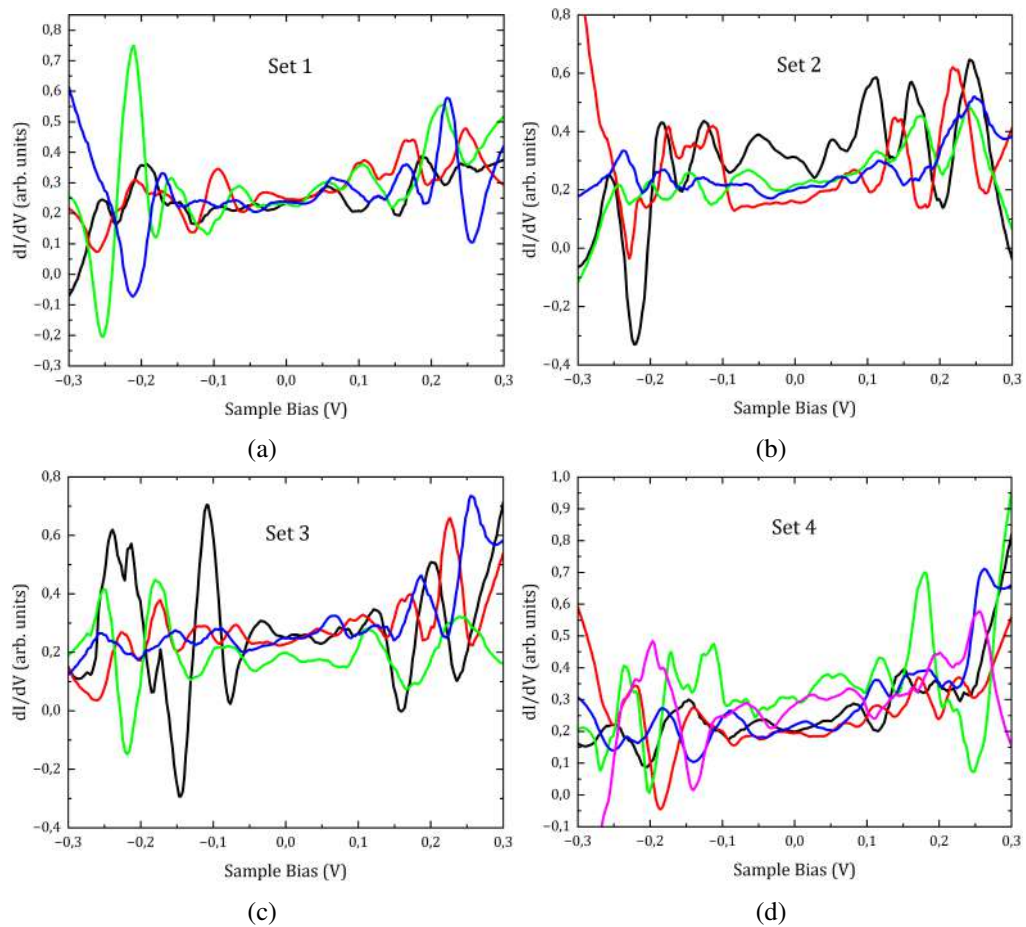


Figure C.14: Tunneling conductance of the bilayer graphene sample over the four sets of measurements for the sample bias of -0.3 V to 0.3 V. Each color represent a different measurement.

## C.6 Discussion

### C.6.1 Scanning Tunneling Microscopy Data

In general, it would take several attempts of imaging the sample in order to get a reasonably good result. Many of the different aspects of imaging graphene on SiO<sub>2</sub> and at ambient conditions have been addressed on previous sections, but there is one important observation to be made regarding the apparent giant lattice distortion observed in both bilayer and monolayer graphene STM measurements. These distortions can be understood within two important considerations. First, it is known that graphene on SiO<sub>2</sub> presents large-scale corrugations and the deposition process can also cause the formation of wrinkles, as shown previously in section 2. That makes the roughness of graphene on SiO<sub>2</sub> much larger than other substrates. Because of these characteristics, when the tip probes a tilted area, carbon hexagons may appear distorted in the graphene  $\pi$ -orbitals high directionality [73]. It is important to point out that these are fictitious distortions of tensile strain created by imaging experiment, which can exceed 10% of the origin lattice parameter.

Along aside with the substrate corrugation, it is necessary to take into consideration the thermal drift effect. Thermal drift is a time dependent movement of the tip relatively to the sample surface, which cannot be controlled during the measurement. This effect causes the images generated by the STM to be stretched along one or even multiple directions and are not well compensated by software treatment. Once the measurements present on this report were all taken at room temperature with no temperature control arrangements, thermal drift is expect to cause non-negligible distortion. Together with the previously mention effect, the distortion observed can be sufficiently explained.

Regarding the bilayer graphene system, as discussed in section 2, the SiO<sub>2</sub> substrate introduces a lot of complications to the imaging of the Moiré pattern. However, when sufficiently close, in order to avoid the previously mentioned corrugations, it was possible to capture an oscillation in the surface height which can be associated to the expected Moiré lattice. After measuring the periodicity of the new system by the same procedure adopted in the case of the lattice vectors, i.e, measuring the distance between the dark/bright features, we can use equation C.7 to find the twist angle of  $\theta_1 \approx 9.51^\circ$ ,  $\theta_2 \approx 6.11^\circ$  and  $\theta_3 \approx 7.40^\circ$ , respectively for the upper, middle and lower STM images of Figure C.11. This indicates the possibility of a range of different angles spread across the surface of the sample.

This can be understood when taking into consideration the synthesis process of the samples. The deposition on the graphene layer on top of each other is not homogeneous because the surface is polycrystalline, which means that portions of the graphene surface have different orientations throughout the sample. Consequently different twist angle when the second layer is deposited on top of the previous one. An example of a polycrystalline graphene surface is shown if Figure C.15.

### C.6.2 Scanning Tunneling Spectroscopy Data

Regarding the spectroscopy measurements, specially for the monolayer case, there are oscillations in the tunneling conductance, which make it not possible to distinguish the peaks associated to the van Hove





Figure C.15: Example of a polycrystalline graphene surface. Image from [74].

singularities. This profile can be explained by the factors mentioned throughout the report: large thermal excitation due to the room temperature, possible interference with air molecules, non-perfect tip craft and, most importantly, the  $\text{SiO}_2$  substrate, which creates scattering centers [72].

However, one can still use the STS data to reach for some interesting conclusions. As stated in section C.5.4, the vHs peaks must be symmetrical to the Fermi Level, consistent with different measurements (unlike the other noise factors). Thus, by taking the average over the measurements, it should be possible to make the vHs singularities more evident. Figure C.18 displays the average over the different measurements for the different sample bias range. Doing this, a clearer profile is generated, where the approximately symmetrical peaks are indicated.

By comparing the different sets of data, we note that the large scale voltage sweep (2 Volts) doesn't have any features in common with the other set of measurements. That's probably because a large number of data points would be required for this case in order to have a better resolution. On the other hand, for the 1 V and 0.6 V range scale, it is possible to assign some peaks which present both symmetry and consistency throughout different measurements.

For the 1 V range data, the two pairs of peaks around  $\pm 0.18\text{V}$  and  $\pm 0.39$  identified for each set are consistent between them, which may be an due to vHs. For the 0.6 V, we also see two pairs which are consistent among all the data (the peaks around  $\pm 0.174$  and  $\pm 0.110$ ). These peaks, found for the complete set of data, are consistent with twist angle of  $1.4^\circ < \theta < 6.4^\circ$  [75]. This also corroborates with the idea of multiple angles spread across different regions of the sample surface.

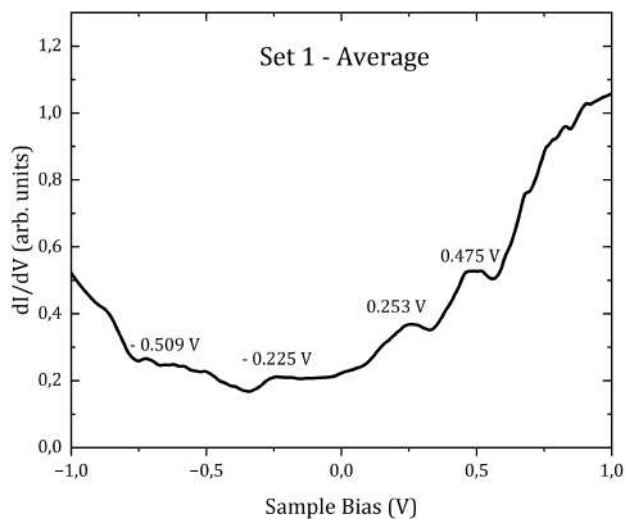


Figure C.16: Average of the STS measurements taken for the 2 V sample bias range. The arrows indicate the symmetrical peaks, with the distance (in Volts) between them.

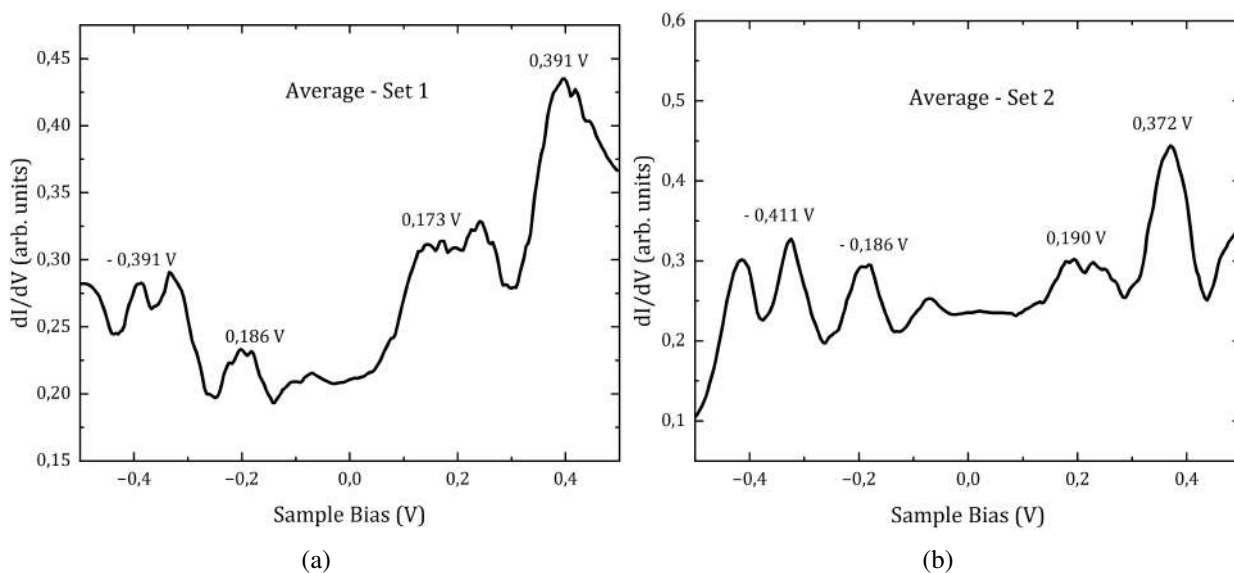


Figure C.17: Average of the STS measurements taken for the 1 V sample bias range. The arrows indicate the symmetrical peaks, with the distance (in Volts) between them.

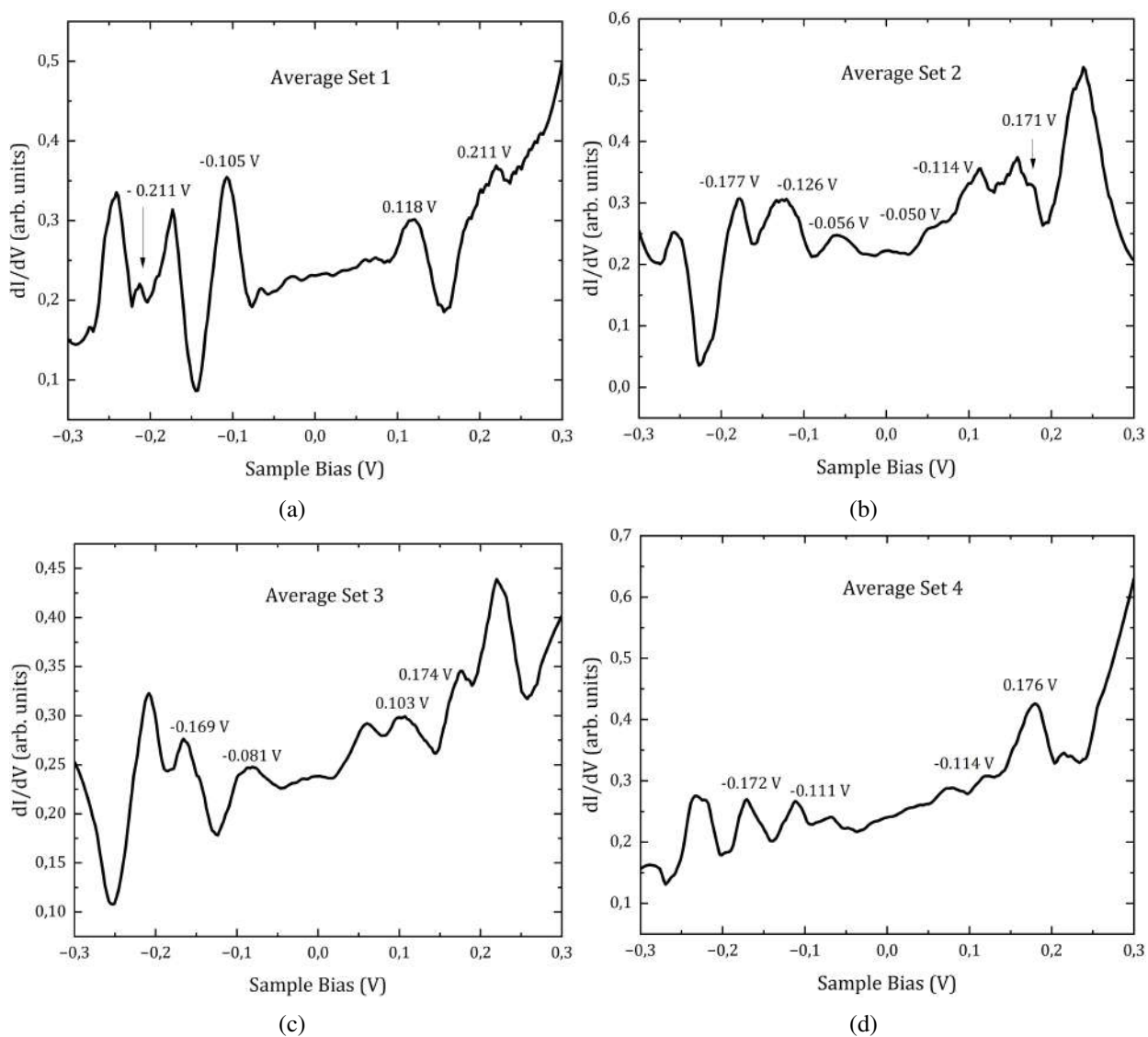


Figure C.18: Average of the STS measurements taken for the 0.6 V sample bias range. The arrows indicate the symmetrical peaks, with the distance (in Volts) between them.